TRACING THE DUSTY S-CLUSTER OBJECT ON ITS ORBIT AROUND THE SUPERMASSIVE BLACK HOLE IN OUR GALAXY
NEAR INFRARED OBSERVATIONS WITH SINFONI AT THE VERY LARGE TELESCOPE

INAUGURAL-DISSERTATION

zur
Erlangung des Doktorgrades
der Mathematisch-Naturwissenschaftlichen Fakultät
der Universität zu Köln

vorgelegt von

Florian Peißker

Köln 2018

Für meinen Sohn Jakob.

ABSTRACT

A faint gas cloud called G2 is found in 2011 on its way towards Sgr A* (that is associated with a supermassive black hole) in the center of the Milky Way. Since the first identification of this source (that is called Dusty S-cluster Object in the following), it is traced until spring 2014 in the red-shifted Brγ wavelength domain with the SINFONI instrument mounted at the VLT/Chile. It emits not only in the red-shifted Brγ domain (with respect to the rest wavelength at 2.1661 µm), the Dusty S-cluster Object (DSO) is also traceable in the red-shifted Paα and HeI regime. It is claimed, that the object in the years before the periapse (i.e., the closest approach to Sgr A*) already starts to dissolve due to the gravitational force of the black hole. Because of that, a tail is detected that follows the object towards Sgr A*. It is expected, that the 'head' and the 'tail' cause a firework-like event that leads to a bright accretion behavior of Sgr A*. In the observations that take place after May 2014, the emitted and prominent Brγ line is observed in the blue-shifted wavelength domain. This indicates that the source passed the supermassive black hole Sgr A*. Furthermore, the object is still intact after the periapse. In this work, a detailed and extensive analysis of the SINFONI data between 2006 and 2015 with a spatial pixel scale of 0".025 and a corresponding field of view of 0".8 × 0".8 per single data cube with the focus on the DSO is presented. In detail, the position of the DSO in the Brγ linemaps is compared to the position of the DSO in the Lucy-Richardson algorithm de- and re-convolved images. The K-band magnitude, as well as the flux from these images, are extracted. The derived orbit is based on the analyzed 10-year survey. Using the position and the velocity of the DSO from the data-cubes, position-velocity diagrams for every year between 2006 and 2015 are presented. Many authors believe that the object is rather a gas cloud than a dust embedded young stellar object. The question, why this topic raises such a controversial point of view, is discussed in this work. Also, the final answer about the nature of the DSO is given. For the analysis, the standard reduction procedure with the SINFONI and EsoRex pipeline is used. Because of not satisfying results, post-data corrections are applied in order to establish various calibration procedures. For the low-pass filtered images, the Lucy-Richardson deconvolution algorithm is applied to K-band images of the Galactic center region around Sgr A*. The analysis shows that the DSO can, without any confusion, be identified in the Brγ linemaps between 2006 and 2015. It can also be traced as a compact source in the deconvolved K-band images in every epoch from 2006 to 2015. A compa-

rison between stacked K-band and Lucy-Richardson images show the robustness of the procedure. The derived position-velocity diagrams underline the compact nature of the DSO. These extensive analysis methods reveal a new source that is called OS1. It follows the DSO on a similar orbit around Sgr A* and can explain the claimed tail emission of the DSO. The magnitude and flux extraction show that neither a brightening nor an increase in flux density of the infrared excess source takes place before or after the pericenter passage. The fact that the DSO can be observed in the near-infrared SINFONI data as a compact source between 2006 and 2015 indicates a stellar origin of the object. It is highly unlikely that a non-stellar object, for example, a gas cloud, could survive the pericenter passage of a supermassive black hole and stay compact on a Keplerian orbit especially after the fly-by event in 2014. A stretching that leads to the creation of a tail in the epochs before the periapse cannot be confirmed by judging the results in the linemaps, the low-pass filtered continuum images of the GC, or in the position-velocity diagrams.

Zusammenfassung

2011 ist die schwach leuchtende Gaswolke G2 auf ihrem Weg in Richtung des supermassiven Schwarzen Lochs, welches mit der Radioquelle Sgr A* assoziiert wird, im Zentrum unserer Milchstraße gefunden worden. Seit der ersten Identifikation dieser Quelle, die im Folgenden Dusty S-cluster Object (DSO) genannt wird, ist sie bis zum Frühling 2014 im rotverschobenen Brγ Wellenlängenbereich mit dem SINFONI Instrument, welches im VLT/Chile installiert ist, detektiert worden. Bezogen auf die Ruhewellenlänge bei 2.1661 μm strahlt das DSO nicht nur im rotverschobenen Brγ Wellenlängenbereich, sondern auch im rotverschobenen Paα und HeI Bereich. Es gibt Publikationen, die annehmen, dass sich das Objekt bereits in den Jahren vor der Periapsis, welcher den Punkt mit der geringsten Distanz zu Sgr A* definiert, aufgrund der gravitativen Kräfte des Schwarzen Lochs anfängt aufzulösen. Dementsprechend wird ein Schweif erwartet, der dem Objekt auf dem Weg Richtung Sgr A* folgt. Es wird vermutet, dass der „Kopf" sowie der „Schweif" Akkretionsvorgänge auslösen, die wiederum zu einer erhöhten Aktivität von Sgr A* führen. Allerdings zeigen Beobachtungen, welche nach Mai 2014 stattfanden, dass die emittierende und markante Brγ Linie in dem blauverschobenen Wellenlängenbreich zu finden ist. Dies zeigt, dass die Quelle an Sgr A* vorbeigeflogen ist. Es zeigt ebenfalls, dass das Objekt immer noch intakt ist. Entsprechend ist beim DSO nicht von einer Gaswolke auszugehen. Vieles deutet darauf hin, dass die untersuchte Quelle womöglich einen stellaren Kern besitzt.

In dieser Arbeit wird die detaillierte Analyse der SINFONI Daten zwischen 2006 und 2015 mit einer räumlichen Pixelskala von 0".025 und einem korrespondierenden Gesichtsfeld von 0".8 × 0".8 pro einzelnem Datenkubus mit dem Fokus auf das DSO präsentiert. Im Detail wird die Position des DSO aus den Brγ Linienkarten extrahiert. Anschließend wird die Linienkartenposition mit der Lage des DSO in den tiefpassgefilterten Bildern verglichen. Von diesen Bildern wird die K-Band Helligkeit, sowie der Fluss extrahiert. Der ermittelte Orbit basiert auf Observationen, die sich über einen Zeitraum von 10 Jahren erstrecken. Mit der Position und der Geschwindigkeit des DSO aus den Datenkuben können Positions-Geschwindigkeitsdiagramme für jedes Jahr zwischen 2006 und 2015 erstellt werden.

Für die Analyse wird die Standardreduktion der SINFONI und EsoRex pipeline benutzt.

Aufgrund fehlerbehafteter Resultate müssen die Daten nach der Reduktion erneut korrigiert werden. Für die tiefpassgefilterten Bilder wird der Lucy-Richardson Faltungsalgorithmus auf die K-Band Bilder des Galaktischen Zentrums der Region um Sgr A* angewendet. Die Analyse zeigt, dass das DSO, in den Brγ Linienkarten zwischen 2006 und 2015 identifiziert werden kann. Es kann ebenfalls als kompakte Quelle in den entfalteten K-Band Bildern in jeder Epoche zwischen 2006 und 2015 verfolgt werden. Ein Vergleich zwischen aufaddierten K-band und Lucy-Richardson Bildern zeigt die Zuverlässigkeit der Prozedur. Die ermittelten Positions-Geschwindigkeitsdiagramme unterstreichen die kompakte Natur des DSO. Diese intensive Analysemethode deckt eine neue Quelle namens OS1 auf. Sie folgt dem DSO auf einem ähnlichen Orbit um Sgr A* und kann die behauptete Schweifemission des DSO erklären. Die Gewinnung der Magnitude und des Flusses zeigt, dass weder ein Aufhellen noch ein Anstieg der Flussdichte der infraroten Quelle vor und nach dem Vorbeiflug am supermassiven Schwarzen Loch stattfindet. Die Tatsache, dass das DSO in den nahinfraroten SINFONI Daten als eine kompakte Quelle zwischen 2006 und 2015 observiert werden kann, deutet einen stellaren Charakter des Objekts an. Es ist höchst unwahrscheinlich, dass eine Gas- und Staubwolke ihre Struktur bei der Annäherung an ein supermassives Schwarzes Loch beibehält. Es ist ebenfalls anzuzweifeln, dass eine Wolke den Vorbeiflug an Sgr A* als kompakte Quelle auf einem keplerschen Orbit vollziehen kann. Dennoch sind viele Autoren davon überzeugt, das Objekt sei eher eine Gaswolke, als ein in Staub eingebettetes junges stellares Objekt. Die Frage, warum dieses Thema solch einen kontroversen Blickpunkt darstellt, soll ebenfalls in dieser Arbeit diskutiert werden. Auch wird eine mögliche Antwort bezüglich der Natur des DSO gegeben.

Eine Vergrößerung des Emissionsbereichs, welche zu der Schweifentstehung in den Epochen vor der Periapsis führt, kann basierend auf den Resultaten der Linienkarten, den tiefpassgefilterten Kontinuumbildern des galaktischen Zentrums oder den Positions-Geschwindigkeitsdiagrammen nicht bestätigt werden.

CONTENTS

Contents

CONTENTS

GENERAL INTRODUCTION

1.1

In the very center of our galaxy, the Milky way, a supermassive black hole (SMBH) of around 4 million solar masses can be found and observed. The first approach of pinpointing the location and deriving the mass of this SMBH in the near-infrared (NIR) is done by Eckart and Genzel (1996). For that, the proper motion of the surrounding stars (also called S-stars or the S-cluster) is determined. With these information, the authors are able to calculate the mass of Sgr A* of around $2.4 \times 10^6 M_\odot$. 20 years later, scientists still use this approach and derive similar masses ($4.02 \times 10^6 M_\odot$ by Boehle *et al.* 2016). Also, new techniques are used to calculate the mass by using only the observed flares (see Karssen *et al.* 2017) that are created by black holes. This is helpful for galactic cores that are too far away, providing the observer with information about the host galaxy and the supermassive black hole at its center.

Luckily, the closest known supermassive black hole is located in the star sign constellation of Sagittarius in our galaxy. Hence, it is named after its location with an additional asterix to underline its unique character as a radio source (Sagittarius A* or Sgr A*). It is less bright than other known galactic nuclei and much brighter than common radio sources that are found after its discovery. The chance of confusion regarding the nature of Sgr A* is very low and the assumption, that the investigated source is indeed a black hole, fits many theories and observations. Theories, that assumed other sources than a black hole, turned out to not hold observational data (see Phinney 1989). Therefore, the 2011 discovered object, that is moving towards the SMBH, is another indirect proof of the presence of

a SMBH in the center of our galaxy. Since astrophysicists rely on data, that is observed far away from earth, the discovery of the object (G2/DSO) promises an exciting insight of the behavior of the black hole. The nature of this object is reflected in its name: some authors believe, that the object is another gas cloud (like G1, see Witzel *et al.* 2017) that is able to trigger the flaring rate of Sgr A*. Others are convinced by a stellar explanation about the nature of this object and underlining this by naming it Dusty S-cluster Object (DSO).

The object, that is described in the following as the DSO, can be observed and traced mainly in the near-infrared (NIR) and emits in the red-shifted Bracket γ, Paschen α, and neutral Helium (Brγ, Paα, and HeI) domain with an increasing velocity before the periapse. After its pericenter passage in May 2014, it is traced in the blue-shifted domain of the related rest wavelengths with a decreasing velocity. With the velocity and the position, one is able to create a bounded orbit and give orbital elements that rule out the possibility of a non stellar origin. Since there is a lot of confusion about this object, it is important to clarify its nature in order to classify the observations for future theories about Sgr A*.

This work will trace the DSO on its orbit around the supermassive black hole at the center of our galaxy, proof the compactness (that is necessary for a stellar origin), give flux and magnitude information about the DSO, discuss the agreement with accepted flare statistics, and investigate the statistical robustness. Position velocity diagrams proof the compactness and show, that the object is not dissolving before or after the pericenter passage.

During the analysis of the SINFONI data, new undiscovered objects were found. They accomplish the analysis in such a way, that the observed features discussed by Gillessen *et al.* (2012) can be directed in a exciting new direction: that a supermassive black hole is an engine for the formation of dusty sources with a possible stellar component. Jalali *et al.* (2014) shows, that this a possible explanation for the observed sources in contrast to the assumption, that the high ionizing radiation in the vicinity of Sgr A* hinders the formation of young stellar objects.

Another discovered object is the X8 source. This object is discovered in the blue-shifted Brγ regime and shows strong sings of bipolarity. This could point to a young stellar object, that is a few million years old. That would be another indication, that a black hole is responsible for the formation of young stellar objects.

The ground-based data is observed with the Very Large Telescope (VLT) located in Chile on Cerro de Paranal. The author of this work traveled in total 8 times during the PhD to Chile to execute Galactic center (GC) observations with SINFONI. The data-sets are afterwards reduced and corrected for errors. Based on the obtained data cubes, image processing tools and enhancers are applied like low pass filtering with the Lucy Richardson deconvolution algorithm. Also, the approach of smooth subtracting the data reveals interesting details in the direct vicinity of Sgr A*.

The following chapters will explain and discuss the question about the nature of the DSO.

THEORETICAL BACKGROUND

This chapter shall provide the reader with useful information about the topic. It is highly recommended to consult additional sources (e.g., The center of our Milky Way, Eckart; Infrared Astronomy, A.T. Tokunaga; Galaxies and how to observe them, Steinike; Experimentalphysik 1, Demtröder;) for a broader understanding of the complex vicinity of the supermassive black hole in the center of our galaxy. Most of this chapter, if not stated otherwise, is based on the mentioned literature.

2.1 The galactic center

Since astronomers are able to observe the night sky, it seems that the Milky Way (the Galactic Center) is paid little attention. For example, the first Astronomer Royal of the English royal dynasty, John Flamsteed, neglected the illustration of the Milky Way (see Historia Coelestis Britannica) at all. The Cologne-based astronomer Eduard Heis, on the other hand, applied another approach by showing the first detailed map (only using his eyes) of the center of our galaxy (Atlas Coelestis Novus) in 1872. After the publication of the Atlas Coelestis Novus, the number of detailed publications of the center of the Milky Way increased. Edward Emerson Barnard (the famous Barnard 68 is named by him, see Fig. 2.8) for example observed many dark clouds in the Galactic Center and published them in his catalog from 1927 (see Barnard 1927). Of course, the bigger and better the telescopes become, the more details are accessible. The limiting factor is, unfortunately, the only optical detection system our body can offer.

Observing the galactic center

Since the galactic core is shielded by gas and dust, optical light is swallowed up by grains (see Figure 2.1). These grains will be discussed later on. But with the beginning of the 20th century till today, these small dirty clumps are triggering the development of CCD detectors that are able to observe the infrared part of the light. With this wavelength regime,
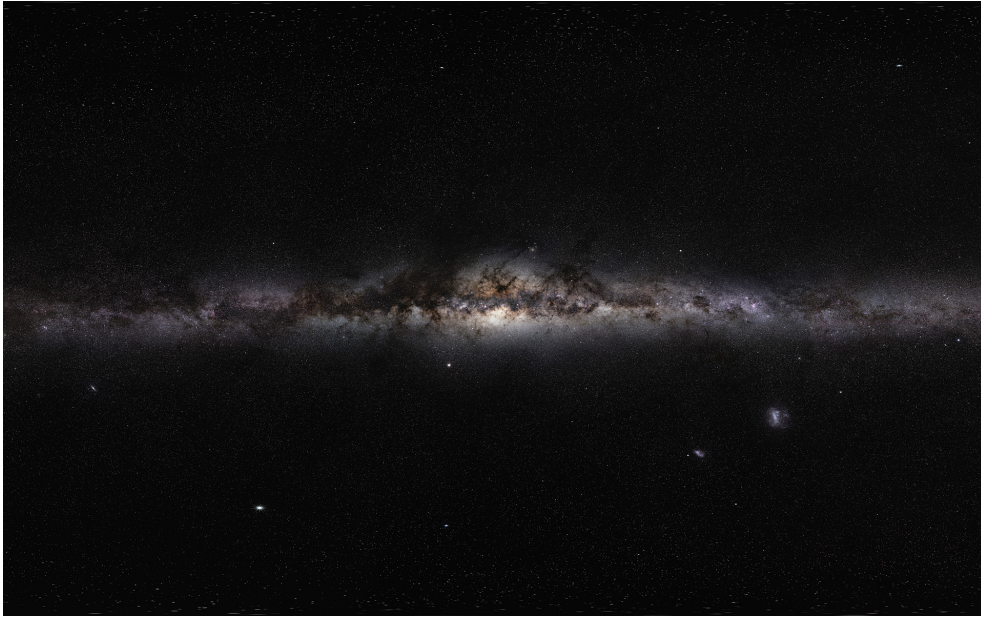

Figure 2.1: *The image, that is taken from* `www.eso.org`*, shows the Galactic center in the optical. To the lower right from the central bulk, the Magellanic clouds are located.*

one can see through the dust and observe the direct vicinity of Sagittarius A* (Sgr A*), the central supermassive black hole in our galaxy. As mentioned in the introduction, scientists argued for some time if other objects besides a SMBH could be a possibility like, for example, a cluster of neutron stars. To cite here Phinney (1989):

> "A young star cluster is a less contrived explanation than a massive black hole for many of the features seen in the Galactic center. However from a Copernican point of view, this explanation is less attractive than a black hole. The evidence for a $\sim 10^6 M_\odot$ black hole is becoming progressively less convincing, but the case *against* it is no stronger."

This citation already shows a controversial discussion about the nature of a nowadays well-known source. It seems that related topics are as controversial as the Galactic center itself: in 2011, an infrared excess source called G2 is found by Gillessen *et al.* (2012).

As mentioned in the introduction, the source will be called DSO for future references. Till 2014, this object moves with a increasing velocity towards Sgr A*. The closest approach is dated to 05.2014. After the periapse, the object is still moving on a Keplerian orbit on its predicted orbit around the black hole. However, the scientific community is divided when it comes to the nature of this object. The main arguments, which are in favor of a gaseous and dusty origin of this object, are the elongated shape of the source as well as the observed velocity gradient. Both arguments would be a clear indication of the proposed classification as a gas and dust cloud. In contrast to this point of view, the arguments that prefer a stellar origin are the detection of a compact source that is moving on a Keplerian orbit around the black hole. The detected size and the neglectable velocity gradient (see Eckart *et al.* 2013 and Valencia-S. *et al.* 2015) are not in agreement with the analysis of the object in Gillessen *et al.* (2012).

Nevertheless, the DSO source is a unique opportunity to study the behavior of the supermassive black hole in case of a close encounter of around 160 AU[1]. Additionally, the answer to the question, where this source is coming from, opens an exciting new view on black holes in general. As Jalali *et al.* (2014) shows, the presence of the supermassive black hole is necessary in order to support star formation. To observe the vicinity of Sgr A*, one needs powerful infrared instruments and a telescope with adaptic optics (AO) in a weather stable environment. For that, the Very Large Telescope (VLT) in Chile is a perfect match since the Atacama desert is one of the driest places in the world.

Dust or no dust

In this section, the different properties of dust and the influence on observations are discussed. It is assumed that not only the Galactic center is shielded by dust, but also the DSO. This implies, that the dust and gas are excited by a central source. This excitation and hence emission is then observed. The problem is the foreground dust between the observer and the galactic center. Because of scattering and absorption processes of the light from the Galactic center, one can describe extinction as follows:

$$extinction = absorption + scattering \qquad (2.1)$$

That means that the observed magnitudes have to be carefully corrected. If the simple ansatz of spherical dust grains with different sizes and masses is used, it becomes clear, that a distribution leads to a strong wavelength related dependency. Figure 2.2 shows such a relation. The authors of the plot try to explain the flat extinction between $3-8\,\mu$m by using different models. However, the main message of this work should be the observational data and the strong relationship between the extinction and the wavelength. It is, nonetheless, another example for many ongoing exciting investigations about our Galactic center with the help of the infrared wavelength regime.

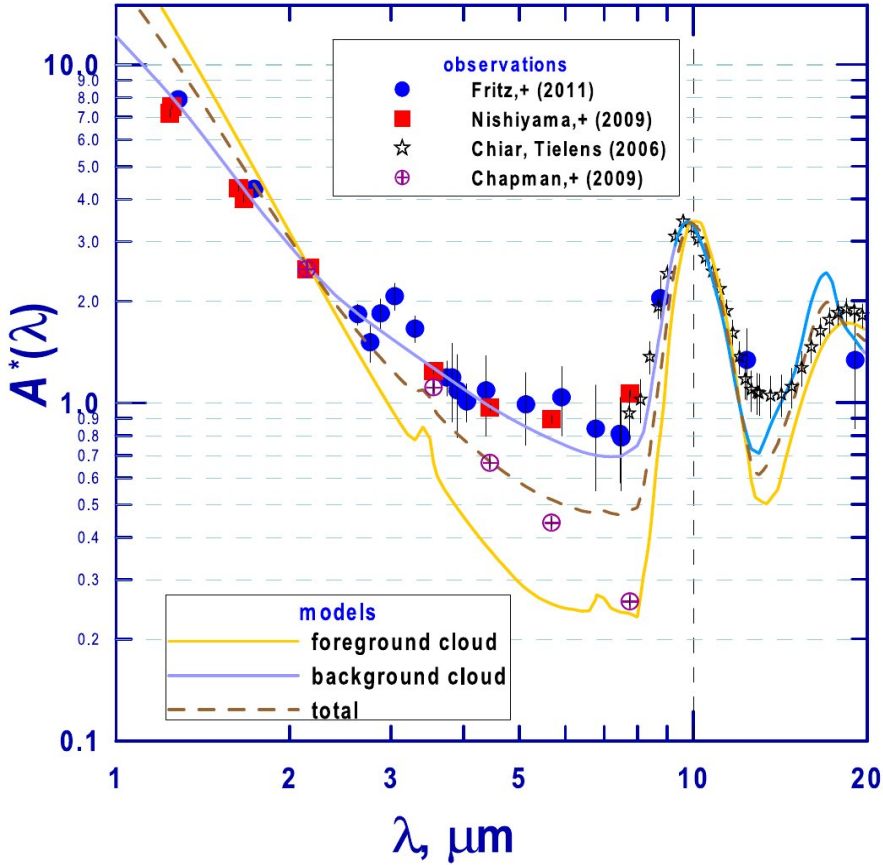[1] $1\mathrm{AU} \hat{=} 149 \times 10^6 \mathrm{km}$

Figure 2.2: *The y-axis represents the normalized extinction, the x-axis denotes the wavelength. The plot is taken from Voshchinnikov et al. (2017). It compares data for the Galactic center extinction from different publications and shows the robustness of the models and the observations. ©AAS. Reproduced with permission.*

Equation 2.1 shows, as mentioned, a rather simple ansatz. Figure 2.3 already implies, that even with a spherical model, the description of dust can get complex. The diameter d of the dust grains is in this example the major quantity that "decides" if a wavelength λ gets absorbed or scattered i.e. extinct. One can distinguish between three approaches:

$$\lambda \gg d \tag{2.2}$$

$$\lambda \ll d \tag{2.3}$$
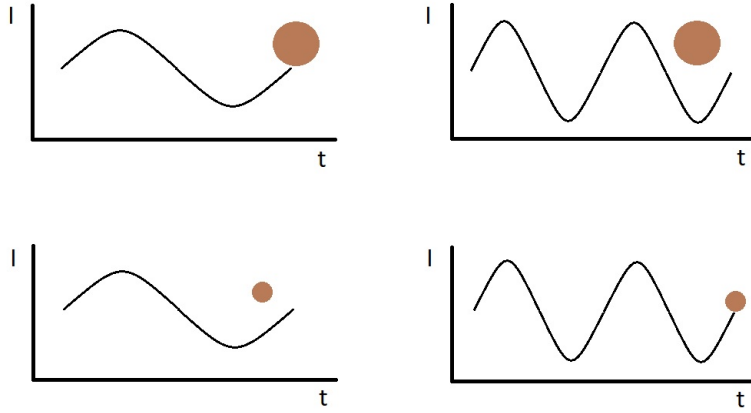
$$\lambda \approx d \tag{2.4}$$

Figure 2.3: *The y-axis shows the intensity I in arbitrary units. The x-axis represents the time. The interacting dust grain in two different diameters is here represented by the brown circles. The grain is penetrated by two different wavelengths.*

If the size of the dust partical is much bigger than the wavelength of the incident beam (Equation 2.2), Rayleigh scattering can explain these processes. For the cross section σ, i.e. the area of interaction between the beam and the dust grain, it is

$$\sigma(\omega) \approx \sigma_{Th} \frac{\omega^4}{{\omega_0}^4} \ , \tag{2.5}$$

where σ_{Th} is the Thomson cross section. Also, ω_0 represents the eigenfrequency of the scattering object whilst ω is the frequency of the incident scattered beam. In contrast to Rayleigh scattering, Thomson scattering is not valid for bound electrons, whole atoms or small energies. For that, the Klein-Nishina formula

$$\frac{d\sigma}{d\Omega}_{Klein-Nishina} = \frac{1}{2}\frac{\alpha^2}{m^2}\left(\frac{E'}{E}\right)^2\left[\frac{E'}{E} + \frac{E}{E'} - sin^2\theta\right] \tag{2.6}$$

is valid where α is the fine structure constant $\left(\approx \frac{1}{137}\right)$, E' the energy of the scattered photon, E the energy of the incident photon, and θ describes the scattering angle. $d\Omega$ marks the solid angle with $d\Omega = d\cos\theta d\phi$. Interestingly, expanding the Klein-Nishina equation for small energies leads to the simple form

$$\sigma(\nu) = \sigma_{Th}\left(1 - 2\alpha + \frac{56}{5}\alpha^2 + ...\right) \tag{2.7}$$

with the frequency ν, and $\alpha = \frac{h\nu}{m_e c^2}$ where m_e marks the electron mass.

However, smaller wavelengths and therefore higher frequencies are almost not interacting with the dust grains that are much bigger. For $\lambda \ll$ d, the incident beam passes the

dust. The path of the photons can approximately be described with geometrical optics, i.e. the beam follows a simple geometrical pattern (see Figure 2.4).
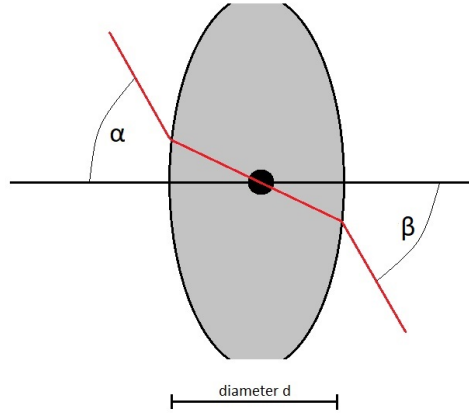

Figure 2.4: *This figure is a simple example for the accessibility of geometrical optics. The beam hits the lense and follows a traceable path that is influenced by the diameter of the optical system and the angle of incidence. The image is inspired by Demtröder (2004).*

If the wavelength is about the size of the dust, i.e. $\lambda \approx d$, the Mie theory describes the scattering process. It is an exact solution of the Maxwell equations that are introduced in 1908 by Mie (1908). For the sake of completeness, the Maxwell equations are defined as

$$rot\,E = -\frac{\partial B}{\partial t} \; , \tag{2.8}$$

$$rot\,H = j + \frac{\partial D}{\partial t} \; , \tag{2.9}$$

$$div\,D = \rho \; , \tag{2.10}$$

$$div\,B = 0 \; . \tag{2.11}$$

A detailed discussion of these equations can be found for example in Demtröder (2004). However, the scattering process can be separated into three pieces: the incident beam E_1, the one inside of the scattering object E_2, and the scattered beam E_3. In order to describe the scattering objects (=dust grains) between the observer and the galactic center, the so called T-matrix can be used. It represents the medium, that is passed by the beam E_2. It is only valid for scattering objects, that are far away from the observer. This boundary condition is fulfilled in the presented case. The mentioned T-Matrix is defined as

$$\begin{pmatrix} E_{\parallel S} \\ E_{\perp S} \end{pmatrix} = \frac{i\exp(-ikr)}{r} \begin{pmatrix} S_2 & 0 \\ 0 & S_1 \end{pmatrix} \begin{pmatrix} E_{\parallel e} \\ E_{\perp e} \end{pmatrix} \tag{2.12}$$

where E_S is the scatterd or observed beam. E_e marks the incident beam. Voshchinnikov *et al.* (2017) uses this approach in order to model and calculate the extinction efficiency factors for homogeneous dust grains.

The relation between the three discussed and present cases are displayed in Figure 2.5 where the cross section (y-axis) is a function of the wavelength. The smaller λ gets compared to a fixed size of the grain, the more the optical domain dominates. In larger wavelength domains, Rayleigh scattering describes the processes. If the wavelength is close to the dimensions of the dust, the above discussed Mie theory overshadows the other theories.
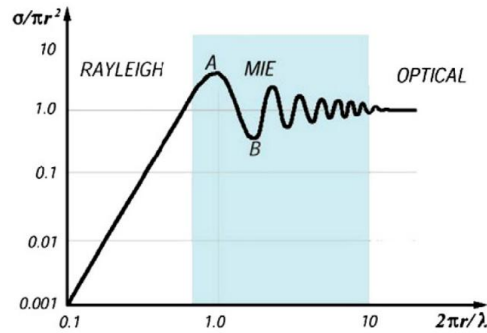

Figure 2.5: *This figure (see Liu et al. 2013) shows, that the Mie theory can explain more complex scattering situations.*

Hydrogen

Since the observations are mostly done in the wavelength regime between $1.45 - 2.45\mu m$ (H+K band), the Brγ plays an essential role in the later discussed analysis section. The object which is investigated in this work can be identified with a red- and blue-shifted Brγ line.

Luckily, hydrogen offers the most simple atom configuration with just a proton and an electron. Because of this structure, it is a basic building block of the universe and can be used to determine the redshift of galaxies by investigating the 21 cm line (the characteristic wavelength of Hydrogen). Our galaxy, for example, consists of 73% hydrogen, 25% helium, and 2% metals. Since helium with an atomic number of 2 (the atomic number of hydrogen is 1) is the lightest atom configuration, everything heavier is called metal. Simplified, it is created by the fusion of two hydrogen atoms. A famous example is a proton-proton cycle in the core of our sun. The fusion of two hydrogen atoms to one helium atom produces, according to Einstein (1905), energy. Because there is a negative difference in the Helium mass and the mass of two Hydrogen atoms after the nucleosynthesis, this mass is equal to

the mentioned produced energy with

$$E = mc^2 .$$ (2.13)

In 1913, Niels Bohr published the Constitution of Atoms and Molecules (see Bohr 1913 and Bohr and Rutherford 1913). With these publications, the Bohr model is introduced. It illustrates the absorbing and emitting behavior of electrons by assuming circular orbits of the electrons around the atomic core. As shown in Figure 2.6, the electron at the energy level n=2 gets excited by the incoming energy $\Delta E_i = h\nu$ where ν denotes the frequency and h the Planck constant. The particle is now excited and on the energy level n=3. Since there is nothing, that could hold the electron in n=3, it falls to n=2. By doing that, it emits radiation with $\Delta E_o = -h\nu$ where $|\Delta E_i = \Delta E_o|$. Additionally, ΔE_o can be less or more than ΔE_i. This is called Stokes or Anti-Stokes and is discussed in detail in Haken and Wolf (2003).
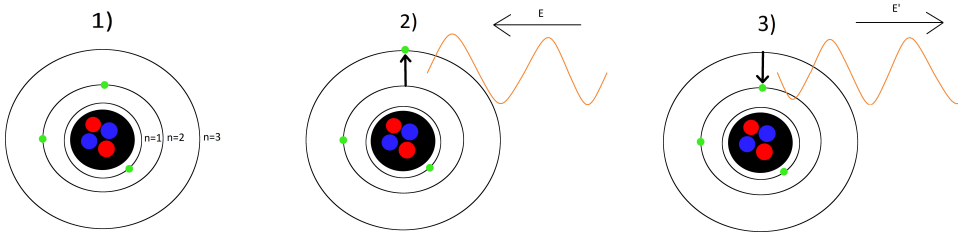

Figure 2.6: *This is the basic process of absorbing and emitting photons based on the Bohr model. Around the core (protons and neutrons in blue and red), electrons (green) are located on orbits. The excited electron moves to the next upper orbit. By falling back, the electron emits a photon.*

The excited Hydrogen atom emits several lines at different wavelengths called series. Interestingly, the Balmer-Series is already found in 1884 by its name giver. Rydberg and Balmer both tried to derive a theoretical model from their findings. Since the outcome is empirical (see Balmer 1897), no explanation is found for the constants and variables (like the energy level n). On the other hand, using the Bohr level enables a detailed analysis. One outcome is the exact description of the excited energy levels of Hydrogen with

$$E_n = -\frac{2\pi^2 m_e e^4}{h^2 n^2}$$ (2.14)

where n represents the energy level, h the Planck constant with 6.626×10^{-34} Js, m_e the electron mass, and e the charge of the electron. Since Bohr assumes circular orbits around the atom with quantized spacing, the angular momentum also has to be quantized since it scales with

$$\frac{1}{\sqrt{r}} \propto \frac{1}{L}$$ (2.15)

where L is the angular momentum. After applying this to

$$\Delta E \propto \frac{1}{r} \tag{2.16}$$

with ΔE as the quantized energy, one gets

$$L = n\hbar . \tag{2.17}$$

This already reveals a quantized description of the angular momentum as a function of n. Equation 2.14 becomes with this

$$E_n \approx -\frac{13.6Z^2}{n^2} eV . \tag{2.18}$$

The 13.6 eV is the value of the so called Rydberg constant that is defined as

$$R_E = \frac{(k_e e^2)^2 m_e}{2\hbar^2} = 13.6 eV . \tag{2.19}$$

Equation 2.18 formulates an interesting point of view on the empirical findings of Balmer and Rydberg. Since the atomic number for Hydrogen is Z = 1, one gets an easy accessible solution that explains the Balmer series with

$$E = E_1 - E_2 = R_E \left(\frac{1}{n_2^2} - \frac{1}{n_1^2} \right) . \tag{2.20}$$

Using the already mentioned photon energy definition E = $h\nu$ and $\nu = \frac{c}{\lambda}$ where λ denotes the wavelength, one gets finally the empirical found Rydberg equation

$$\frac{1}{\lambda} = R \left(\frac{1}{n_2^2} - \frac{1}{n_1^2} \right) \tag{2.21}$$

and

$$R = \frac{R_E}{hc} . \tag{2.22}$$

Finally, there is the theoretical and the empirical agreement that explains the found series. Next to the Balmer series (with $n_2^2 = 2$), the Lyman series ($n_2^2 = 1$) as well as the Paschen series ($n_2^2 = 3$) can be explained with this approach. Figure 2.7 shows the hydrogen term diagram that is based on the presented model. The energy levels n are represented by the horizontal lines. The upper thick one is the energy level at ∞. At −13.58 eV, the ground state with n = 1 is defined.
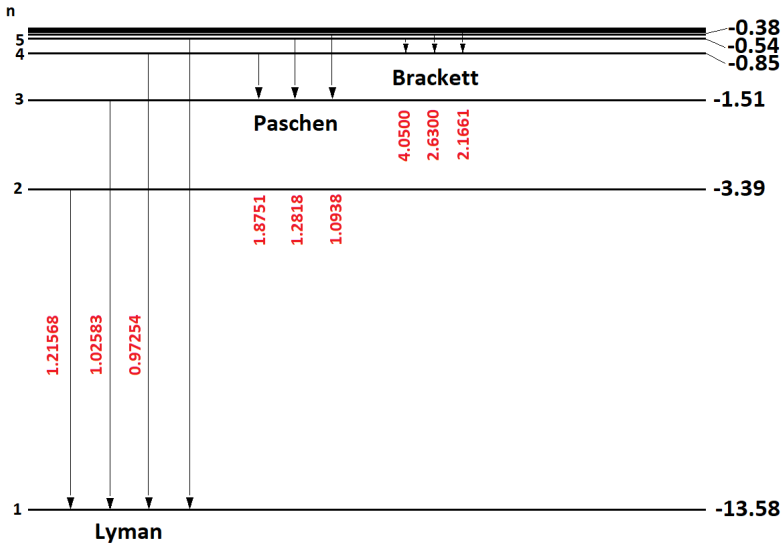
Figure 2.7: *The hydrogen term diagram (also called Grotrian diagram) shows the first Lyman, Paschen, and Brackett recombination lines. This image is inspired by* Grotrian *et al.* (1928).

Doppler effect

The detection of astrophysical objects is in many cases connected to sources that emit Doppler-shifted emission lines. Often, the investigated objects are moving with a velocity u_z. The emitted oscillation period $T = 1/\nu_0$ is moving in the same z-direction towards the observer. After a time T, it is

$$\lambda = \lambda_0 - u_z \cdot T = \frac{v_p - u_z}{\nu_0} \tag{2.23}$$

where $\Delta z = \lambda_0 = v_p \cdot T$. So the periods of a moving object differ just by Δz. The distance is defined as the wavelength λ. For the observed frequency it is

$$\nu = \frac{v_p}{\lambda} = \nu_0 \cdot \frac{v_p}{v_p - u_z} \quad . \tag{2.24}$$

This leads to

$$\nu = \nu_0 \frac{1}{1 - \frac{u_z}{v_p}} \tag{2.25}$$

where it is obvious, that the observed frequency ν is higher than the emitted frequency ν_0. If the object is moving in the $-z$ direction away from the observer, it follows directly

$$\nu = \nu_0 \frac{1}{1 + \frac{u_z}{v_p}} \tag{2.26}$$

since the velocity becomes $u_{-z} = -u_z$. Therefore, emitted frequencies become Doppler-shifted. In the case for the DSO, the emitted lines before 2014 are red-shifted since the object is moving away from the observer. After 2014, the emitted lines are blue-shifted since the DSO is moving towards the observer.

Dusty sources in the galactic center

In Galactic center observations, dust and gas are playing an important role. Ironically, dust not only blocks light like in the case of Barnard 68 (shown below), it can also help
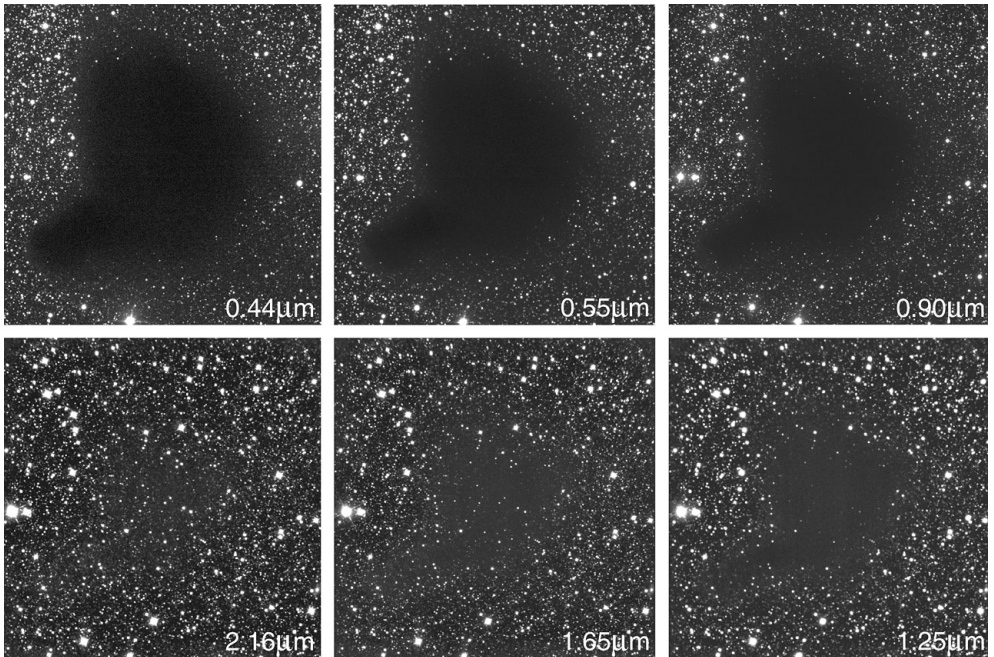

Figure 2.8: *The image shows the 500 light-years distant dusty cloud Barnard 68 at different wavelengths. The dust is optically thin for observing B68 in the* K_s-*band and becomes optically thick for wavelengths that are closer to the visible spectrum. The figure is taken from* `www.eso.org`*.*

identifying dusty objects in the Galactic center. Mostly because of scattering and excitation processes, that are discussed in the former sections, dust and gas are indirect tracers for young stellar objects (YSOs). Surprisingly, a lot of objects can be found in the wavelength regime between $1.45 - 2.45 \mu m$ with the same approach: searching for an excited and Doppler-shifted hydrogen line. This leads in most cases to a continuum detection that is representative of a dusty source. In the mentioned wavelength domain, one can find several excited hydrogen and helium lines that are presented in Table 2.1. Please note, that only relevant lines are listed. If a line is below a 3σ threshold, it is excluded to eliminate the chance of confusion. Depending on the weather conditions and the number of

Paα	Brδ	HeI	Brγ
1.87561 μm	1.94509 μm	2.05869 μm	2.16612 μm

Table 2.1: *This table shows the rest-wavelength for helium and different hydrogen series.*

observations that are directly translated to the on-source integration time, the detection of some lines is more challenging compared to other lines. As it turns out, the Brγ line is a reliable tracer when it comes to the identification of faint infrared objects that are close to the detection limit of the instrument. Nevertheless, the first dusty source in the Galactic center is the so called G1 object (see Ghez *et al.* 2005 and Clénet *et al.* 2005 for further information). This object is moving on a Keplerian orbit around Sgr A*. A bound trajectory around a central potential like a supermassive black hole favors a stellar origin of the object (see Witzel *et al.* (2017)).

However, another object is found in 2011 and is first published by Gillessen *et al.* (2012) where the authors claim, that the investigated object is a dust cloud without a stellar core. They report a stretching along the orbit and predict an increasing flare activity around the periapse, i.e., the closest approach of the cloud G2. It is named by Meyer and Meyer-Hofmeister (2012) in order to indicate that the object is as well as G1 a gas and dust cloud. As mentioned before, it turns out that G1 is not just a gaseous dusty object and the goal of this work is to do the same for G2. To underline the nature of the object, it is named Dusty S-cluster Object (DSO) by Eckart *et al.* (2013). Both models will be shortly discussed in the upcoming two sections. The presented cases are based on the publications of Gillessen *et al.* (2012) and Eckart *et al.* (2013).

2.2 One scenario, two approaches

G2, a gas cloud is approaching Sgr A*

In Gillessen *et al.* (2012) the authors present data-sets that are taken with the Very Large Telescope (VLT) that is located in the Atacama desert in Chile. The data consists out of NACO and SINFONI observations. Both instruments work in the near-infrared and will be discussed in chapter 3. Figure 2.9 shows a compilation of K_S (2.18μm) and L$'$ (3.80μm) data. The authors conclude that the absence in their K_S data and the parallel detection in
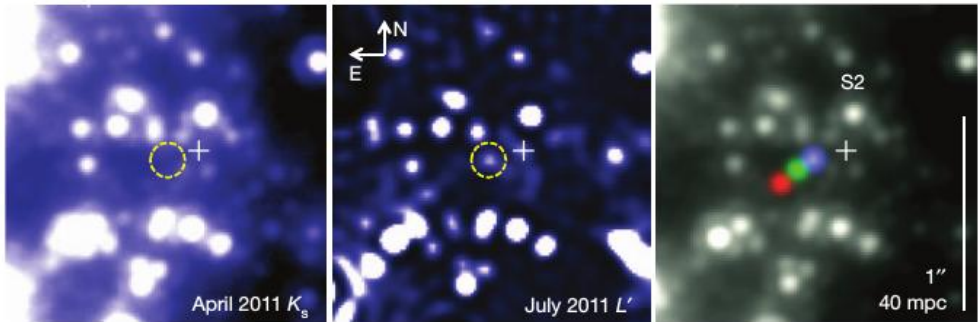

Figure 2.9: *The field of view shows the S-cluster with bright stars that move around the central black hole. The white cross marks the position of Sgr A*. Just above it, S2 is located. The image is taken from Gillessen et al. (2012). The data-sets are observed in 2011. The left image shows K_s, the middle one L$'$ data. The right image shows the position of G2 in several years (colored dots): 2004 (red), 2008 (green), and 2011 (blue).*

the L$'$ in combination with the tail detection (see Figure 2.10) points to a stretched gas/dust cloud. They derive increasing line of sight velocities of v $\approx 1200 \frac{km}{s}$ in 2008 and v $\approx 1600 \frac{km}{s}$ in 2011 from the red-shifted Brγ line. Additionally, they report a red-shifted HeI and Brδ line with the same redshift as the Brγ. Their position-velocity (pv) diagram shows partially smoothed data cubes (see the white dashed square in Figure 2.10) where the authors apply a 50 mas Gaussian to the data. Since the spatial pixel scale in SINFONI data cubes is 12.5 mas, the smoothing Gaussian, that is applied to parts of the presented data, is 4 pixels wide. That is approximately the size of full-width-half-maximum (FWHM) of the presented source itself.

The authors derive a temperature of around 550K from a blackbody fit. They use the two Ofpe/WN9 stars IRS16c and IRS16NW as calibrators and extinction values from Fritz *et al.* (2011). With this, they conclude a luminosity of L $\sim 5L_\odot$ where $L_\odot$ is the luminosity of our sun[2]. The derived mass from the temperature, luminosity, size, and the Case B recombination is around 3 earth masses[3]. The Case B recombination can be calculated

---

[2]$L_\odot = 3.9 \times 10^{23} \frac{ergs}{sec}$
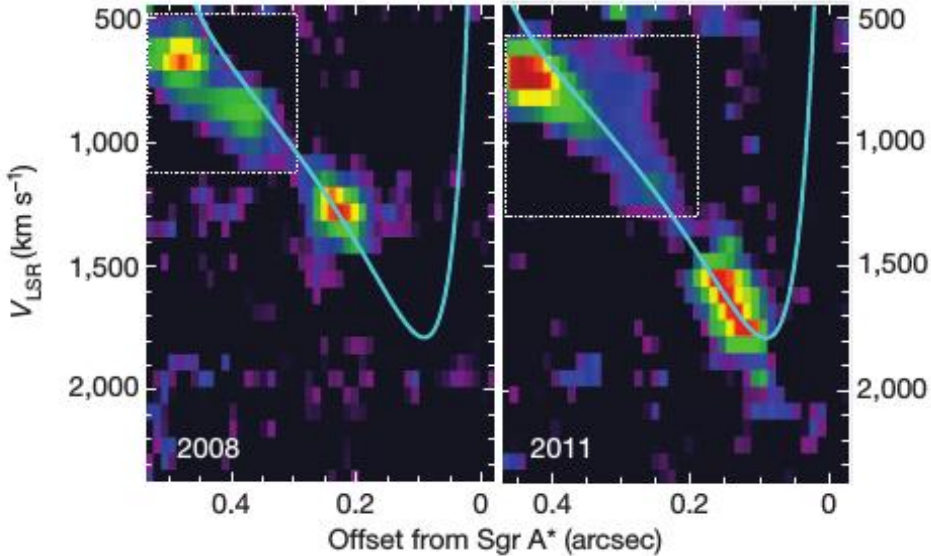
[3]$M_{earth} = 5.97^{24}$ kg

Figure 2.10: *These are two position-velocity diagrams taken from Gillessen et al. (2012). The left one is based on the 2008 SINFONI data; the right one is from 2011. The emission in the white square is smoothed and shows the claimed tail. The x-axis shows the distance to Sgr A*, the y-axis denotes the velocity in* km/s.

with the line ratios from, e.g., Brγ, HeI, and Brδ. For further information, the reader is advised to consult Peterson (1997), Burgess (1958), and Baker and Menzel (1938). Especially the latter publication spans over 18 publications with tables that connect the relative line intensities with particle densities. In Gillessen *et al.* (2012), the detected line flux ratio is $\frac{\text{HeI}}{\text{Br}\gamma} = 0.7$. From this, the cloud-mass is definite to ~ 3 Earth masses.

The distance between the cloud and Sgr A* at the closest approach is around 36 light hours. As a comparison, our Solar system has a radius of 1 light year (about 100000 AU[4]). It is believed, that the cloud gets disrupted after this approach since its unstable gaseous nature. With that, an increased flaring activity of Sgr A* is predicted since the gas of the cloud gets accreted. In early 2014 it is expected that G2 is dissolved and destroyed due to gravitational forces. Close to the pericentre, i.e., the closest approach of the cloud to the supermassive black hole, an increase in temperature up to $6 - 10 \times 10^6$K is predicted.

---

[4] 1 AU = 150×10^6 km

DSO, a dusty stellar object is approaching Sgr A*

In contrast to the presented model, Eckart *et al.* (2013) present the idea of a stellar nature of the object that they, as mentioned several times, named Dusty S-cluster Object (DSO). They present different deconvolved images where the authors apply either the Lucy-Richardson or Wiener algorithm. All results show the DSO at the expected L' position. From that, they extract a K_S magnitude and come up with a slightly different blackbody fit. With the additional H-band ($1.45\mu m - 1.85\mu m$) observations, they are able to give $H - K_S$ and $K_S - L'$ colors. With this information, they show a color-color diagram (see Fig. 2.11) with interesting dusty features. In principle, the authors claim that a mixture of dust and a stellar contribution of the NIR detection is possible.

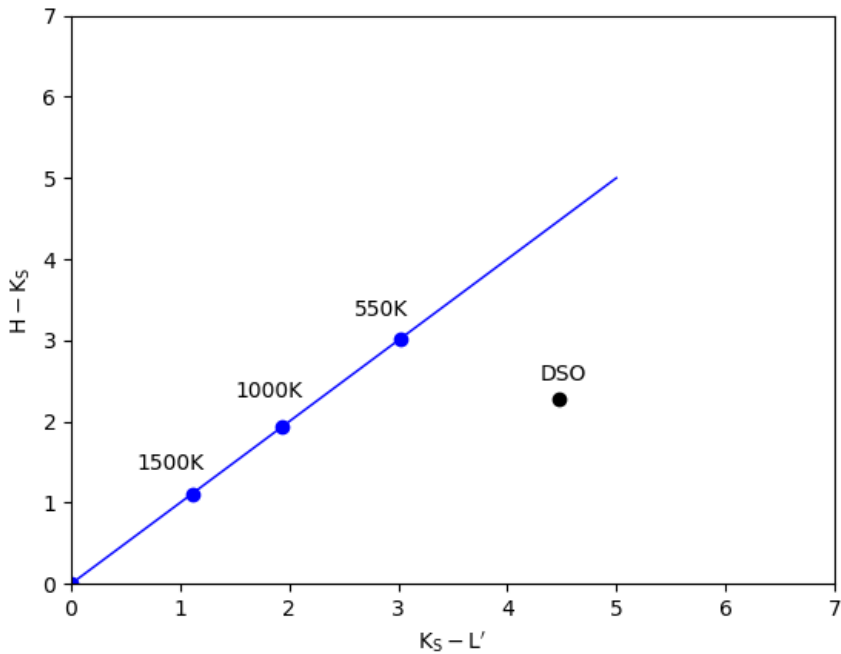**Figure 2.11:** *The figure is inspired by Eckart et al. (2013) and shows a color-color diagram. The y-axis denotes the $H - K_S$ color. The $K_S - L'$ color is plotted on the x-axis. The black numbers mark pure dust emission. An increased $K_S - L'$ color indicates a mixture of stellar and dust. The DSO (black circle) emission with a temperature of 550K could be explained with 80% dust and 20% stellar contribution.*

They also discuss the chance of a blend star. These "stars" are false signals that are caused by old stars that move so close to each other in the line of sight, that their light creates an apparent "new star". This is broadly discussed by Sabha *et al.* (2012) and the chance of confusing the DSO with a artificial created object is rather low (($\leq 10^{-4}$)). The reported Brγ luminosity in Eckart *et al.* (2013) is with $92 \times 10^{-3} L_\odot^{Br\gamma}$ 46 times higher than the Brγ luminosity observed by Gillessen *et al.* (2012). They exclude the idea of an external heating source since the surrounding stars must in this case also heat up other dust in the Galactic center. Since the mass of the object is low and the dust is heated by a central star that is hidden inside of the emission, Eckart *et al.* (2013) doubt that the pericentre approach leads to an increased flare activity of Sgr A*. The authors discuss different scenarios for the DSO that include a bow shock-like setup comparable to X3 and X7 (see Fig. 2.12) and a Wolf Rayet (WR) star.
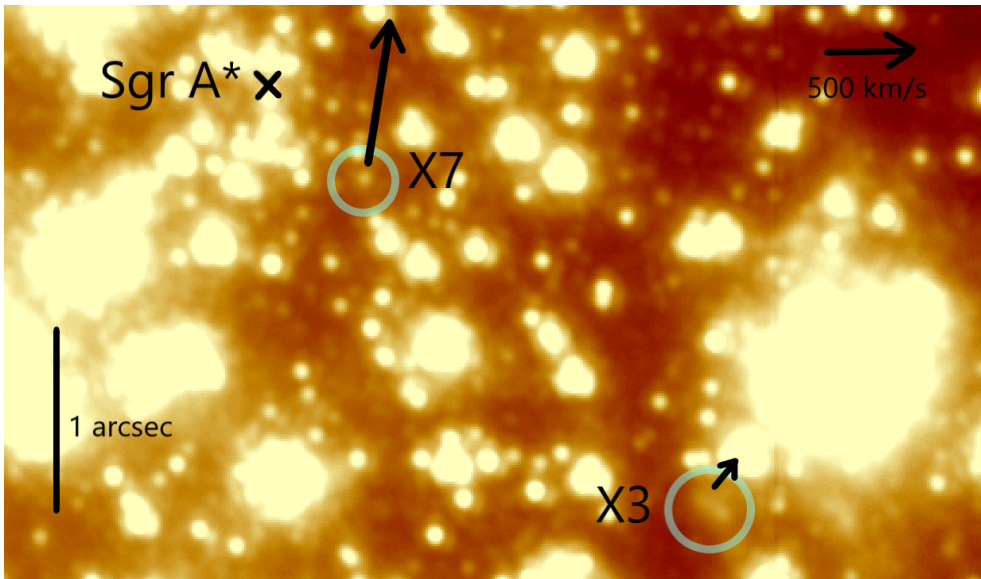
Figure 2.12: *An overview over the Galactic center region south-east of Sgr A* that is marked with a black cross. The bow-shock source X7 and X3 are marked with a dashed circle. The arrows indicate the proper motion of the two objects. X7 is moving with over* 600km/s*, X3 with around* 100km/s*. The data-sets are observed with NACO, an instrument mounted at the VLT. It operates in the infrared. The figure is inspired by Mužić* et al. *(2010).*

A proto-planetary disk is a scenario that Eckart *et al.* (2013) exclude since the origin would need to be a young stellar ring. To entangle a proto-planetary disk with this setup, it needs some sort of interaction that would have destroyed the disk in the first place. Another possibility is that a somehow formed disk was on another orbit and drifted after many orbital

periods to the high eccentric orbit the authors of both discussed publications observed. Again, the disk would be destroyed in this scenario due to the gravitational forces from the black hole as well as the radiation from the S-cluster stars.

OBSERVATIONS

Here, the used telescopes, the setup, the execution, and a general overview of the observations are given. The used instruments are as well explained as the influence of the weather conditions. Since the allocated time is limited, it is crucial to increase the usable-to-useless ratio. A well defined observation-plan is reflected in a higher Signal-to-Noise (S/N) ratio which is the key to the detection of the DSO.

3.1 The Very Large Telescope

The Very Large Telescope (VLT) started operating in 1999 with the Unit Telescope (UT) 1. It consists of 3 additional telescopes (i.e., 4 in total). The diameter of the main mirror on every telescope is 8.2 meter. It is one of the biggest optical telescopes in the world. The term "optical" could be misleading since the telescope operates also in the near-infrared. In this case, the term is loosely defined. Single dish, or in the case of the VLTI, multi-dish telescope would be a better fit. As shown in 3.1, the VLT also offers four smaller Auxiliary-Telescopes (ATs), each with a 1.8-meter main mirror. They are movable and can form an interferometer where they work together to increase the level of detail (the observations get 25 times finer). Recently, a new instrument called Gravity is installed to do the same with the bigger Unit-Telescopes (UTs). It offers, as well as many other instruments installed at the VLT, an K-band imaging mode. The astrometric accuracy can reach a resolution in the order of a few μas. With this instrument, it is planned to observe relativistic effects from Sgr A* on the orbit of the B0-2 V star S2 (see Paumard *et al.* 2006, Parsa *et al.* 2017, Gravity Collaboration *et al.* 2017, and Grould *et al.* 2017). The VLTI also operates like a optical telescope but with an artificial dish. Because the four telescopes work as one, it

Figure 3.1: *The four Unit-Telescopes, that are about to open, and the smaller Auxiliary-Telescopes. In the back between UT3 and UT4, the VLT Survey Telescope is visible.*

is a so-called baseline that replaces the diameter of a dish. The maximum distance between at least two telescopes defines the maximal possible resolution. The location of the VLT in the Atacama desert is a perfect fit since it provides stable weather conditions and a high number of observation nights throughout the year. The altitude of around 2635 m above the sea level is of course also helpful for the observations due to a thinner atmosphere. Even though the VLT is located close to the sea and the land line is directed in the north-south direction, the wind barely blows from west to east or vice versa. This is unusual but can be explained by the location itself. High mountains of the Chilean Andes shield "El Cerro Paranal[1]" to the east. The possible winds from the west are chilled since the high pressure and warm winds that are caused by the mentioned shielding are "pushing" against the stream. As a side effect, the Atacama desert is one of the driest places in the world with a humidity between 2% – 10%. Because of these conditions and the almost non-existent light pollution, it is an excellent site for telescopes working in the infrared. Additionally, a telescope that works only in the visible wavelength domain is also located on Cerro Paranal. It is the second telescope from the right in Figure 3.1 and is called VST, short for VLT Survey Telescope. With a dish-diameter of 2.6 m, it is the largest survey telescope that observes visible light.

---

[1] El Cerro Paranal = The mountain Paranal

Unit Telescope 1-4

The VLT consists of the four Unit Telescopes or UTs that are named in the language of the Mapuche, a group of indigenous inhabitants; UT1 (Antu), UT2 (Kueyen), UT3 (Melipal), and UT4 (Yepun). Mounted on these telescopes are a variety of different instruments that work in different wavelength domains for a vast catalog of observational situations and objects.

Since the UTs are located on a plane area on top of a mountain, it is not possible to point deeper than 20°. Therefore, one has to adjust the observations accordingly because the starting time could be scheduled to a too early time. Since wind speeds can reach high velocities[2], small openings in the telescope walls can be opened and closed for letting streams of air pass through. A useful side effect is the additional cooling function of the wind.

Next to the main mirror (M1), a secondary mirror (M2) is installed for the Cassegrain focus that is located above the M1 mirror.
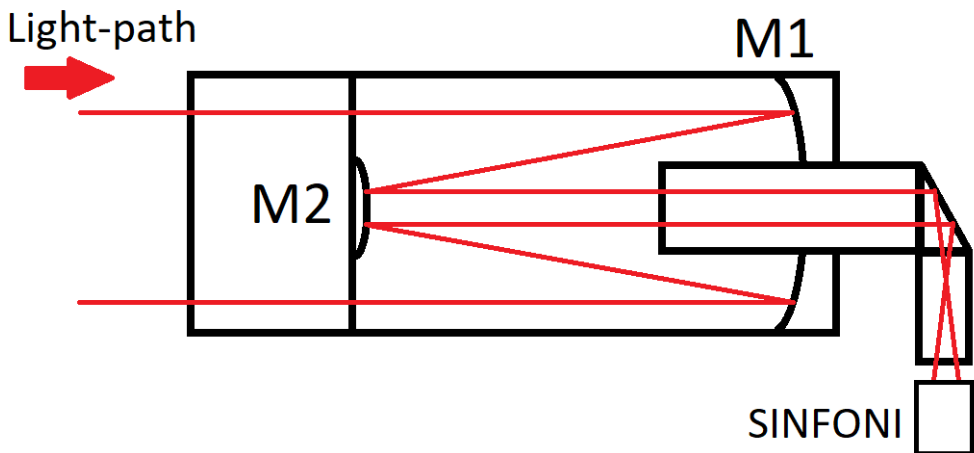
Figure 3.2: *The Cassegrain focus mode. This simple sketch illustrates the light path when it enters the telescope. First, the light hits the main mirror (M1) and gets reflected to the secondary mirror (M2). The collected light is then passed to another set of mirrors that is located at the base of the dish. From there, the light is directed to the SINFONI instrument that is placed in the Cassegrain focus. This image is inspired by Wilson (2013) and Riekher (1990).*

---

[2]The pointing restriction begins at $12\frac{m}{s}$. At $18\frac{m}{s}$, the telescope will be closed.

SINFONI spectroscopy

In 2014, 2015, and 2016 the Galactic center with the near-infrared integral field spectrograph SINFONI that is mounted on UT4 (see Eisenhauer 2003) is observed by the author of this work. The instrument consists of two components: a SPectrometer for Infrared Faint Field Imaging (SPIFFI) and an Adaptive Optics (AO) unit. The wavelength range reaches from 1.1 µm to 2.45 µm and therefore operates in the near-infrared. The instrument is installed in the Cassegrain (see Fig. 3.2) focus. Four different gratings are available with different spectral resolution and wavelength ranges: The selectable Field Of View (FOV)

	J	H	K	H+K
wavelength range	$1.10 - 1.40$ µm	$1.45 - 1.85$ µm	$1.95 - 2.45$ µm	$1.45 - 2.45$ µm
spectral resolution	2000	3000	4000	1500

Table 3.1: *The different wavelength operation modes of SINFONI.*

settings are $0".8 \times 0".8$, $3".2 \times 3".2$, and $8" \times 8"$. The most ambitious part of SINFONI/SPIFFI is most certainly the image slicer. With that, finer spectra, a reduced noise level as well as less image errors are possible. When the light from the telescope enters SPIFFI, it is directed to a pre-slicer that slices the image into 32 individual slitlets. They are reflected to a bigger slicer that re-arranges the 32 slits to one big long slit. In this sense, SINFONI works like a longslit spectrograph. The slit is then collimated by three mirrors and directed to the grating wheel that covers the 4 wavelength bands J, H, K, and H+K. The mounted detector is a Rockwell 2k × 2k pixel Hawaii 2RG array and a lens spectrometer camera. The scientific output file of SINFONI is a data-cube. This is a 3 dimensional cube that consist of two spatial (x and y direction) and one spectral (z direction) dimension. Figure 3.3 explains the basic principle of SINFONI.

CCD

The basic idea behind a digital detector can be explained with a charge-coupled device, known as CCD. The main advantages of this technology are the ability, to cool down the chip to reduce thermal heating, the size, and data accessibility. These arrays are silicon-based and consist of several layers. The charges of a single pixel are transmitted to a readout amplifier that is located outside of the array. Figure 3.4 shows a semiconductor with the gap between the valence and conduction band. To bring electrons in the conduction band, the energy E_G is needed. The incident photons carry the energy hf that induces electrons in the conduction band. These charges are then passed to the readout amplifier.
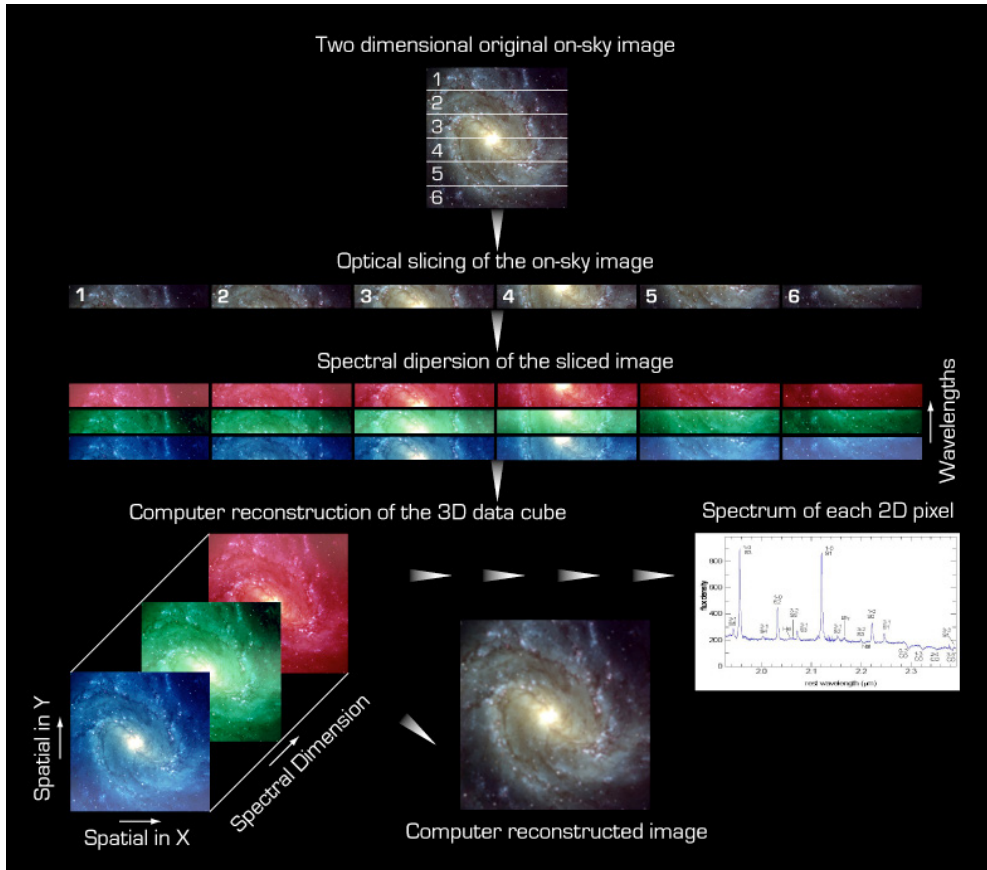
Figure 3.3: *In this example, the image is sliced into six single stripes. In reality, 32 slices are created mainly because of the variable sky-emission lines in the field of view. If just the 2d image would be created, a overlap of the lines disturb the result. After that, every single stripe is spectrally divided. Hence, every single stripe creates a "group" of sub-stripes. They are getting reconstructed by using the matching sub-stripes of each group. With that, an image is constructed for every wavelength (depending on the grating). In the end, the images are stacked above each other. They create the mentioned 3d cube where every single pixel shows the associated spectrum. The image is taken from www.eso.org .*
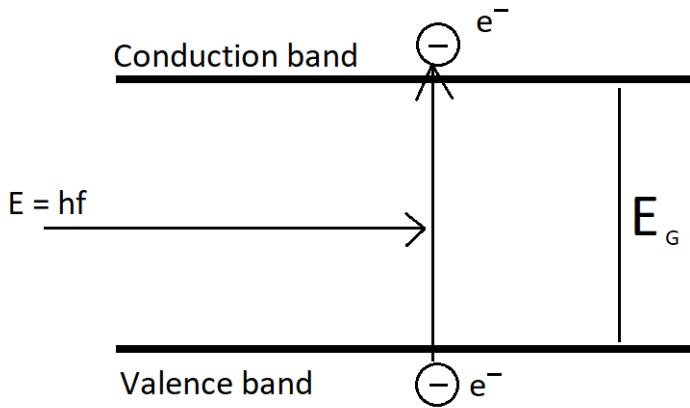
Figure 3.4: *The basic principle of a semiconductor with a band gap. Electrons are relocated from the valence band to the conduction band under the influence of the incoming light.*

Active and Adaptic optics

Historically, telescopes got bigger in time. Even though the techniques of building and constructing bigger mirrors improved, the image quality of the telescopes decreased. Since a 3-4 meter mirror weighs several tons, gravity becomes the primary mechanism that influences the image quality since the pull distorts the mirror shape. With the help of active optics, small actuators can push the mirror back into the non-distorted shape. This principle can be transferred to the adaptive optics (AO) system of the instrument. Between the secondary mirror M2 and SPIFFI, a Deformable Mirror (DM) is located. This mirror is controlled by the wavefront sensor: at the entrance to SPIFFI, an IR Dichroic (that works in principle like a beam splitter) reflects the optical part of the incoming light to the wavefront sensor. The infrared part passes the Dichroic towards SPIFFI. This has the advantage that all the IR light can be scientifically used while the optical part works as a calibrator for the DM. The biggest disadvantage is the optical regime. It is more negatively affected by weather conditions compared to the infrared regime.

The wavefront sensor receives the light from the pre-selected Natural Guide Star (NGS), that is disturbed by turbulence in the atmosphere. These turbulences are causing a deformed wavefront that is reflected in the point spread function (PSF). Every ground-based observation is influenced by the atmosphere which creates a PSF. Since the astronomical objects are approximately point sources, the received image is a mix of a point source and the point spread function, i.e., the atmosphere. Of course, the weather conditions play an important role. But even with almost perfect weather conditions, the movement of the atmospheric layers would cause a PSF. That translates into the so-called Airy disk where the

central circular intensity peak is the PSF. The wings of the wave create small rings around the central disk that are shown in Figure 3.5. It is the result of the diffraction limit. When
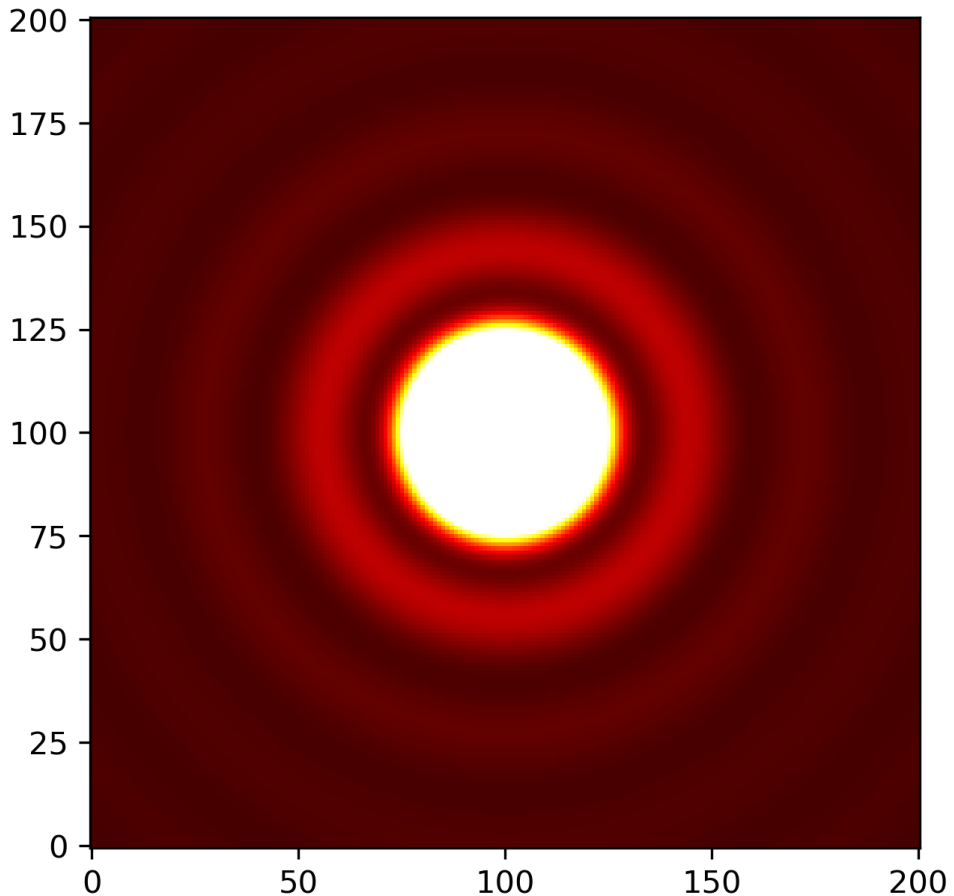

Figure 3.5: *In the center of the Airy disk, the maximum intensity of the incident beam is located. The rings around that center have decreasing intensities, i.e., every successive ring has a lower intensity compared to the former one.*

the light of an object passes through an observing setup, it creates concentric rings around a central bright spot. These rings have a decreasing intensity compared to the central spot and can be described with the so called first kind Bessel function

$$J_\alpha(x) = \sum_{m=0}^{\infty} \frac{(-1)^m}{m!\Gamma(m+\alpha+1)} \left(\frac{x}{2}\right)^{2m+\alpha} \tag{3.1}$$

that is also visualized in Figure 3.6. The maximum of the function is at r = 0.0 whereas the following local maxima can be found at some distance r > 0. The first minimum can be
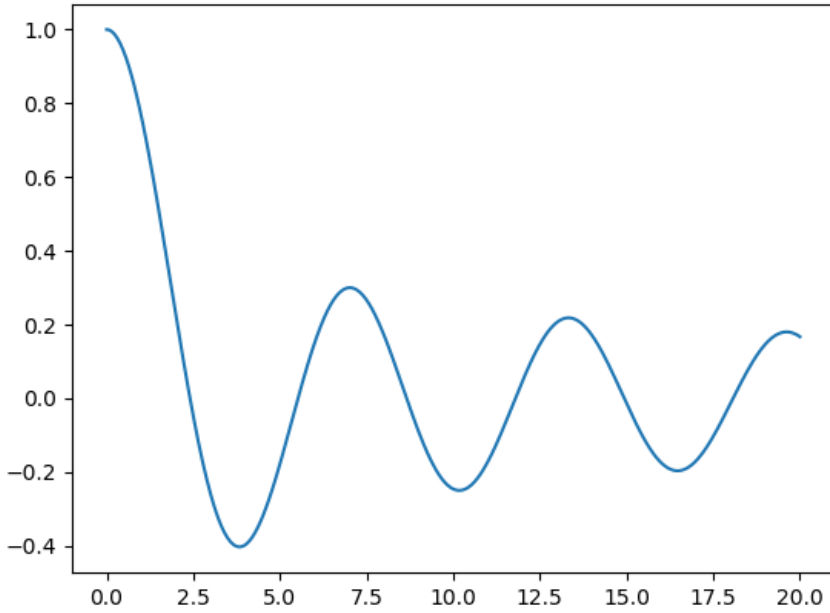
Figure 3.6: *The bessel function reflects the basic behavior of the former introduced airy disk. The global maximum is located at* x = 0.0, *the following local maxima have a decreasing intensity.*

found at

$$sin(\theta) \approx 1.22 \frac{\lambda}{d} \tag{3.2}$$

where d denotes the diameter of the aperture (i.e. telescope dish diameter) and λ the incoming wavelength. The radius r of the Airy disk marks the resolution of the telescope. The resolution describes, if an observer is able to distinguish between two maxima of two distinct objects. The intensity of the Airy disk can be calculated with

$$I(\theta) = I_0 \left(\frac{2J_1(ka\,sin\theta)}{ka\,sin\theta} \right)^2 = I_0 \left(\frac{2J_1(x)}{x} \right)^2 \tag{3.3}$$

where J_1 is the introduced first kind Bessel function. Also, k denotes the wavenumber (= $2\pi/\lambda$), a the radius of the aperture (i.e. telescope dish), and θ the observational angle. θ is defined as the angle between the dish axis and the connection line between the observational object and the center of the dish. Equation 3.3 and Figure 3.6 are the result of the Fourier transformation of an incoming beam.

However, the AO module compares the intensity of the received PSF with the intensity of a perfect PSF. The result of the comparison is called Strehl ratio. The Real-Time-Computer (RTC) is now adjusting the deformable mirror by controlling 60 bimorph electrodes. The then corrected light is again split up by the Dichroic and passes the RTC where the Strehl ratio is calculated. Afterward, the DM again is trying to correct for the distortions. This loop is, of course, strongly depending on the frequency of the wavefront sensor. If the change of the turbulences are too fast, the correction loop will not be able to follow the behavior. In this case, it would make sense to reduce the frequency of the loop to get a better result. Even though this observing strategy can solve the problem, too fast changing atmospheric layers are not promising observation conditions. As an astrophysicist, choosing the weather conditions is not possible. Therefore, one has to come up with a detailed observational plan that will be explained in the following section.

3.2 Observations

For the observations, the H+K (1.45 µm - 2.45 µm) grating is chosen because of the increased amount of information compared to the K-band grating (1.95 µm - 2.45 µm). Also, the limiting magnitude for the continuum is higher with the selected H+K band and FOV[3]. The integration time of the individual exposures is set to 400s mainly to avoid fast changing weather conditions that result in a decreased overall quality of the data. Even though 600s is possible, the chance of the discussed situation where the conditions could decrease in such a way that the RTC works to slow can be reduced. The observations in the Galactic center in the past years (2006-2015) show that an exposure time setting of 400s is also a good compromise between usable data and assigned observation time. Lowering the exposure time also leads to a decreased influence of negative external sources. The analysis is done in the sub-pixel domain. Avoiding external and internal noise sources is crucial since the DSO signal is close to the detection limit. It is important to note that an increase of the total on-source exposure time does not correlate with the signal quality of the red and blue-shifted infrared excess emission source since individual data cubes have to fulfill certain criteria that will be explained in the following. If the total number of observation nights are limited, the mentioned exposure time setting is a considerable strategy to get a high quality per single exposure ratio.

The 0".8 × 0".8 field of view (FOV) of the single exposures are jittered around Sgr A* to cover a larger FOV ($\approx 1'' \times 1''$). As explained in Valencia-S. *et al.* (2015), the observations avoid regions that could lead to a nonlinear behavior of the detector. This can be achieved by placing the star S2 in the upper right quadrant of the SINFONI fast reduction screen as shown in Figure 3.7. The spatial pixel scale of SINFONI is set to the lowest value, i.e., 0".025. This setting corresponds to a 0".8 × 0".8 FOV for a single data cube. Since the observations are the most important part of the observing run, the observations have to be prepared sometime before the observing nights. For that, p2pp is used to create an Ob-

---

[3]$\mathrm{mag}_{\mathrm{H+K\,limit}} = 19.2$ compared to $\mathrm{mag}_{\mathrm{K\,limit}} = 18.3$
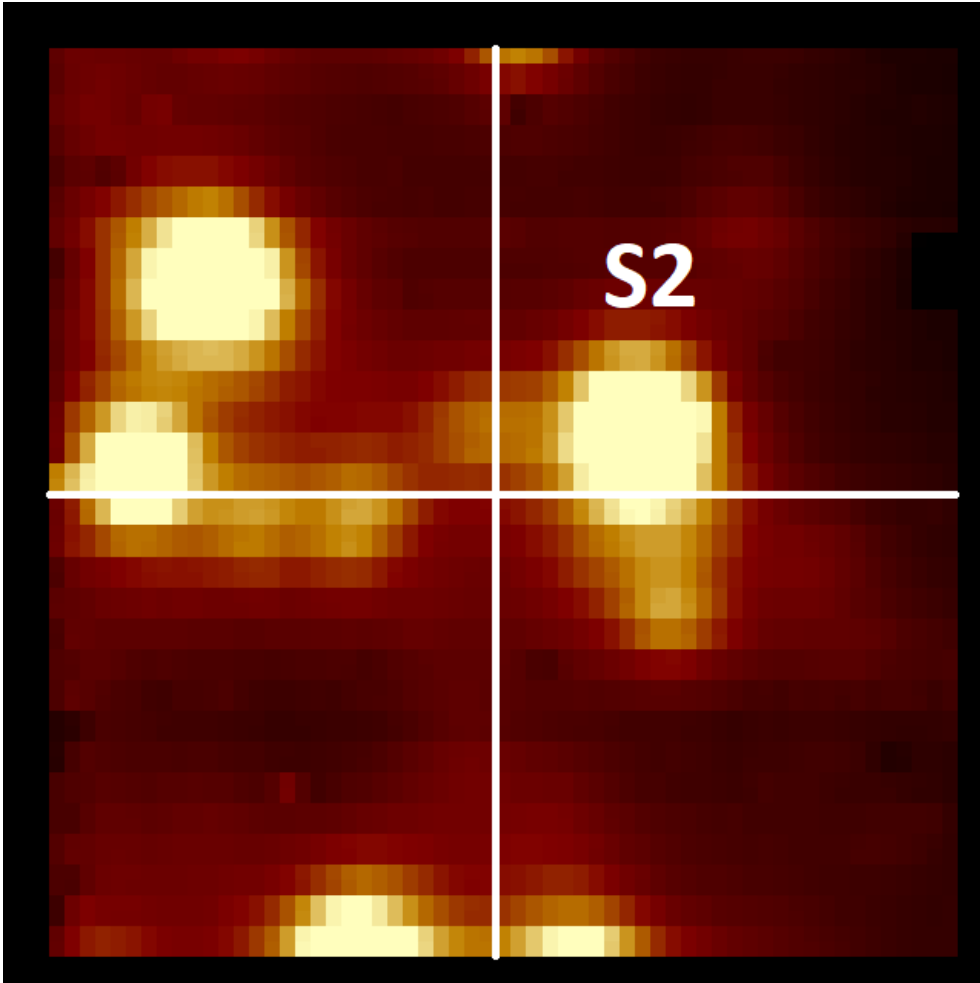
Figure 3.7: *This K-band image of the Galactic center is extracted from a single data cube that is observed with the H+K grating in March 2014. The exposure time is set to 400s. No corrections are applied. The weather conditions during the observations were exceptionally good with a K-band seeing less than* 1".0 *and a coherence time of more than* 2ms. *This is reflected in the FWHM of S2 where* RA = x = 5.6 px *and* DEC = y = 6.0 px. *The white cross imitates the pointing cross of the fast reduction screen of SINFONI. The star S2 is placed in the upper right quadrant. The bright stars on the left border of the field of view are S4 and S5. The two more fainter stars directly under the horizontal white line are S14 and S20. The two stars on the lower border, which are not completely in the FOV, are S1 and S22.*

servation Block (OB) where the observer can choose different templates. The software is provided by ESO and offers a Graphical User Interface (GUI) that helps with the creation of the OBs. Different templates like AO and non-AO assistance, natural guidance star setup, science definition, and the acquisition preparation are included. In the case of the Galactic center, the science template and the acquisition template for an NGS is used. With these OBs, the telescope knows what to do. Therefore, everything has to be set up, like exposure time (400s), grating (H+K), plate scale (0".025), NGS coordinates, offset positions, and the offset style. From the science object (o), the telescope jumps to an empty region to observe a sky (s). For the final data reduction, this sky is subtracted from the science object. Hence, the offset style is oso. With that, one sky is suitable for two science objects. This sequence is then repeated several times. Since the observations start as soon as possible, the observed object is just about the horizon with a high atmospheric airmass. When the object is "moving" to higher altitudes, the airmass gets lower. With that, the conditions get better and it makes sense to open the correction loop and to re-acquire the NGS. This has the practical use of enhancing the observations by over 10% in terms of the FWHM. But this can make the difference between detecting or not detecting a faint object. It is, therefore, crucial to apply this during observations that span over several hours.

Here, the execution of the observations are briefly sketched:

1. Loading the OB, the FOV around the NGS is displayed on the fast reduction screen

2. Selecting the NGS

3. Skipping the re-selection of the NGS in the smaller plate scale since this would introduce an offset

4. Jumping back to the science FOV, increase parallel the plate scale for a better overview and reduce the Detector Integration Time (DIT) to 10s

5. Pointing to S2, simultaneously decrease the plate scale to the smallest setting and increase the DIT to at least 100s

6. Shifting S2 to the designated position, start parallel the observations

In the worst case this process can take up to several hours. Since the observation time is limited, they could be already over before they begin. Doing every step with a certain sensitivity is crucial. With that, the acquisition time can be reduced to ~ 20 minutes.

Weather conditions

In total, there are over 15 different observation runs with the Very Large Telescope that are executed between 2014 and 2017 by the author of this publication with several days of pure observing time. The runs are listed in the appendix. During that time, various weather conditions took place. As it turns out, the weather is not as stable as one would expect since low humidity ($\leq 10\%$) and the hydrostatic head ($< 10\frac{\text{mm}}{\text{year}}$) is remarkably low. During the mentioned time, strong effects of El Nino, a weather phenomenon, took place. A drop in pressure leads to a strong increase in wind velocity. As a consequence, the telescope had to be closed several times in 2014 and 2015 and the number of possible observation nights decreased compared to the previous years. The biggest influence for the near-infrared

Figure 3.8: *The view from the ESO hotel/Residencia at the Atacama desert in the west direction towards the sea. On the right, Cerro Paranal with the VLT is visible. As a rule of thumb one could say: Beautiful sunsets = Bad observations. In this night, the observations were canceled due to bad weather conditions.*

observations in the Galactic center from the weather and atmospheric conditions is due to the movement of the atmosphere itself. The so-called coherence time is a direct indicator for turbulences in the air layers. Often, astronomers validate the quality of observations by the seeing. This can be misleading since the seeing is measured in the 500 nm wavelength regime far away from the infrared ($\sim 2.2\ \mu$m). It is not an appropriate value to quantify the observations (see Martinez *et al.* 2010 for more information). The coherence time on the other hand always resulted in good GC observations.

Sky variability

The SINFONI manual recommends a 50% total observing time on the object. This, on the other hand, means that the rest is spent on the sky. Of course, the overhead time has to be subtracted but is in the order of a few percents with respect to the total observation time. As a consequence, an observation pattern of oso for the observations is chosen. Here, o refers to the science object, s to the sky. It is afterward subtracted from the science object during the reduction process. The sky is chosen to be an empty region that is fixed during the observations. For the science object, the observations are jittered around the desig-nated source to cover a broader field of view and to avoid detector saturation. That means that the same sky region is subtracted from different science object positions in the field of view: according to the SINFONI manual, the detector delivers a changing line profile for different areas on the CCD chip. But this would result in an over- and under-subtraction of the sky lines. To visualize the problem, Figure 3.9 shows the final spectrum of 4 successive observed sky frames at the position of the DSO. These sky cubes are subtracted from the object cubes. Because of the chosen pattern, every sky cube is used for two object cubes. Unfortunately, the strong variability of the sky lines cannot be corrected by the pipeline.
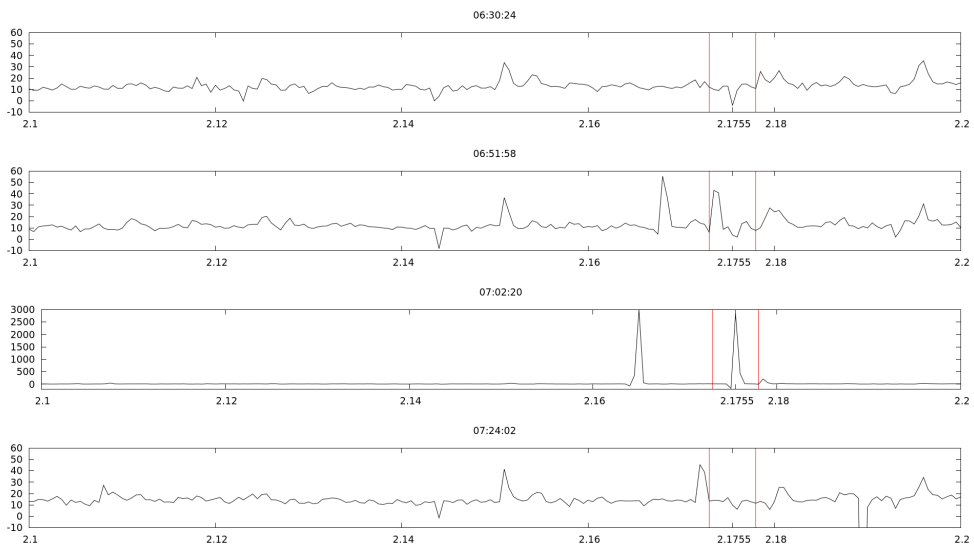

Figure 3.9: *The sky frames are taken from the 2008 SINFONI dataset. The spectrum is ex-tracted from four different single pixel apertures that are at the same position as the DSO in the object cube. The DIT is 600s for each sky exposure and the grating is chosen to be the H+K band. The plate scale is set to 12.5 mas. The displayed spectrum shows the K_s-band. The red lines indicate the width of the Doppler-shifted Brγ line in the object cube. It shows that the emission lines of the DSO coincide with the sky emission lines that are not corrected.*

This is already discussed in detail in Davies (2007). The author state that an over- and under-subtraction takes place. But not only the sky variability is problematic, the strong

sky lines over the Doppler-shifted Brγ, HeI, and Paα are also difficult to model. Figure 3.10 shows some of the prominent sky lines. The red bars mark the wavelength regions where
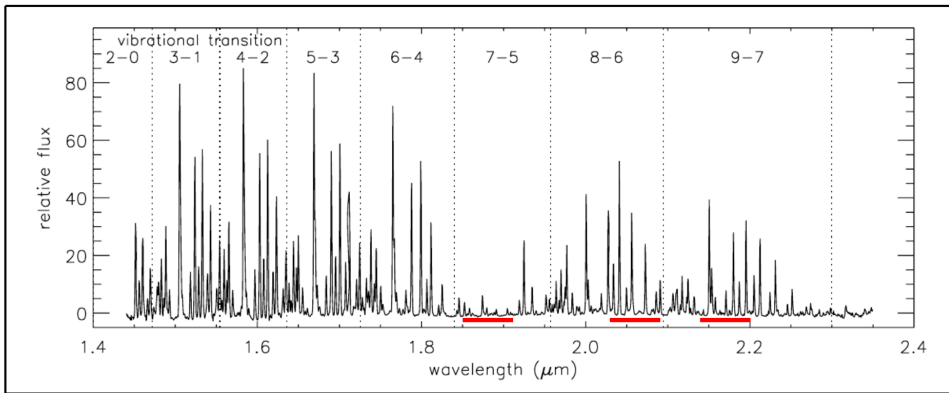

Figure 3.10: *The spectrum of the sky cube is separated by the vibrational transition states. This spectrum shows strong sky lines at the expected DSO emission lines (marked with red bars). The location of these lines imply that a not satisfying correction could influence the DSO emission line. This adjusted figure is taken from Davies (2007), Figure 2, "A method to remove residual OH emission from near-infrared spectra", which is published in the Monthly Notices of the Royal Astronomical Society, Volume 375, Issue 3, pp. 1099-1105.*

the DSO emission lines are observed.

3.3   List of observations

During the time of this analysis, the author of this work traveled many times to Paranal/Chile to execute observations with the Very Large Telescope. This includes the preparation of the observations such as creating OBs, and draw an alternative observation plan for bad weather scenarios. In the following, the executed observations by the author with SIN-FONI at UT4 are listed. For a better overview, just the run-ID and the observing dates are listed.

1. 092.B-0920(A), 26.02.2014 - 27.02.2014

2. 091.B-0183(H), 27.02.2014 - 02.03.2014

3. 092.B-0920(A), 10.03.2014 - 12.03.2014

4. 092.B-0009(C), 24.03.2014 - 27.03.2014

5. 093.B-0092(A), 04.04.2014 - 06.04.2014

6. 093.B-0092(C), 03.10.2014 - 05.10.2014

7. 094.B-0009(A), 03.10.2014 - 07.10.2014

8. 094.B-0009(B), 26.03.2015 - 28.03.2015

9. 095.B-0036(A), 12.04.2015 - 16.04.2015

10. 095.B-0036(D), 03.09.2015 - 05.09.2015

11. 096.B-0157(B), 14.03.2016 - 16.03.2016

12. 096.B-0174(A), 22.03.2016 - 23.03.2016

13. 097.B-0216(A), 27.05.2016 - 29.05.2016

14. 097.B-0216(B), 18.09.2016 - 19.09.2016

15. 097.B-0216(B), 24.09.2016 - 25.09.2016

16. 098.B-0214(A), 12.10.2016 - 14.10.2016

17. 098.B-0638(B), 15.03.2017 - 16.03.2017

18. 098.B-0638(B), 17.03.2017 - 18.03.2017

19. 098.B-0638(B), 19.03.2017 - 20.03.2017

4

METHODS

For the reduction of the data, the SINFONI pipeline provided by ESO is used. Unfortunately, the pipeline reduce the data only to a certain level of precision. A more exact result can be achieved by post data correction. This chapter will explain the problems and the applied methods to minimize the issues that are created on the detector level. Additionally, the image processing tools are introduced that are used for the analysis.

4.1 Data reduction

Observational data does not come in a complete and final form but rather with a set of different calibration files. Before the actual data can be analyzed, the science data needs to be calibrated and corrected with these files for external and thermal effects. This calibration and correction process is called data reduction and is described in detail in Modigliani *et al.* (2007) for the SINFONI instrument. Gasgano is the used ESO GUI. In the following, the calibration files are described.

1. Dark frames:
   To correct for hot pixels, i.e., pixels that do not linearly correlate with the incoming light and seem to be brighter compared to other pixels, dark frames are observed. The telescope is closed and the dark frames are measured with the same exposure time as the science observations. With this, the dark current of the pixel-to-pixel variations can be determined as well as the thermal background noise.

2. Linearity lamp frames:
    The linearity lamps are measured for every grating in a lamp-on/lamp-off pattern. The goal is to keep a record of the pixel-to-pixel response as a function of the flux intensity. The frames are collected in the adaptive-optics hardware house where different PenRay-lamps are installed for calibration purposes such as Xenon, Argon, Neon, and Krypton.[1]

3. Flat lamp frames:
    Flat frames in combination with the dark frames and the linearity lamps measure the pixel-to-pixel variations of the detector. That includes the number of bad pixels, the fixed-pattern noise, and the lamp efficiency. Therefore, the master bad pixel map contains hot and non-linear behaving pixels.

4. Distortion frames:
    These frames are observed to determine the slit-to-slit distance and the spatial distortion on the detector. Since these values should in principle be somewhat constant, distortion frames are recorded only every 30 days. In reality, this can differ slightly due to maintenance work or environmental circumstances (weather, earthquakes). As it turns out, the robustness of this quantity is stable and also 60 days old distortion frames deliver reasonable results.

5. Arc lamp frames:
    When photons hit a detector with a particular wavelength and therefore channels, the device does not "know" which frequency is connected to the channel. Hence, the arc lamps are needed to calibrate the detector since the wavelength of the four lamps is known. With this information, the available channels are translated into wavelengths. The finer this calibration process is, the more information one gets out of the observations. Another method would be the use of a laser instead of arc lamps since these devices can deliver a far more discrete wavelength. See Lo Curto *et al.* (2012) for further information.

6. Jittering:
    Even though the jittering is not a part of the calibration, it is part of the reduction. This last step shifts the individual cubes according to their coordinates in an array to their designated position. The final result is a mosaic with overlapping cubes that increase the on-source observation time and decrease the noise. With that, more information and a better overview over the field of view is intended.

As mentioned in the introduction, the calibration process and especially the jittering is not satisfyingly executed by the pipeline. The established correction tools will be presented in the next section.

---

[1]Neon+Argon (K-band), Xenon+Argon (H-band), Xenon (H+K-band), and Argon (J-band)

4.2   Corrections

Data from SINFONI consists of science- and sky-frames. Science-frames are the observation files with the target and the sky-emission of the atmosphere. The sky-frames are files, that are obtained by observing a empty region on the sky. This file can be subtracted from the science file to get rid of the sky-emission lines. Before the data reduction took place, the data is corrected for cosmic rays, bad pixels, and a sinus-shaped pattern that is caused by the amplifiers of SINFONI that can be found in several slits of the raw science file. Please also consider Smajić *et al.* (2014). Additionally, the jittering process, flat issues, and telluric absorption are corrected.

Pre-reduction tools

Cosmic rays

To correct for cosmic rays that are especially problematic when observing with high exposure times (400s and 600s), the algorithm of Wojtek Pych (Pych 2004) is used. The algorithm divides the frame into smaller sub-frames. In these sub-frames, the standard deviation as a function of counts is calculated:

$$\sigma = \sqrt{\frac{\sum c_i{}^2 - (\sum c_i)^2/n}{n}} \qquad (4.1)$$

A histogram with the count-distribution is created where the peak is detected. From there, the algorithm searches for gaps in the histogram that are representative of the difference in counts between the distribution of not infected pixel and cosmic rays. Pixels which are above these gaps (i.e. have a higher count number than the not infected pixel) are flagged but not removed.

Sinus pattern

This pattern can be caused by the amplifiers of SINFONI that influence the creation of the wavelength map (Arc lamps). Not every slit is infected by this pattern and additionally, it differs in strength and shape. Therefore, it is not possible to completely get rid of this problem. If the amount of exposures is rather high ($\geq$ 20 single exposures), the effect is damped and loses its weight. Fortunately, after the detection of the DSO in 2011, the interest increased and the number of observations covers this effect in a satisfying manner.

Bad line removal

Even though ESO implemented this code already in the pipeline itself, it should be mentioned at this point. The bad line removal code corrects the science and calibration files for lines which are created on the detector level. These lines are not the sinus shaped pattern, but rather a line of hot pixels. For bright and luminous objects, this effect is negligible.

Since the investigated object is neither bright nor luminous (compared for example with S2 that is also in the field of view), this effect can influence the detection of the DSO.

Post reduction tools

After the applied pre-reduction tools and the data reduction, additional steps need to be made to decrease the likelihood of confusion.

Quality control

Since the weather conditions and the performance of the telescope, as well as the execution of the observations, are not constant factors, the quality of the observations is also not constant. Conservatively, the quality of the Galactic center observations close to Sgr A* can be determined by looking at the FWHM of S2. By comparing all the reduced data from SINFONI between 2006 and 2016, values for the FWHM of S2 close to x = 5 px and y = 5 px are considered as high-quality data. Between the range x = 6 − 7 px and y = 6 − 7 px can classified as good data. Everything above these values, a careful case-to-case decision is needed. Some observations show an elongated PSF. With that, even observations under good conditions can look worse compared to observations with bad conditions. The origin of this PSF behavior is unclear. It can be speculated that the not adjusted Natural Guid Star (NGS) is responsible for this effect. A possible workaround is presented in section 3.2.

Flat field correction

To correct for bad pixel-to-pixel variations on the detector, a flat field correction is applied. Every single data-cube is checked by hand to identify the bad line positions that shows magnitude variations that are created at the detector level. These lines are then multiplied by a factor that reflects the magnitude of the variation.

Reference frame

The data is analyzed by years. Hence, the individual data cubes that fulfill the quality control are combined into a final cube. Except in the year 2014 when the DSO goes through the peri-center with the detection in the red- and blue-shifted Brγ wavelength regime. It is required in data that is divided in pre- and post peri-center data-sets. To maintain high-quality results, the combination procedure of the individual cubes to a final cube with the SINFONI pipeline is highly unsatisfying. For that, the best data-cubes of every year are picked to create a 100 × 100 pixel wide reference frame that includes S2, S4, and S10. These can be found in the extended field of view. Now, every single cube is checked for the coordinates of one of these stars. With the reference frame and the positions of the three stars, the individual data cubes are shifted according to the coordinates. With that, a satisfying combination of the individual cubes is guaranteed.

Flagging

In some of the individual data cubes, the borders show a non-linear behavior. By cropping these regions, false signals can be avoided. Since the data cubes are shifted and then stacked, hot pixels from the border could be placed anywhere in the field of view. Therefore, the approach of removing the infected regions in the single cubes is justified. Additionally, cosmic rays and the bad pixels can be corrected with this script. By the simple approach of comparing the medians of certain regions, the bright or hot pixels can be identified and removed.

Telluric correction

Observing in the infrared and especially in the H-band, the spectrograph of SINFONI detects not only the spectrum from the science object but also atmosphere self-induced emission and absorption features. These prominent lines between $1.8\,\mu m - 2.0\,\mu m$ can be seen in Figure 4.1 and are coming from molecules like, e.g,. water (see Carter *et al.* 1992). Since the Doppler-shifted Paα line can be found in the telluric emission region, a correction is sufficient to analyze this line. For that, the spectra of 4 stars are used. For the extraction of the spectrum, the uncorrected data cubes are separated and combined by days. The higher the amount of data, the more variations of the spectrum can be covered. Specific rest wavelengths like e.g. the Brγ line at $2.1661\,\mu m$ are removed by fitting a polynomial function to the continuum. Overplotting the selected rest wavelengths leads to a cleaned star spectrum. The telluric emission lines can then be singled out by comparing the polynomial fitted continuum with the spectrum of the stars itself. The outcome, the telluric spectrum, is then used again to correct the spectrum of the whole data cube. In Fig. 4.2, a corrected S2 spectrum is shown. As mentioned before, the variations of the single cubes in the infected wavelength regions can be fitted with higher accuracy with more data.

4.3   Analyzing tools

Next to the spectral analysis for faint sources, SINFONI also offers a simultaneous imaging mode. To enhance the Signal-to-Noise ratio, different methods like a (low iterations) Lucy-Richardson deconvolution or High-Pass filtering can be applied.

Lucy-Richardson deconvolution

For extended image analysis, the Lucy-Richardson algorithm is used. This iterative low pass filtering process calculates and rebuild the original image (I_{orig}) information of every pixel of the input image. In this case, it is a K-band continuum image ($I_{observed}$) of the Galactic center region around Sgr A*. The original image itself is a composite of point sources that is polluted by a point spread function (PSF). The PSF is the result of the Earths atmosphere and other external factors like, for example, the limited size of a telescope.
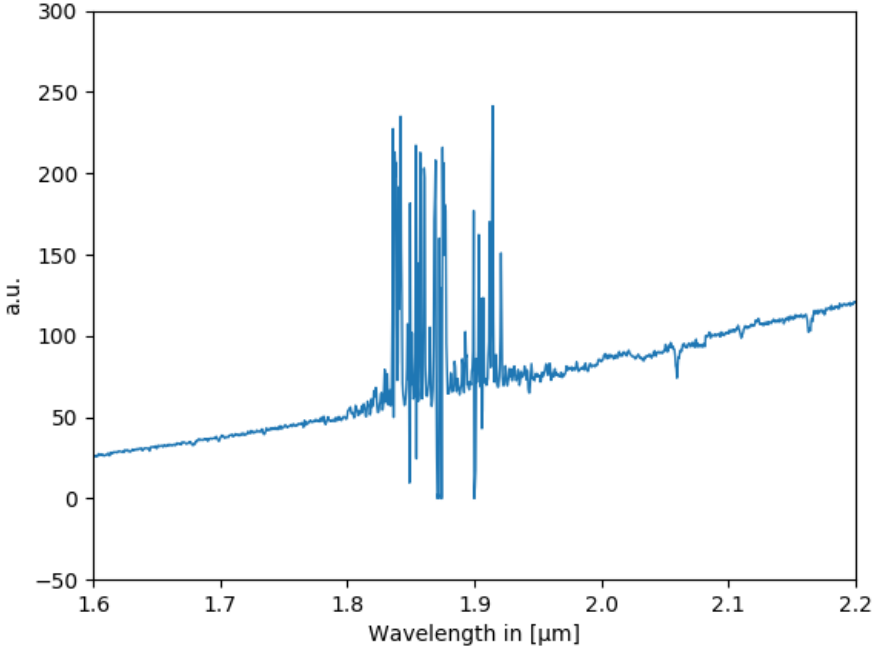
Figure 4.1: *This is a spectrum in* μm *from the S-cluster star S2 of 2008 in arbitrary units (a.u.). The data cube is a combination of 21 high-quality single data cubes with an exposure time of 600s/cube. In total, the final data cube can offer an exposure time of 3.5 hours. The shown spectrum is extracted with a 3-pixel radius wide aperture without continuum correction since the telluric correction does not deliver satisfying results. An analysis of the Paα line that is spectrally located in the telluric wavelength range (1.8 μm − 2.0 μm) is excluded. The reason is the high chance of confusion.*

Therefore, the image is "blurred" since every point source is spread by the PSF. The wings of these PSF also add additional noise to the image. The observed image can be described with

$$I_{observed} = I_{orig} \otimes PSF \tag{4.2}$$

where the original image is convolved with a PSF. The image itself consists out of pixel[2] $\sum \mu$ at a random position j. For the observed pixel distrubtion follows

$$\mu_i = \sum_{i=1}^{m} y_i \, p(i, j) \tag{4.3}$$

where y_i is the "true" pixel value without the influence of an PSF and p(i,j) the emitted photon from its origin i at the observed position in the image at j. Hence, the factor p(i,j)
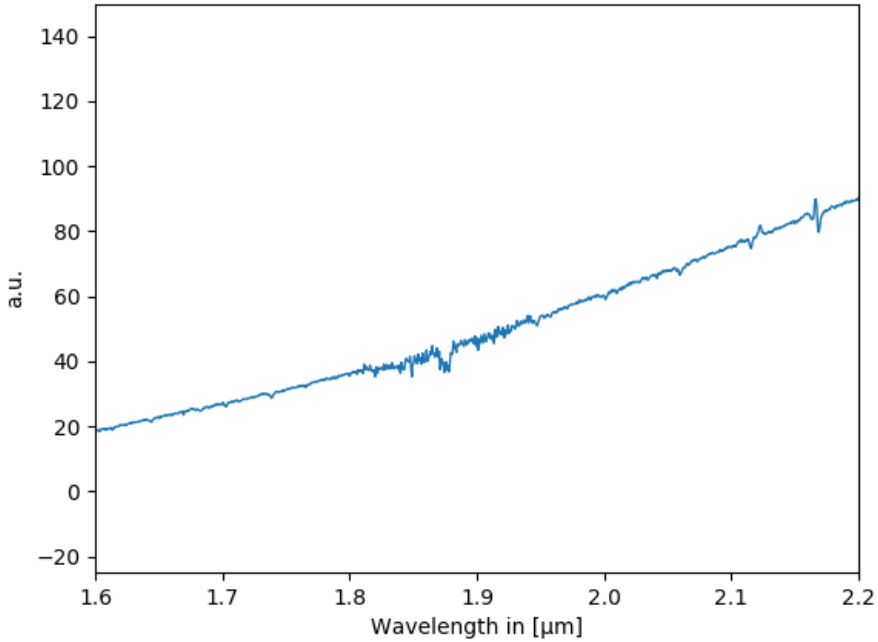
---

[2]SINFONI data cubes have 64 × 64 pixel

Figure 4.2: *This spectrum is again from the S-cluster star S2. The data cube from the 2013 observations consists out of 176 single data cubes with a combined exposure time of almost 30 hours. With this amount of high-quality data, a correction of the telluric emission lines is easier since the variations in the infected wavelength region can be corrected more precisely.*

denotes the PSF of the observing system. Since Equation 4.3 can be described with a Poisson distribution, it is

$$z(i, j) \sim Poisson(y_i p(i, j)) \tag{4.4}$$

where $z(i, j)$ again defines the observed pixel distribution. This distribution can now be convolved with a PSF $P(i, j)$ that is either extracted from the image or artificially constructed. This is the most important step of the algorithm since the quality of the PSF is directly connected to the final outcome. The observed distribution can now be written as

$$\Gamma_n = z_n(i, j) \otimes P(i, j) \tag{4.5}$$

where n gives the iteration number and Γ the new image. This can now be compared to $I_{observed}$ with

$$R(i, j) = \frac{\Gamma_n}{I_{observed}} \otimes P(i, j) \ . \tag{4.6}$$

In Equation 4.6, $R(i, j)$ is the correction function that results in a noise reduced image. High frequencies usually are connected to noise. Following this, the convolved result is low-

pass filtered where high frequencies are blocked. If now the correction function R(i, j) is applied on the distribution $z_n(i, j)$, the outcome results in a low-pass filtered image. This is reflected by

$$z_{n+1}(i, j) = R(i, j) \cdot z_n(i, j) \ .$$ (4.7)

It is important not to use a high number (n > 10000) of iterations since the algorithm tends to create point sources out of noise or combine the flux of neighboring objects to one source. Therefore, a low number (n < 100) of iterations or the physical background knowledge can be helpful to interpret the results. However, the sensitive process of constructing a PSF remains the most important part of the process.

Channel maps

Since the continuum dominated data-cubes represent just one way of analyzing the observations, it is interesting to know what other information can be extracted from them. Looking at single wavelengths (or channels) can reveal interesting details about the data. Figure 4.3 shows the selected Brγ rest wavelength at $\lambda = 2.1661 \ \mu m$ with the subtracted continuum. It reveals a structure that is hidden beneath the continuum. On the other hand, Figure 4.4 shows the same field of view but without the continuum subtraction. It is an image of the complete wavelength range of SINFONI in the H+K band (1.45 μm − 2.45 μm). To achieve a clean continuum subtraction, a polynomial fit to the spectrum and the subsequent subtraction by it leaves just (non continuum related) emission lines. These lines are usually Doppler-shifted from the rest wavelengths. Lines of this nature originate in objects, that are moving either away or towards the observer.

Aperture photometry

Extracting the flux information of the DSO to calculate its magnitude can be done by using aperture photometry on the deconvolved Lucy-Richardson K-band images. In order to extract the magnitude of the DSO, S2 is used as a reference star with a magnitude of 14.15± 0.06 in the K-band. The ratio between S2 and the DSO can be obtained by applying an aperture with a local background subtraction on these two objects. The flux of the DSO can then be calculated with

$$Flux_{DSO} = \frac{Counts_{DSO} * Flux_{S2}}{Counts_{S2}} \ .$$ (4.8)

The error is calculated by placing 30 one-pixel apertures around the DSO in the images. By calculating the standard deviation of the apertures, the sigma of the background can be estimated. Multiplying this by the square root of the pixel number of the DSO aperture leads to the error for the counts. Transferring this value gives the error for flux and magnitude. Additionally, Sabha *et al.* (2012) investigate the close vicinity of the SMBH and point out, that the chance of detecting a blend star is around 30% − 50% and that the density of faint main sequence stars below the detection limit could be significant high towards Sgr A*. The authors derive a KLF (K-band luminosity function) slope of $\alpha = 0.18 \pm 0.07$
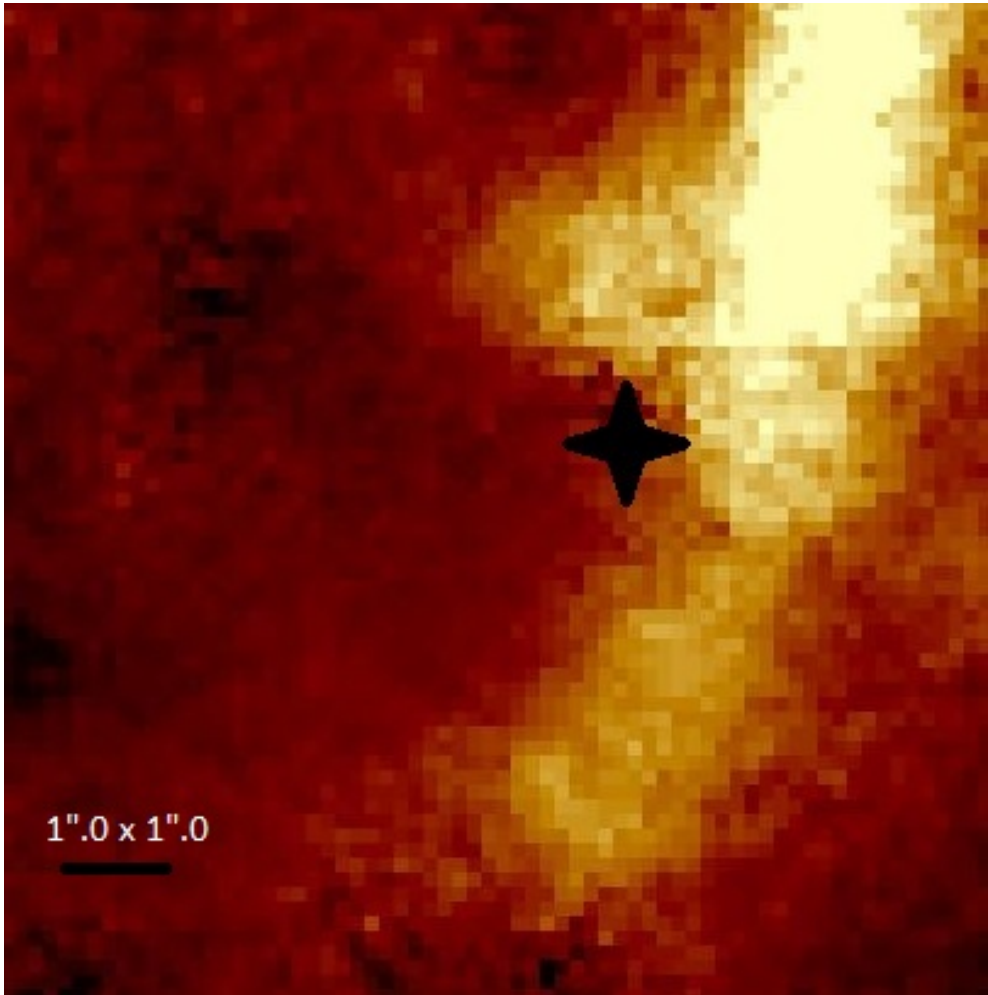
Figure 4.3: *A line map showing the isolated Brγ rest wavelength extracted from the data cube of 2013. The black cross marks the approximate position of Sgr A*. The bright arm shows the background emission of Brγ at* 2.1661 μm. *The field of view is centered on the S-cluster.*
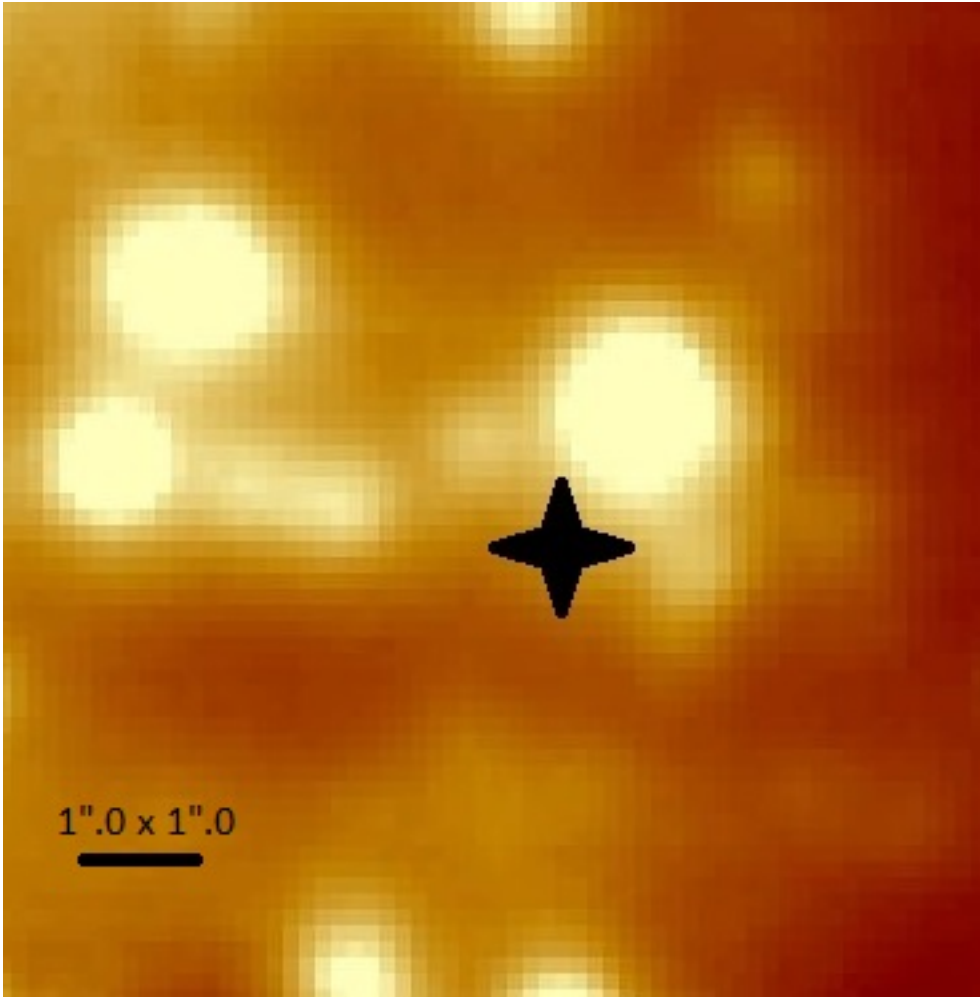
Figure 4.4: *A continuum image of the S-cluster. The H+K-band continuum image is extracted from the data cube of 2013 and shows the same field of view as in Fig. 4.3. Sgr A* is located approximately at the position of the black cross. The bright star above Sgr A* is called S2.*

which is related to a linear behavior between the number of stars and the K_S magnitude. Since the DSO faces several varying background scenarios towards Sgr A* and hence a high chance of creating a blend star, the derived magnitude and flux can only be interpreted as an upper limit.

Position-velocity diagram

Another way of investigating the data is the analysis of the flux along the orbit of the DSO. This procedure is a function of distance to Sgr A* in combination with the velocity. This can reveal extended shapes of the object and visualize complex connections. Gillessen *et al.* (2012) show a position-velocity diagram for 2008 and 2011 (see Figure 2.10) to underline the assumed gaseous nature of the object. One way of creating these diagrams is the mentioned flux investigation along the orbit. An important parameter is the slit size, which is placed along the trajectory. Using over sized slits can lead to false results since the emission of other sources could be included and misinterpreted. Additionally, a matching background subtraction by placing other slits next to the orbit-slit is sufficient. In contrast to the Paα emission, the Doppler-shifted Brγ wavelength regime is confusion-free due to the lack of interfering atmospheric telluric features. It is therefore a favorable strategy to use the Doppler-shifted Brγ line for creating position-velocity diagrams. In contrast, the HeI variations over the years between 2006 and 2015 make an analysis unfavorable because of the worse S/N ratio. Also, the line can not be detected in some years.

Orbit

To create position-velocity diagrams, it is important to derive a proper orbit. It is achieved by using the 4th-order approximation Runge-Kutta method (see Runge 1895, Kutta 1901). Compared to the Euler method (Hairer *et al.* 2008), this procedure solves differential equations more precisely. The basic idea is, that small variations to the initial conditions are applied and adjusted over a recurrence formula. For the initial conditions

$$x = x_0, \ y = y_0 \tag{4.9}$$

follows

$$\frac{dy}{dx} = f(x, y) . \tag{4.10}$$

With

$$y_{n+1} = y_n + h T_4(x_n, y_n, h) , \tag{4.11}$$

the mentioned recurrence formula can be defined. Also, h is the size of the variations that are applied around the initial conditions. These variations are calculated with the term T_4 that is described by

$$T_4 = \frac{1}{6}(k_1 + 2k_2 + 2k_3 + k_4) \tag{4.12}$$

where

$$k_1 = f(x, y) \tag{4.13}$$

is just the intial equation. Following this,

$$k_2 = f(x + \frac{h}{2}, y + \frac{h}{2} k_1) \tag{4.14}$$

defines the next approximation step where half of the step size h is added to the initial conditions. It is worth mentioning it, that k_1 appears in the y parameter of k_1. Now,

$$k_3 = f(x + \frac{h}{2}, y + \frac{h}{2} k_2) \tag{4.15}$$

uses the same step size h. Instead of k_1, k_2 is used for the iterative process. Finally,

$$k_4 = f(x + h, y + h k_3) \tag{4.16}$$

uses the full step size and k_3 to calculate a precise approximation.

With this method, the orbit with a starting point in 2005 can be precisely calculated. By running the process several times, the best matching orbit of the DSO can be chosen from a set of results.

4.4 QFitsView

QFitsView is used for most part of the analysis of the data. This GUI is an easy way to handle and manipulate the 3d data-cubes of SINFONI. It is based on the DPUSER computer language (Thomas Ott, MPE Garching, and Eckart and Duhoux (1991)) which includes some useful routines like the Lucy-Richardson deconvolution algorithm or the smooth-subtract method. In Figure 4.5, the graphical interface is shown. The numbered sections are:

1. The window of the QFitsView interface shows the field of view of the data-cube. The contrast and the look-up table (linear, logarithmic, square root) can be changed.

2. In this part of QFitsView, the spectrum of the selected pixel (or aperture) is displayed. It also shows the selected channel. By changing the channel, the observed wavelength is changed.

3. This panel harbors the main features and settings of QFitsView. It shows, for example, the selected channel and the chosen look-up table.
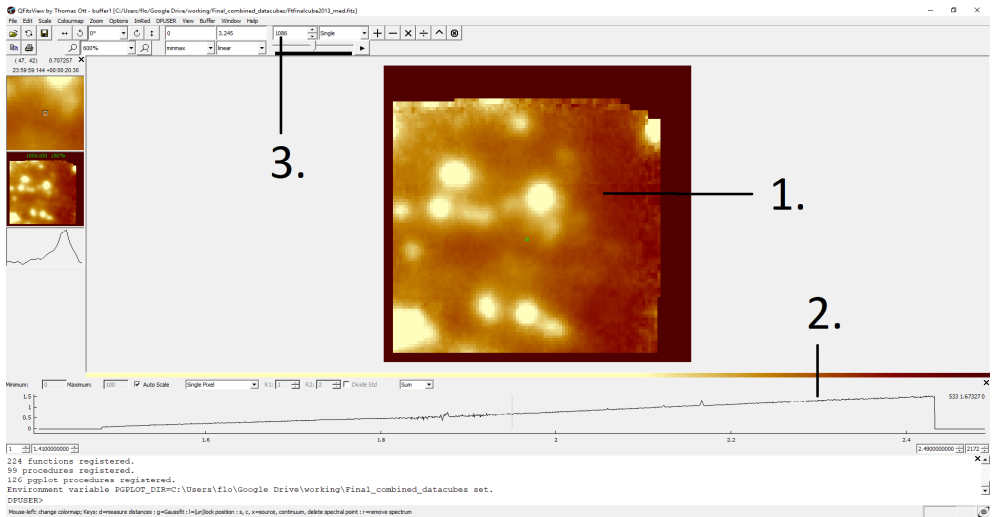
Figure 4.5: *This screenshot shows the QFitsView interface. The field of view shows the Galactic center in 2013 and is placed in a* 100×100 *pixel array with a scale of* 12.5 *mas/pixel. The sections (1-3) of the interface are explained in section* *4.4.*

5

<div align="right">

RESULTS

</div>

In this chapter, the results of the reduced data between 2006 and 2015 including the identification of the DSO in the Lucy-Richardson convolved K-band images of the Galactic center are presented. Line maps are used to verify the position of the investigated object. With that, an orbit can be created. To verify the results of the Lucy-Richardson deconvolved images, K-band images are shifted and stacked. Therefore, the identification of the DSO in the continuum is possible. Additionally, magnitude and flux of the DSO can be extracted by applying aperture photometry. The evolution and the claimed brightening of the DSO is discussed.

Line emission images of a faint infrared excess source

The presented Brγ line images in Fig. 5.1 show the emission of a red-shifted (between 2006 and 2014.3) and blue-shifted (between 2014.4 and 2015) compact K-band source that is moving on a Keplerian orbit around Sgr A* with a comparison of the continuum contours of the S-stars. The specific wavelength and the resulting velocity can be found in Table 5.1. 2014a is defined as the time before the periapse, 2014b as the time after the pericenter passage. The circle around the DSO represents the beam size of UT4. Objects that are smaller than this diameter are compact. The FOV covers around 0".8 × 0".8 and is focused on Sgr A* that is always at the position of the magenta-colored cross. Because of the noise and subtracted continuum, the overall shape and radius of the DSO undergoes some variations between 5% − 10%. The unstable weather conditions and the variable amount of data per year are reflected in the Signal-to-Noise ratio. The quality is decreased at the border of the final data cube due to dithering (i.e., statistical) and slit recombination effects. This can

<div align="center">53</div>

Date (YYYY)	Wavelength (μm)	Velocity (km/s)
2006	2.1740	1108.03
2007	2.1742	1121.83
2008	2.1747	1191.08
2009	2.1755	1307.41
2010	2.1767	1475.69
2011	2.1777	1613.49
2012	2.1800	1925.81
2013	2.1817	2166.79
2014a	2.1847	2583.67
2014b	2.1430	3198.60
2015	2.1499	2230.50

Table 5.1: *The detected Brγ wavelength and the resulting velocity of the Dusty S-cluster Object between 2006-2015.*

also be observed in the individual exposures that makes a centering on the DSO during the observations necessary. Following this, the single exposures during the observations are jittered around the expected position of the DSO in a 0".1 window. As a result, the DSO region has the best Signal-to-Noise ratio because of the highest number of overlapping single exposures while regions at the border of the final data cube show a decreased S/N ratio. The red-shifted and blue-shifted Brγ emission are marked with white dashed circles. An interesting and important feature in 2012 can be detected: since the observations start in 2012.21 and stop in 2012.8, the covered time spans over a wide velocity range. As a result, the velocity of the DSO is around 1750 km/s at the beginning of 2012 and about 2050 km/s at the end of 2012. Combining this dataset leads to an effect that is interpreted as a velocity gradient over the source, i.e., the velocity over the DSO and the emission area is lower downwards the orbit and higher towards the black hole. Because of this effect, the conclusion could be a not stable nature of the object, for example a gas cloud. In Table 5.1, the velocity value for 2012 is an average between 1786.62 km/s and 2065.00 km/s. Figure 5.2 shows an example for a size comparison between the line map emission and the continuum.

Distance to Sgr A*

For every dataset until 2014a (2014.35), the resulting line maps presented in Fig. 5.1 are showing a red-shifted Brγ emission that is moving with an increasing velocity towards Sgr A*. After 2014.45, a blue-shifted Brγ emission which is moving away from the central black hole can be detected in the line maps. By applying a two-dimensional Gaussian

Figure 5.1: *The Doppler-shifted Brγ line detection of the DSO between 2006 and 2015. In 2009, the field of view of the data does not cover the whole* 100×100 *pixel image.*

fit to the position of the DSO in the line maps, the distance with respect to Sgr A* can be extracted. The determination of the position of Sgr A* will be explained in the next section. This fitting technique is followed by a variation of errors, mainly because of the noise, the continuum subtraction, the local background situation, and the non constant number of observations for every year/dataset. Since the detection of the source itself is close to the detection limit of SINFONI, it is reasonable to assume that some of the flux of the DSO can be confused with the noise or is mixed with the subtracted continuum. The derived Brγ line distances in Table 5.2 are an upper limit with a spatial centroid peak variation of ±0.5 pixel that can be translated to ±6.25 mas. This value can be justified because of the high accuracy of the center of gravity in every dataset. Fitting repeatedly different sized Gaussians, that also take account of extended emission that is close to the noise level or above, delivers results that are consistent with the given error.

Identification of the DSO/G2 in the Lucy-Richardson reconvolved images

The main problem with the identification of the DSO in the line maps is the lacking opportunity to compare the source to the other known stars in order to do aperture photometry. The failed K-band detection in Gillessen *et al.* (2012) results in the proposed gas-cloud
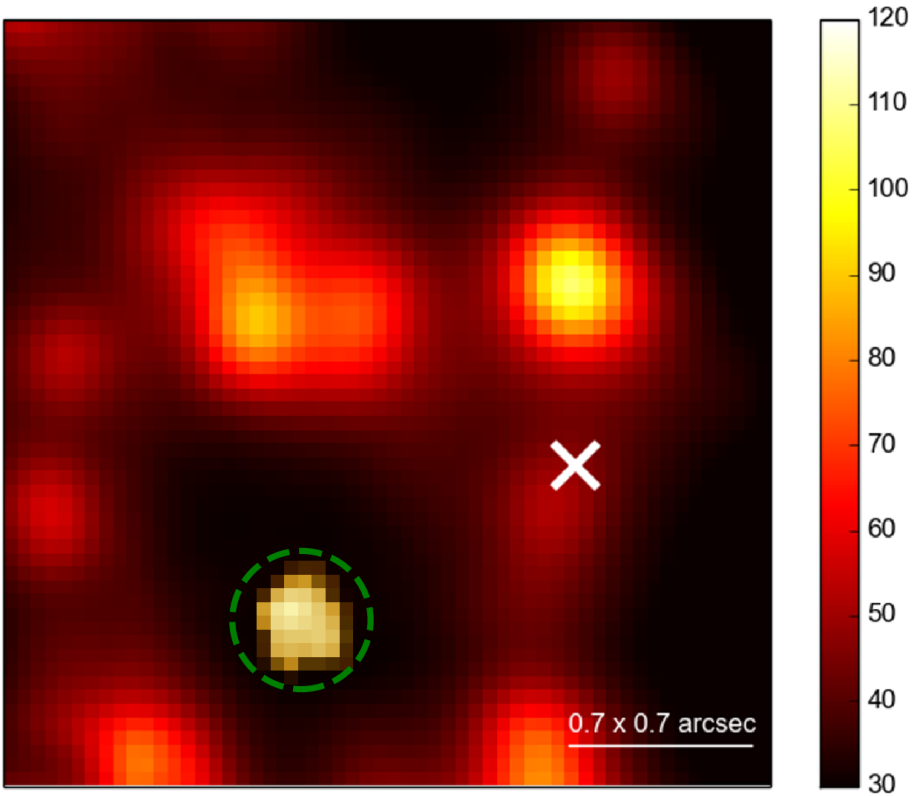
Figure 5.2: *Brγ line detection of the DSO in 2006. It is located in the green dashed circle. Sgr A* is at the location of the white cross. The Brγ line map emission is copied into a K-band continuum image. The color bar is scaled to the stars but not to the DSO. The scale of the field of view is* $0".7 \times 0".7$.

model. If the Lucy-Richardson algorithm is applied to the K-band data, no source would be detected because of the not existing flux information at the position of the DSO. Hence, the motivation of using the LR algorithm is given. If a detection with the Lucy-Richardson algorithm is possible, it would result in the magnitude/flux extraction and the detection of the source in the continuum. From the average H+K-band data cubes, images that show the Galactic center around S2 and Sgr A* are extracted. S2 is the brightest and most iso-lated star in the field of view. Since the Paα line could increase the confusion, the spectrum is limited on the K-band between 2.02 μm and 2.24 μm. These collapsed data-cube images include in addition to the prominent Brγ line also the less intense HeI emission. Unfortu-nately, the Galactic center in the investigated region is crowded by many objects like S62, S64, S17, S40, and S20 in a way, that the PSF of S2 shows superpositions of these mentioned

Date (YYYY)	Distance (mas)
2006	237.00
2007	190.25
2008	183.75
2009	186.00
2010	148.87
2011	131.25
2012	127.12
2013	93.37
2014a	47.75
2014b	34.75
2015	67.00

Table 5.2: *The detected distance in mas to Sgr A* based on the Doppler-shifted Brγ emission line between 2006-2015. The distance decreases till 2014a and is based on the red-shifted emission. In 2014b, no red-shifted emission of the DSO can be detected. The DSO moved around Sgr A* and emits after 2014b in the blue-shifted Brγ wavelength domain. As a consequence, the distance in 2015 increases compared to 2014.*

stars. These influences of the surrounding stars are not neglectable and make a profitable application of the Lucy-Richardson algorithm unrewarding. Other stars in the field of view are either not fully observed or suffer from even worse superpositions. Respectively, an artificial PSF with an FWHM of 4.0 px and 5.0 px in x- and y-direction is created. This point spread function is normalized and centered at the related S2 position. Analyzing the PSF of S2 and other sources over the years, reveals an elliptical behavior of the SINFONI instrument that is reflected in the observed beam. Therefore, the created artificial PSF has to follow that pattern. Since this instrument behavior is neither a constant nor a universal effect, different PSFs are created for every year. Some stars at the border show a reduced influence of the elliptical beam. Additionally, the range of the variations of the beam is quite large over the years. The difference of the spatial dimensions (x,y) of the 2006 observed PSF of S2 in the K-band is ~ 0.3 pixel. In 2015, this difference is ~ 1.0 pixel, which translates into 9 mas or 3.5 mpc[1]. The effect is an example to show the importance of handling the creation of the used PSF with high accuracy and attention. After the creation of the PSF, an adjusted background subtraction is applied to the images that are scaled to the local environment of the DSO. To verify the amount of background, some faint S-stars (i.e., S23, S57, and S63) are used as identification factors. The environment of Sgr A* is highly dynamical because of the fast-moving S-stars. Hence, the position of S4 and S5 are used to verify the applied background subtraction. This approach is justified since Valencia-S.

---

[1] With a assumed GC distance of 8.3 kpc follows 1"=40 mpc where 1 pc=3.08×10^{16}m.

et al. (2015) show that a background subtraction from randomly placed apertures can create false signals. Another source of confusion would be background apertures that are far away (≥ 10 pixel) from the DSO. As an example, a spectrum from a position upstream of the orbit of the DSO is presented (Fig. 5.3). Pfuhl *et al.* (2015) and Plewa *et al.* (2017) show red-shifted Brγ lines for the time around the peri-center in 2014.3 with a parallel detection of a blue-shifted Brγ line. This is supposed to underline the gaseous nature of the object since parts of the DSO are torn apart close to Sgr A*. A resulting parallel detection would indeed point to a gaseous nature. However, based the available dataset that covers the periapse in early 2014, a parallel detection can not be confirmed. The presented spectrum in
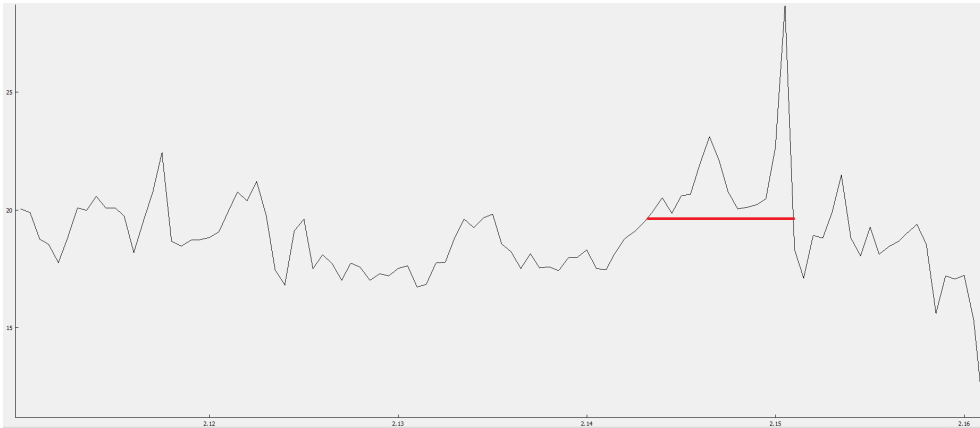
Figure 5.3: *The Brγ line detection of the DSO in 2014.3 just before the closest approach to Sgr A*. This line can be found in the blue-shifted Brγ domain. The width of the line (red bar) is over* 850 *km/s and would be consistent with the reported blue line in* Pfuhl et al. *(2015) and* Plewa et al. *(2017).*

Figure 5.3 is created by using random apertures that are spread all over the field of view. In Fig. 5.4, the connected apertures to the shown spectrum are presented. The green aperture is the expected area of the parallel detection of the gas that is torn apart because of the gravitational forces. The red apertures are the subtracted background. This example shows that because of the inconsistent and bumpy background in the Galactic center (see Sabha *et al.* (2012) for a detailed analysis), signals can be appear or disappear. A combination of a sensitive analysis with background knowledge in physics can minimize these false interpretations.

However, after the creation of the PSF and the subtraction of the background, iterations between 5000 − 10000 and a threshold of 0.000003 is used to deconvolve the images with the Lucy-Richardson algorithm. The threshold setting is due to the sensitive noise behavior of the algorithm. The convolution algorithm is only applied where the count value of a pixel is higher than the threshold setting. Otherwise, it returns a zero pixel value. The implemented routine in QFitsView, a DPuser based GUI (Thomas Ott, MPE Garching, also
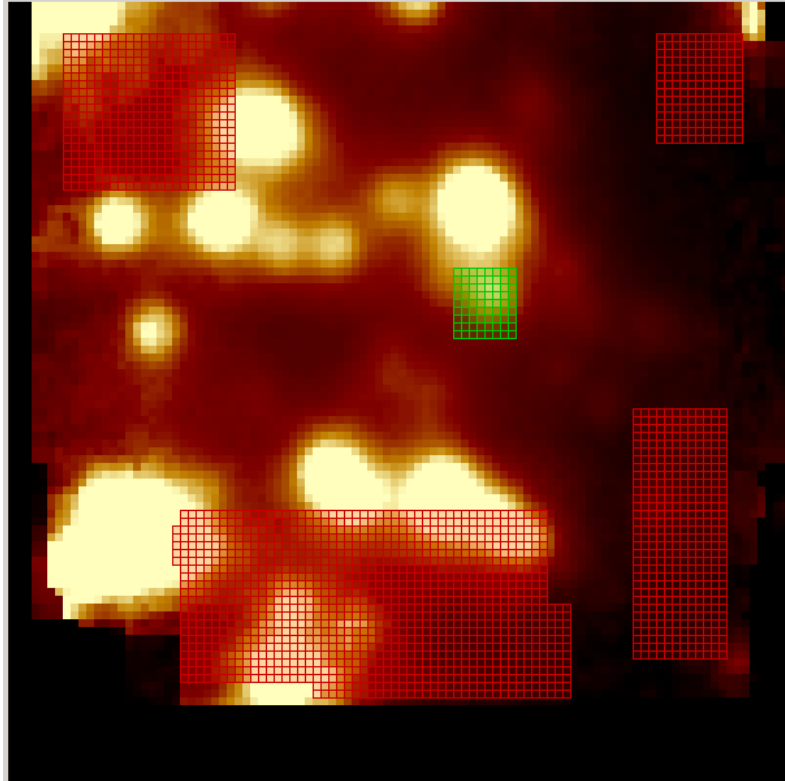
Figure 5.4: *The randomly placed red apertures define the background. The green aperture is placed over the claimed (see Pfuhl et al. 2015 and Plewa et al. 2017) DSO position in 2014.3. The resulting spectrum is shown in Fig. 5.3.*

consider Eckart and Duhoux 1991), is a suitable choice. Some datasets show a striped pattern and an elongation of the S-stars that can be corrected by rotating (45°) the elliptical PSF. This refers to the mentioned problem of the elliptical beam and the changing situation for every year. These images are reconvolved with a Gaussian (kernel size between 4.0 px - 5.0 px) that represents the diffraction limited beam size of the instrument. A smaller PSF for the reconvolving process leads to false results that are reflected in unknown stars or repositioning of known stars like S2.

Determining the distance between the DSO and Sgr A* requires the position of the SMBH itself (consider the former section). For that, every single data cube between 2006 and 2015 is investigated for (weak) signs of a flaring Sgr A*. From these cubes, K-band images can be extracted. On them, the described Lucy-Richardson algorithm is applied. Except for epoch 95 and 96, the exact position of the central black hole and epoch can be extracted from the reconvolved images for every year, since the algorithm creates a point source from the increased flux around the designated area. Because of the orbital distance

of S2 to Sgr A* in epoch 95 and 96, the two sources cannot be distinguished without confusion. For that, a polynomial orbit function of S20, that is defined as

$$\alpha[mas] = (220.8 \pm 0.6) + (-4.94 \pm 0.31)\Delta t \tag{5.1}$$

for the right ascension and

$$\delta[mas] = (109.5 \pm 0.4) + (-6.29 \pm 0.21)\Delta t \tag{5.2}$$

for the declination, can be used. It is introduced by Gillessen *et al.* (2009) and can be used to determine the distance to Sgr A*. By using this approach not only for S20 but also for S4 and S5, the distance to Sgr A* can be derived with an accuracy of ~ 0.5 pixel that translates into 6.25 mas. Therefore, using the fits for determining the position of Sgr A* in 2014b and 2015 is justified. In Fig. 5.5, the continuum identification of the DSO between 2006 and 2015 is presented. The field of view is chosen to be 0".8 × 0".8 and shows the DSO (white dashed circle) in addition to the S-stars around Sgr A*, which is indicated by a black cross. The DSO is clearly located inside the white dashed circle. Because of the lack of high-quality data in 2014b and the distance to nearby stars, the DSO cannot be identified without confusion in the convolved images. However, the position agreement is also represented by the position of the dashed circles around the DSO in the Lucy-Richardson images. They are located at the same positions as in the line images (see Fig. 5.1). With that, the chance of confusion is minimized and it can be concluded that the found point sources in the Lucy-Richardson deconvolved images are not artificially created objects.

K-band detection of all combined epochs

The results of the Lucy-Richardson deconvolved images in the previous section already show a high level of agreement with the integrated deep field SINFONI line maps. To eliminate the probability that the DSO could be a false signal, another approach for identifying the object in the continuum can be applied. Since the flux of the source is low compared to the surrounding stars, it is helpful to stack individual years. With an increased S/N ratio, the chance of identifying the DSO in the K_S-band increases. It is useful to subtract more prominent sources like S2 and S4 from the K_S-band images that are extracted from the final data-cubes. Since the position of the DSO is known from the line maps and the Lucy-Richardson deconvolved images, a shifting vector can be applied. This increases the flux at the DSO position. Every other source leaves a trail. Additionally, the Lucy-Richardson deconvolved images are shifted with the same vector. Figure 5.6 shows the result of stacking several years that are individually centered on the DSO. In the left image the extracted and stacked K_S-band images are presented. The center of the green dashed circle reveals a source that can be identified as the DSO. Since it is located at the same position in the right image, the detection of the point source in the stacked Lucy-Richardson deconvolved images can be confirmed (Fig. 5.5). Both images are independent and represent proof, that the identification in the LR deconvolved images, based on the position of the DSO in the line maps is consistent with the position of the source in the K_S-band continuum. From that follows directly, that the DSO can be detected in the K-band continuum.
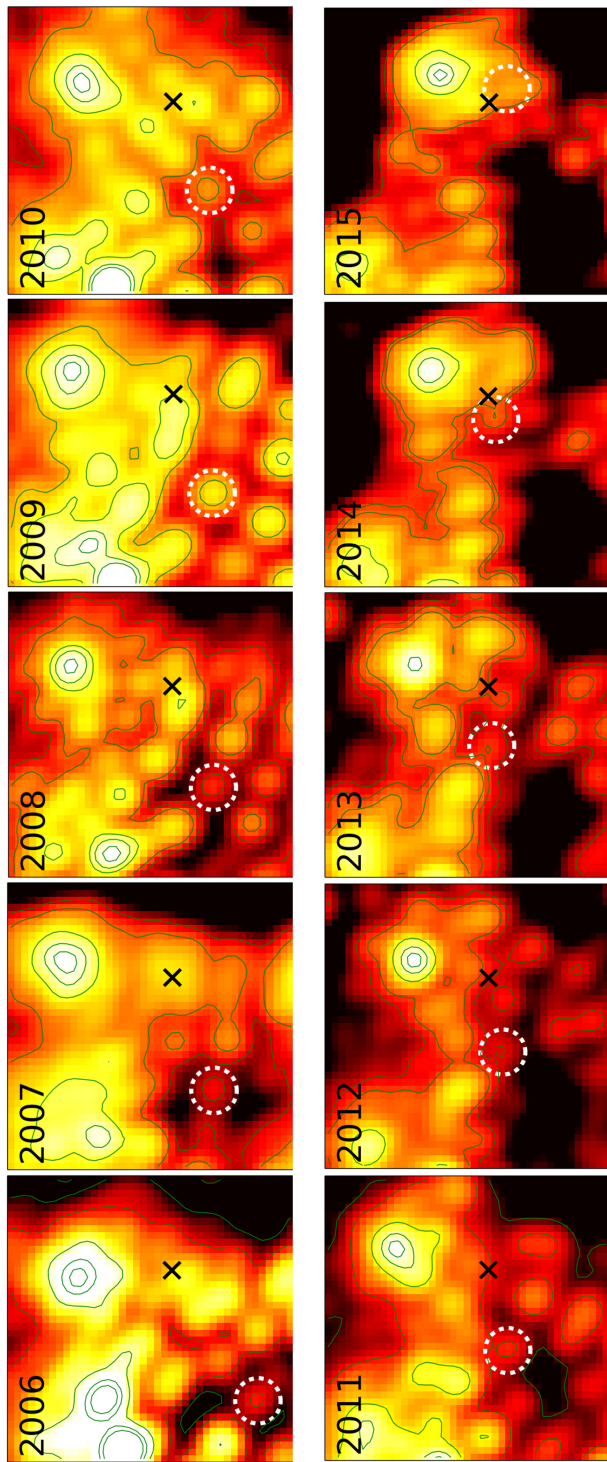
Figure 5.5: *Lucy Richardson detection of the DSO between 2006 and 2015 with a FOV of 0".8 × 0".8 for each figure. The presented image of 2014a is before the pericenter passage of the DSO in 2014.39, 2015 is after the flyby.*
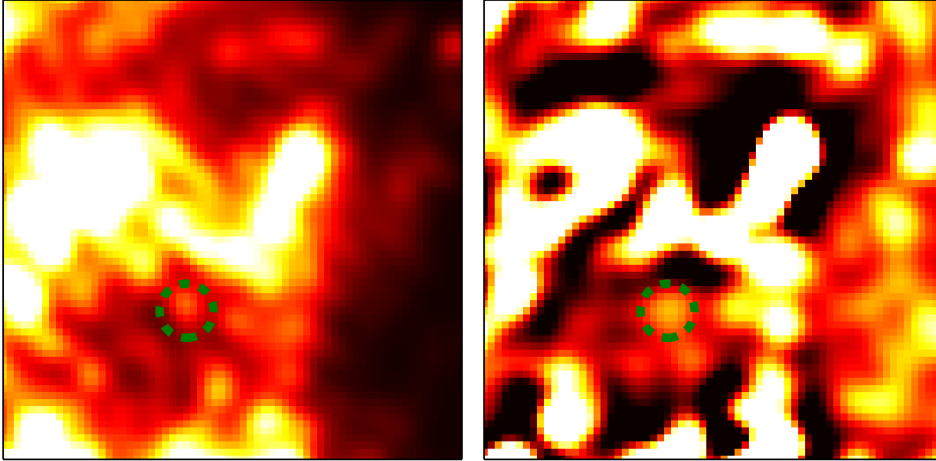
Figure 5.6: *Combination of several epochs between 2006 and 2015. The left image shows the result of combining the shown LR deconvolved images. The right image is the product of combining several data cubes between 2006 and 2015 that fulfill our quality control. In both cases the DSO is marked with a dashed green circle. The FOV is chosen to be $1".0 \times 1".0$.*

Flux and magnitude evolution of the DSO

Because of the clear identification of the Dusty S-Cluster Object in the LR images of the Galactic center, the flux and the magnitude can be determined. As mentioned in the former chapter, the star S2 with a K-band magnitude of 14.15 ± 0.06 is used as a reference star to compare the counts of the two objects. Since the orbit of the DSO and S2 is close to other sources, is is easy to mix flux and magnitude information. To avoid faulty count-information that is polluted by other sources, just the main peak emission with a 1-pixel aperture is used on S2 and the DSO. Extracting the counts leads to the ratio between the two objects. This ratio is the same between the magnitude and the flux of S2 and the DSO. Multiplying the ratio that is extracted from the counts with the magnitude and the flux of S2 results in the same DSO properties. The flux-ratio is transfered to the magnitude with

$$m_{DSO} - m_{S2} = -2.5 \cdot [flux-ratio] \tag{5.3}$$

that leads to

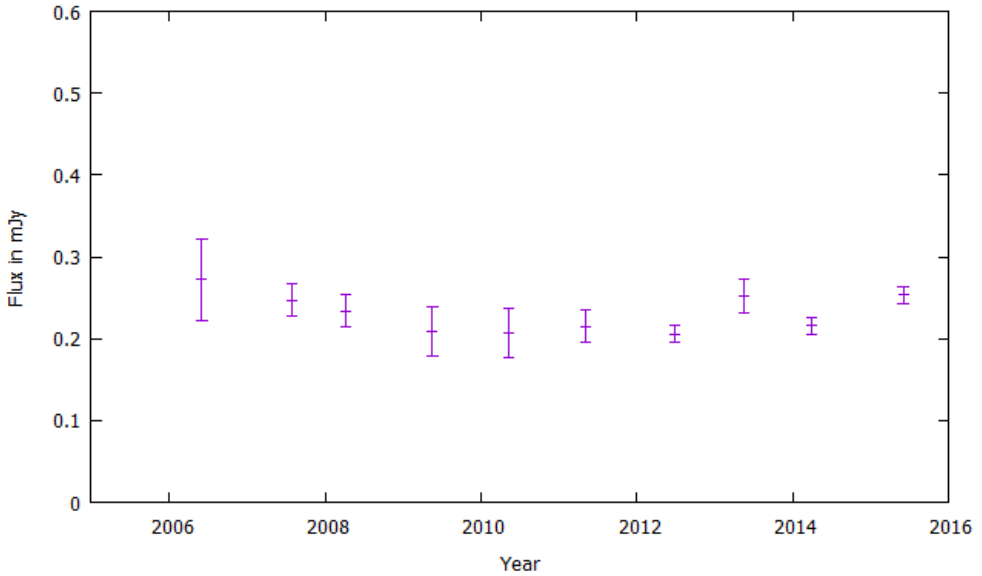$$m_{DSO} = 14.15 \, mag - 2.5 \cdot [flux-ratio] \tag{5.4}$$

Figure 5.7: *The plot shows the flux evolution of the DSO as a function of years. The values are based on the Lucy-Richardson deconvolved images. The error-bars reflect the changing background of the DSO on its trajectory around Sgr A*.*

m_K denotes the K-band magnitude, m_{S2} is 14.15 mag. In principle, the flux-ratio can be replaced with the ratio extracted from the counts. The results can be found in Table 5.3. The derived K-band flux denotes the magnitude values that are presented in the same table. The flux and the magnitude of the Dusty S-cluster Object stays rather constant over the years within the errors bars (see Fig. 5.7 and 5.8). The average value is 18.57 ± 0.11 mag. This average value is consistent with the derived K_S magnitude presented in Eckart *et al.* (2013). The authors use another near infrared instrument called NACO. The average K-band flux for the DSO is 0.0231 ± 0.02 mJy. A brightening in the epochs before and after the peri-center passage based on the observations cannot be observed. That is consistent with the predictions of, for example, Eckart *et al.* (2013) and Valencia-S. *et al.* (2015). It is important to note that neither an increase nor a decrease of the flux and magnitude as reported by Pfuhl *et al.* (2015) or Plewa *et al.* (2017) can be confirmed. As mentioned before, the bumpy background, the surrounding stars, and the unstable weather conditions make the analysis of the data challenging. A sensitive application of the given methods is crucial. Regarding the error-bars in Fig. 5.7 and 5.8, a natural variation can be observed. The discussed external influences are reflected in these fluctuations.
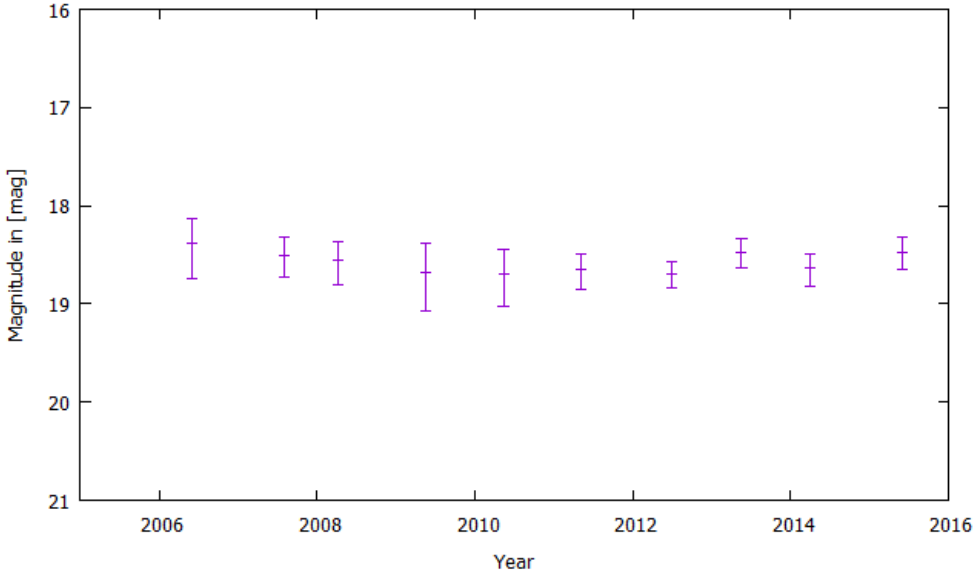
Figure 5.8: *The magnitude plot shows the almost-constant behavior of the DSO.*

Date (YYYY)	Magnitude (mag)	Flux (mJy)
2006	18.39	0.272
2007	18.50	0.247
2008	18.56	0.234
2009	18.68	0.209
2010	18.69	0.207
2011	18.65	0.215
2012	18.70	0.206
2013	18.48	0.252
2014a	18.64	0.216
2015	18.47	0.253

Table 5.3: *The observed K-band continuum flux of the dusty S-cluster object between 2006-2015. Of course, the presented K-band magnitude of the DSO shows the same constant behavior as the flux.*

Brγ line evolution between 2006 and 2015

The evolution between 2006 and 2015 of the Brγ line is presented in Fig. 5.9 and also shows the red-shifted HeI line in 2008 to early 2014. For a better comparison and overview, the wavelength range is fixed. The velocity is calculated with

$$\lambda_{observed} - \lambda_{rest} = \lambda_1 \tag{5.5}$$

and

$$\frac{\lambda_1}{\lambda_{rest}} \cdot v_{light} = v \tag{5.6}$$

where $\lambda_{observed}$ denotes the observed wavelength, λ_{rest} the rest wavelength of the observed lines that is shown in Table 2.1, and v_{light} the speed of light (300000 km/s). However, the red and blue-shifted HeI line is not present in 2006, 2007, 2014b (post pericenter passage), and 2015, because of the chosen wavelength window. The Brγ line, on the other hand, is clearly traceable (see the right plot) in the red-shifted domain (2.173 μm − 2.186 μm) with respect to the rest wavelength at 2.1661 μm (represented with a dashed line). Between 2006 and 2014, the red-shifted emission line gets accelerated with $v_{2006} = 1108.03$ km/s and $v_{2014a} = 2583.67$ km/s. After mid-2014, the blue-shifted Brγ line is detected in the wavelength domain between 2.142 μm − 2.151 μm. In late 2014, the Brγ emission line can be traced in the blue-shifted wavelength regime with a velocity of $v_{2014b} = 3198.60$ km/s for the DSO. This is much higher than the detected velocity earlier that year and also shows, that the DSO has passed the pericenter passage due to the blue-shifted nature of the line. As a consequence, the DSO is again detected as a blue-shifted Brγ line in 2015 with a velocity of $v_{2015} = 2230.5$ km/s. Therefore, the source is slowing down and reached the maximum of the line of sight velocity in 2014.

Since the width is not increasing significantly in the observed period of time, the proposed stretching by Gillessen *et al.* (2012) cannot be confirmed since this should be reflected in a broadening of the emission lines. Although the evolution of the Brγ line shows small variations in width and intensity, this can be traced back to the numerous external formerly discussed sources of interference. The resulting impact is additionally reflected in the noise behavior. The considered and later discussed nature of the DSO, a possible young accreting star (see Kurosawa and Romanova 2013), could contribute to these line variabilities. This low variability is consistent with the magnitude values discussed before and reflects, on top of the mentioned influences, the probably non constant accretion rate of a young stellar object. Analyzing the Brγ and HeI line show a HeI/Brγ ratio of ∼ 0.6. This indicates an optically thin emission material that is consistent with the findings of Gillessen (2014).

Orbit of the DSO

With the approach of searching for flares from Sgr A* in combination with the polynomial fit method (see Gillessen *et al.* 2009 and this chapter), the derived position and the velocity
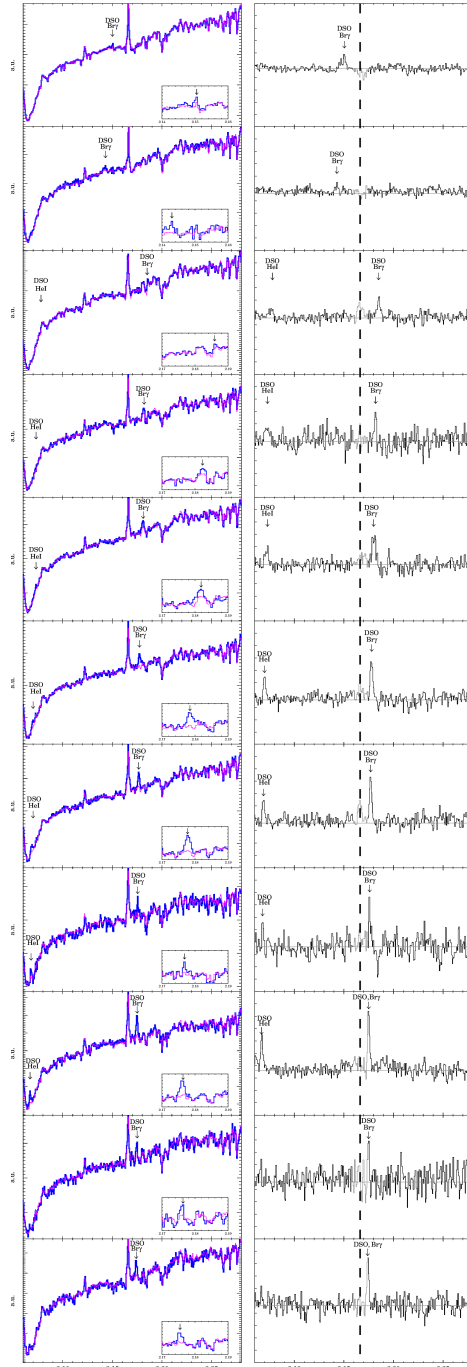
Figure 5.9: *Line evolution of the DSO. The vertical dashed black line in the right plot shows the position of the Brγ rest wavelength at 2.1661 μm. From the bottom to the top, the years between 2006 to 2015 are presented. In 2014, two spectra are presented since the DSO passed Sgr A*. The red-shifted Brγ peak in 2014b disappeared. Instead, one finds a blue-shifted Brγ emission in 2014b and 2015.*

of the DSO is used to create an orbit. The velocity shown in the plot of the orbit is purely based on the analysis of the Doppler-shifted Brγ line. The in Fig. 5.10 presented high
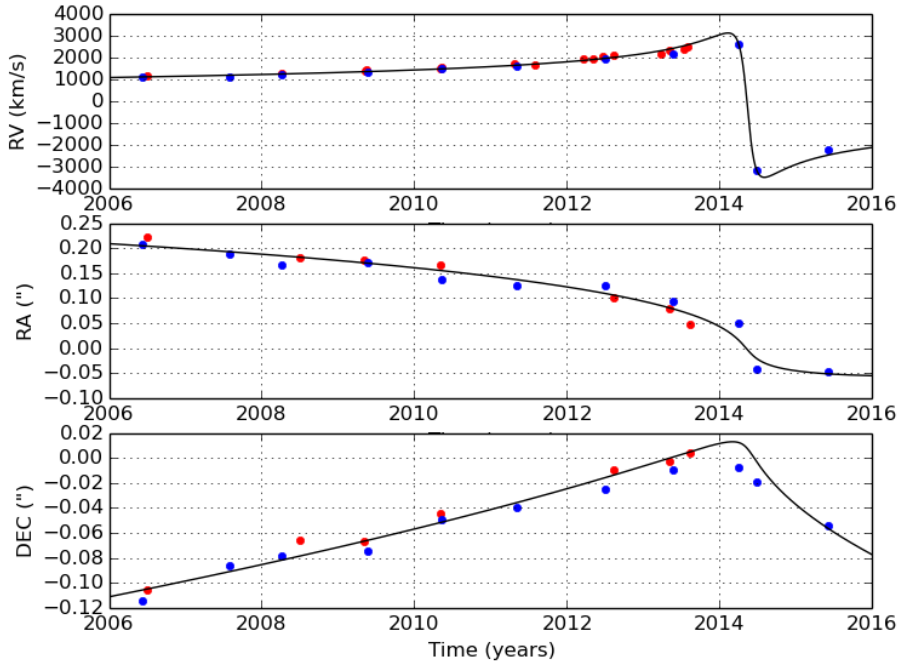
Figure 5.10: *The upper panel shows the line of sight velocity of the DSO that is based on the Doppler-shifted Brγ emission line. The middle and lower panel show the right ascension (RA) and declination (Dec) of the DSO. Based on this data, the DSO passed Sgr A* in 2014.39 with a projected Brγ velocity of over 3000 km/s. This plot is created by Marzieh Parsa (ph1, Cologne).*

precision orbit shows, that the DSO stays on a Keplerian orbit around Sgr A*. The red points are extracted from Meyer *et al.* (2014) and show an additional confirmation of the used methods and detections with an independent telescope (W.M. Keck I and II, see Peter L. Wizinowich 2000) till 2013. The plot of the orbit shows a rather constant Brγ line of sight velocity since its first observation in 2006 and 2010. Because of the close peri-center approach, a strong increase up to ∼ 2500 km/s can be observed. The maximum red-shifted velocity of ∼ 3000 km/s, unfortunately, is not observed. This is because the Galactic center cannot be observed during winter due to its declination. The single right ascension and declination plots are transferred to a 2D orbit of the DSO on the sky that is displayed in Fig. 5.11. This trajectory can now be applied to the LR images shown in Fig. 5.5. The resulting combination of these two results shows a remarkable position consistency (see Fig. 5.12). Since the orbit is based on the position of Sgr A* that is derived from single cubes and
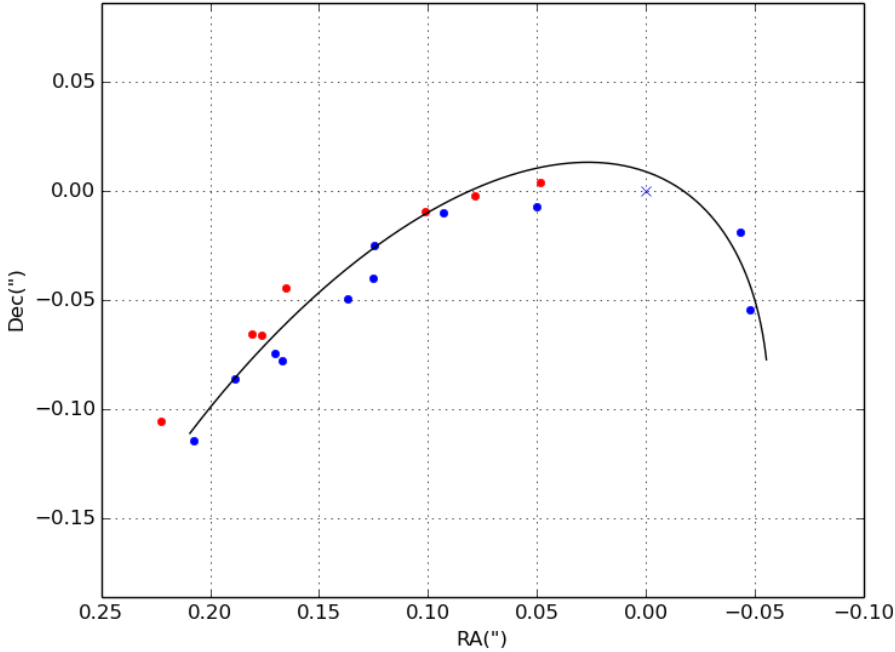
Figure 5.11: *Projected orbit of the DSO on the sky. The red points are extracted from Meyer et al. (2014). The SINFONI data from this work (blue dots) show a high consistency with the additional presented data. Sgr A* is centered at* RA = 0".0 *and* Dec = 0".0. *This plot is created by Marzieh Parsa (ph1, Cologne).*

polynomial-fits for several S-cluster stars, it is an independent and non entangled result. Figure 5.12 shows, that the DSO is moving on a Keplerian orbit around Sgr A* between 2006 and 2015.

Position-velocity diagram

By using the positions from the orbit shown in Fig. 5.10, position-velocity diagrams can be created. For that, continuum subtracted data cubes are used. With a SINFONI PSF sized distance above and below the orbit of the DSO, background slits for local background subtraction are created. Since the velocity and the distance to Sgr A* is well known, a position-velocity diagram can be shown (Fig. 5.13). This plot of the Brγ velocity of the DSO against the distance to Sgr A* shows a compact[2], Doppler-shifted emission source. It is another example of the non stretched nature of the DSO. This detection is consistent with

---

[2]Compact in this sense that the detected area of the Brγ emission line is $\leqq$ the beam size of UT4 ($\approx$ 5px, i.e., 62.5mas in diameter).
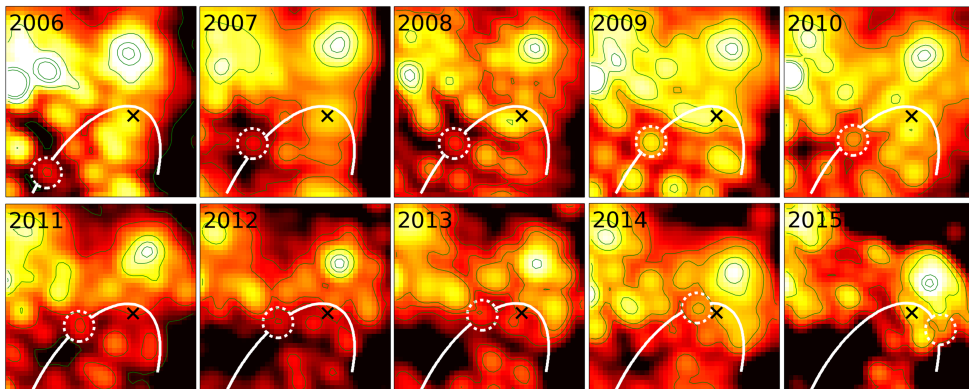
Figure 5.12: *Orbit of the DSO (dashed circle) in combination with the Lucy-Richardson images. The DSO can clearly be traced on the derived orbit. Sgr A* is marked with a black cross. The field of view of each panel is set to* $1".0 \times 1".0$.

the previous results. The pericenter passage is in 2014.39 and the DSO is clearly detected in 2014.2 (here: 2014a) before the periapse and in 2015 after the periapse. The spatial compactness is suffering from small variations that are well inside the PSF beam size of the instrument. Some diagrams show some features at the border, that can be associated with hot pixels and noise.

Mimicking the G2 tail emission

The discussed methods and tools are now applied to the data with the wrong ansatz. Instead of placing a PSF sized slit along the orbit, a 10-pixel wide slit (almost two times the size of the SINFONI beam size) roughly along the orbit is used that covers almost $\frac{1}{6}$ of the data cube. With this, the additional emission is included in the position-velocity diagrams that physically does not belong to the DSO in the first place. In Fig. 5.14, the results of the two approaches are presented. The right plot shows two additional sources which are above the noise level and almost as extended as the DSO itself. At least one of the two features is indicated in the initial pv diagram (left plot). A closer look at this emission reveals that other sources (or: other stars) are following the DSO on similar orbits (section 5.1). Compared to the left plot in Fig. 2.10, the similarities can not be neglected.

5.1 Detection of additional sources

The extended analysis of the SINFONI data reveals unexpected emission sources that are, like the DSO, detected in the Doppler-shifted Brγ wavelength regime. One source, X8 (Peißker et al., in prep.) is discussed in the outlook section. Another source can be directly linked to the detection of the DSO. It adds an accessible explanation of the diverse discussed topic and shows the risk of false interpretation of the data. Hence, the detection
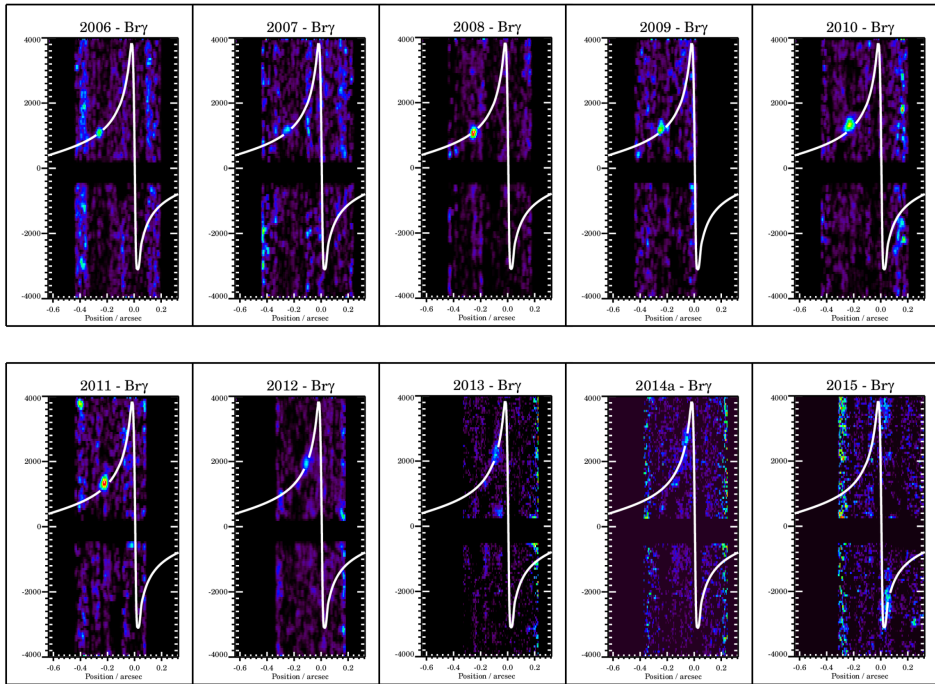
Figure 5.13: *The position-velocity diagrams are showing the DSO on its orbit around Sgr A* for every year between 2006 and 2015. The DSO can clearly be identified on the extracted orbit. No stretching can be detected. Different S/N ratios for the different data cubes cause some of the additional emission at the border of the single diagrams. Until 2014, the DSO is moving towards Sgr A* (positive velocity). After 2014, the DSO is moving away from Sgr A*. This results in a negative velocity. In 2014, the pv diagram shows no parallel detection of a blue-shifted Brγ counterpart upstream the orbit.*

of several dusty objects that are moving around Sgr A* can be reported. These objects are, similar to the DSO, detected in the red-shifted Brγ and Paα line domain. They are moving with a slightly increasing velocities between ≈ 750 km/s in 2008 and ≈ 1200 km/s in 2015 on orbits towards Sgr A*. The expected pericenter passage for the first object is around 2019. For the second object, the pericenter passage is determined around 2020. For the third object, the periapse is expected in the late 2020s. The orbits of these objects, that are named OS (Other Star), are separated from the DSO orbit by 2−5 px (25.0−62.5 mas) in the years between 2008 and 2015. The name is chosen to indicate a stellar nature in contrast to the reported "tail" emission by Gillessen *et al.* (2012), Gillessen *et al.* (2013), Pfuhl *et al.* (2015), and Plewa *et al.* (2017). Considering the low spatial separation and the position of these sources, the position is consistent with the tail feature of the DSO presented in the mentioned publications. Since the FOV is too small, the number of available data-sets are
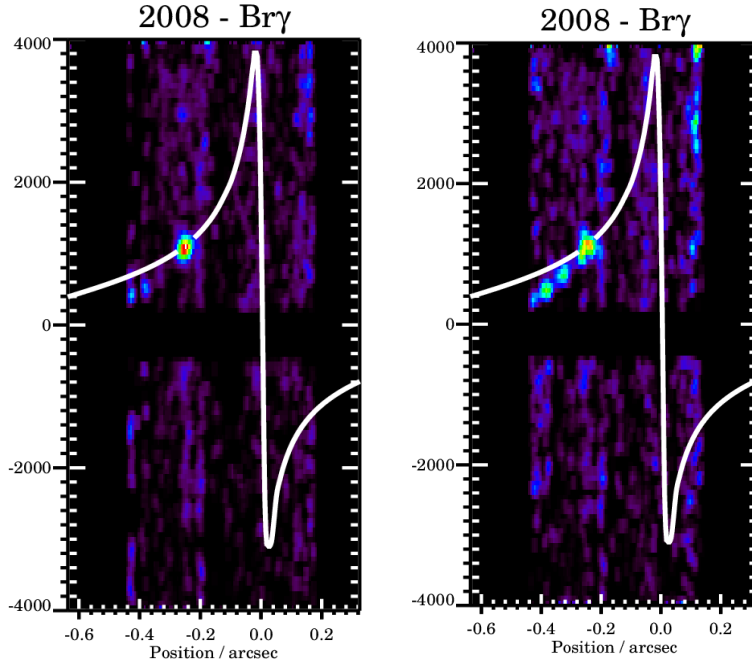
Figure 5.14: *The left figure shows the DSO in its orbit towards Sgr A*. The slit size is one PSF (6 pixels = 75 mas). The right figure shows the same plot but with a two sized PSF slit size. With this slit size, the additional emission is included. This could be interpreted as the claimed tail from* Gillessen et al. *(2012).*

limited. On top of that, the low quality of some data makes the identification of the sources not possible. This is also the result of the focus of the observations. Compared to the line maps of the DSO, the overall noise is stronger since the S/N ratio is decreased. A detection in other years increases the level of confusion even though the spectral analysis is less affected. However, the detected red-shifted Brγ source is shown in Fig. 5.15. The Keplerian orbit for OS1 is presented in Fig. 5.16. The object mimics the orbit of the DSO around Sgr A*. It is expected to be traced in the blue-shifted wavelength domain in late 2019. Since the Galactic center can only be observed between spring and late autumn, the earliest OS1 observations could take place in 2020.2 to verify this prediction. Regarding the nature of this object, it shows stellar characteristics. If a gas cloud scenario is considered, a certain degree of stretching is anticipated due to the gravitational influence of Sgr A*. Like for the DSO, no stretching, which would point towards a non stellar nature, is present. Also, a Keplerian orbit, in general, is associated with stellar objects. Because of the separation of the first and last data point covering the velocity and position of almost seven years, the confusion with a blend star (see Sabha *et al.* 2012) is highly unlikely. The results are underlined by the detection of OS1 in the Lucy Richardson reconvolved images that are presented in Fig. 5.18 and 5.19. The contours, that are shown in Fig. 5.15, indicate the continuum po-
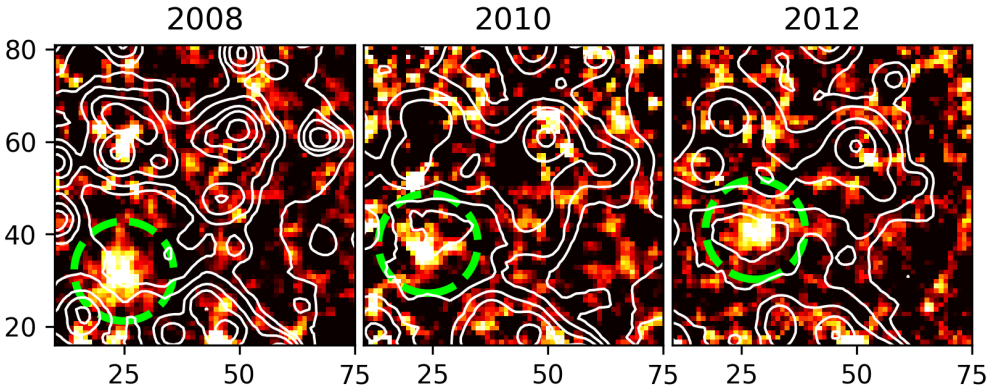
Figure 5.15: *These 3 line maps show the OS1 source on its way around Sgr A*. The contours are taken from the K-band continuum of the data cubes. OS1 can be detected at* 2.1715 µm *in 2008 and* 2.175 µm *in 2012. This plot is created by Marzieh Parsa (ph1, Cologne).*
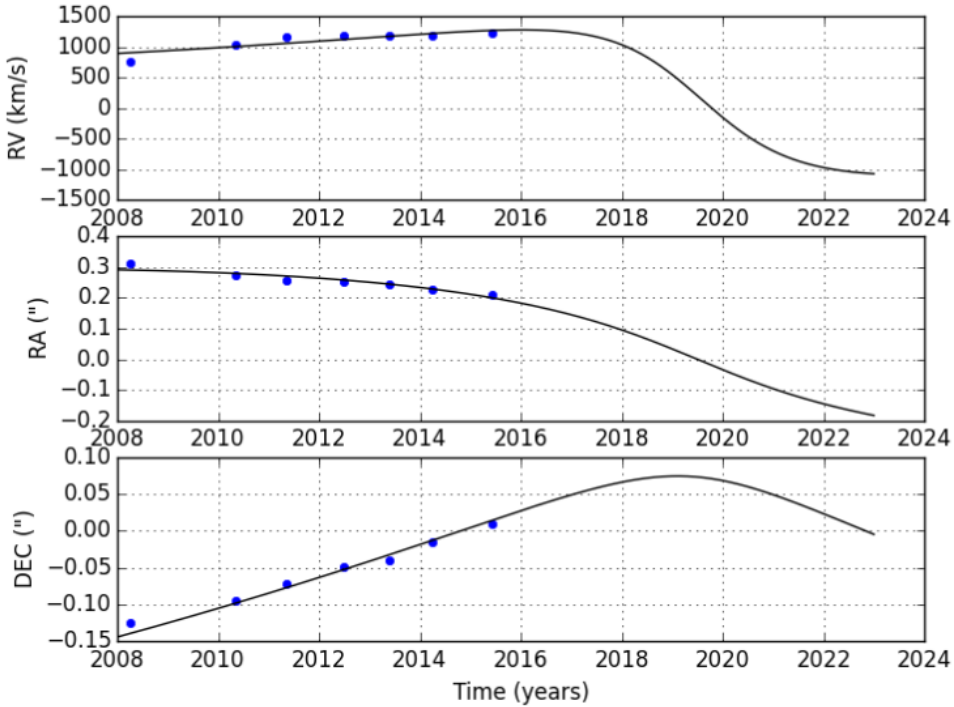

Figure 5.16: *The plot shows an increasing velocity for the OS1 source between 2008 and 2015. The periapse is determined for 2019. It is not clear if this fly-by can result in increased activity of Sgr A*. Compared to the DSO, the velocity will not increase significantly and stays below* 1500 *km/s.*
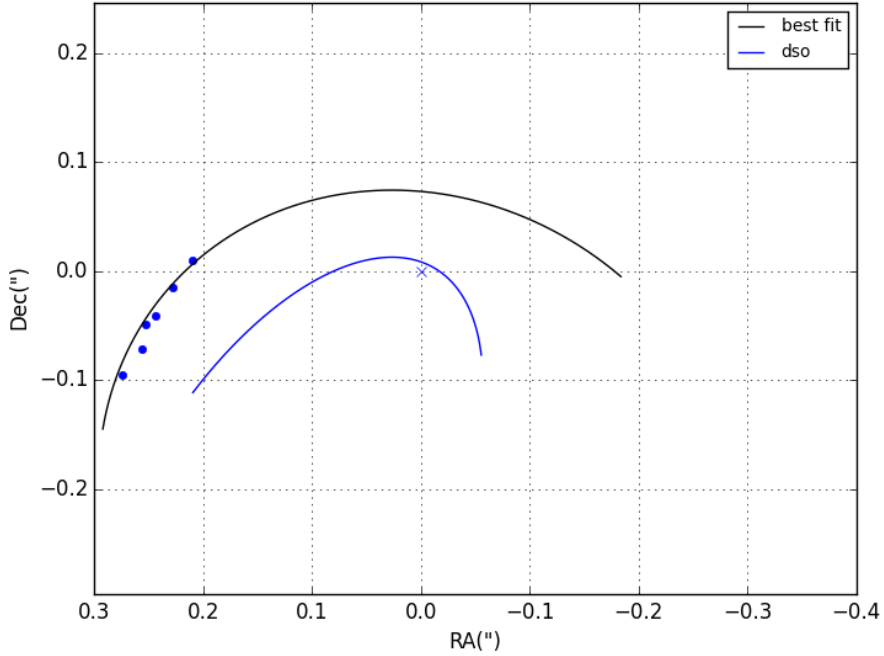
Figure 5.17: *A comparison of the OS1 and DSO orbit. The spatial separation is less than 0".1 and therefore around 8 pixels. The distance to Sgr A* around the periapse is ~ 0".08. Sgr A* is at the position of the blue cross, the DSO orbit is plotted in blue.*

sition of OS1 in the S-cluster. For a better overview, OS1 is marked with a white arrow in the low-pass filtered K-band images in Fig. 5.18. The white dashed circle highlights the DSO and shows the close, spatial distance between these two sources. In 2014, an identification becomes more challenging since OS1 is moving into a more crowded environment. As indicated by the name OS1, there are also other sources in the field of view. Keeping Fig. 5.14 in mind, the second source, OS2, is more challenging to identify. Even though it can be detected in the line maps, an isolated survey is more complicated compared to OS1 and the DSO because of the signal intensity and the S/N ratio. This is caused by the decreasing data quality at the borders of the stacked data-cube due to the focus of the observations. It cannot be ruled out that both sources merge and become "one" source or act as a blend star. The level of confusion is comparably high when it comes to OS2. Figure 5.20 shows the OS2 position and orbit on the sky compared to the DSO trajectory. Because of the diffuse emission and the low S/N ratio at the position of the source, the positions are not as accurate as for the DSO. This is also reflected in the fit in Fig. 5.21. Nevertheless, it is also possible to fit a Keplerian orbit to the data points that point towards a stellar nature of the object. The resulting problems of the low-quality data are also valid for OS3 which
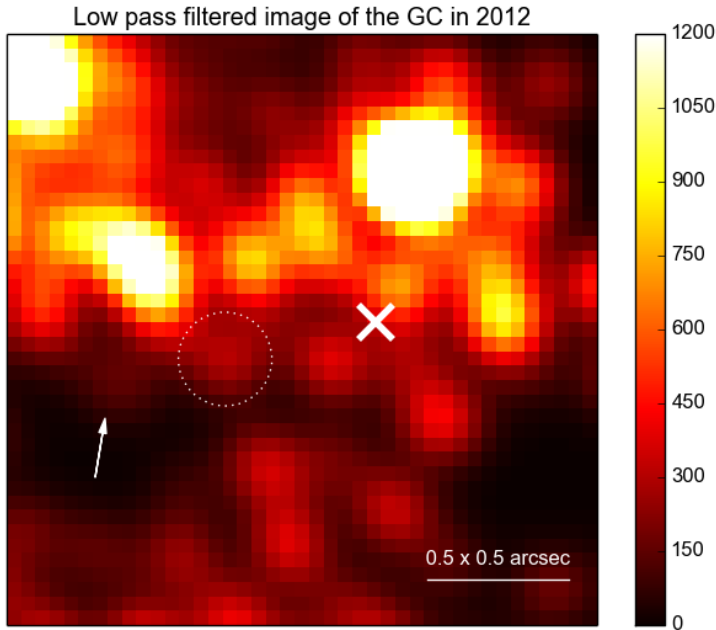
Figure 5.18: *The Galactic center plot in 2012 shows not only the DSO (white dashed circle) but also the OS1. This LR result is based on an extracted K-band image. Sgr A* is at the position of the white cross. The field of view is* 0".5 × 0".5. *The brightest source in the FOV is the star S2 that can be found just above Sgr A*.*

is spatially more separated from the DSO, OS1, and OS2. Since the data points are more separated, an orbit that is based on a Keplerian model can be presented (see Fig. 5.22 and 5.23). The data for OS3 shows a red-shifted infrared excess source that is moving on a Keplerian orbit around Sgr A*. The plotted data is limited to the time frame between 2012 and 2028. Because of the mentioned quality and observational limitations, earlier data sets provide unsatisfying position information. The plots for OS3 show a pericenter passage around 2022. However, these additional sources show the challenges during the analysis of the DSO and the confusion that emerges from the crowded field of view. Interestingly, Fig. 5.24 shows the combined orbits of OS1 (red data points), OS2 (green data points), and the DSO (blue orbit). Since the orbit starts in 2007, the shown plot explains the tail emission. It can be concluded that additional data sets are needed from independent instruments and telescopes that could expand the analysis of these sources.
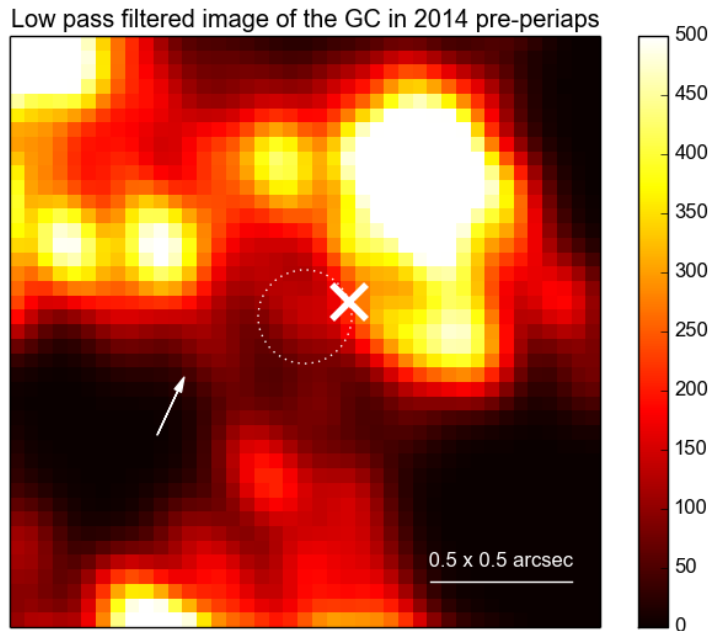
Figure 5.19: *The Galactic center in 2014 with the same properties as described in Figure 5.18. Here, the detection of the OS1 source is more complicated because of the overlapping wings of the PSF of the stars close to Sgr A*.*

5.2 Velocity gradient of the DSO

Taking a closer look at the discussed sky variability reveals interesting details above the analysis process. For that, the sky data needs to be manipulated. This can be achieved by using the single sky frames, that are subtracted from the object-cube (science+sky). It is

$$object - sky = science .\qquad(5.7)$$

The sky frames are a direct output from the SINFONI pipeline. They can be treated as data-cubes because of the comparable structure. This is important since several correction routines have to be applied to them. The first step is to apply the flagging correction to identify bad and hot pixels as well as cosmic rays. Then, the single sky cubes are shifted to a certain position which is consistent with the object-cube counterpart. For that, the same shifting vector as for the object cubes is applied to the sky cubes. The sky cubes are now placed in a 100 × 100 pixel array and normalized to a median value of a 1-pixel aperture that is placed close to the DSO position in the single cubes. In the final step, the single arrays are added up and show a sky cube with the same size of the field of view as the final
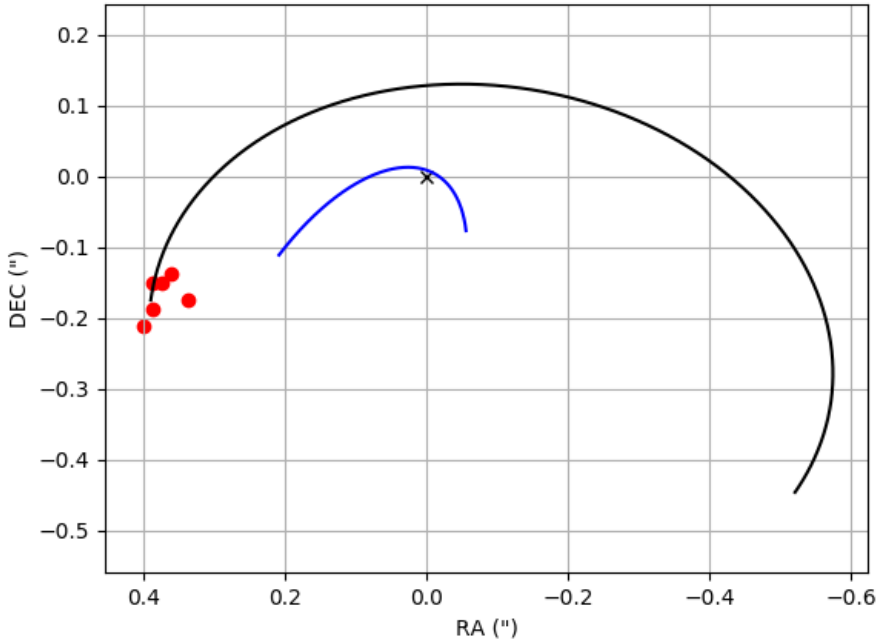
Figure 5.20: *Compared to OS1, the presented OS2 orbit shows a higher spatial separation than the DSO orbit. The OS2 data points (red) are more scattered than the OS1 data points that can be explained by the diffuse emission. Therefore, the derived center of gravity is hard to determine. The DSO orbit is plotted in blue, the position of Sgr A* is centered at the blue cross at* $\mathrm{RA} = 0".0$ *and* $\mathrm{DEC} = 0".0$.*

science data cube. By comparing the single sky spectra, it can be found that the variability of the lines is in a range of 5% − 20%. Using this small percentage and applying it to the final sky data cube, sky variability can be imitated. Figure 5.25 shows the velocity gradient which is extracted from the non manipulated final data cubes. For that, every single pixel of the related spectrum in the Brγ wavelength domain is analyzed. If the emitting line of a single pixel at the position of the DSO is over a 3σ threshold, the pixel itself is displayed. Therefore, Fig. 5.25 shows not only the velocity gradient but also a good indicator for the noisy background emission. In 2007 for example, the emitting line is too close to the noise level. Hence, no pixel is included in the analysis. It also shows that the emitting area of the Doppler-shifted Brγ line is limited. As it turns out, the size of the DSO is always below the limiting PSF size of SINFONI. With this information, it can again be confirmed that the object is compact and non extended. However, the range of the color bar just next to the plots is based on the values extracted from Plewa *et al.* (2017). The authors of this publication claim that a velocity gradient in the given range can be detected, i.e.,
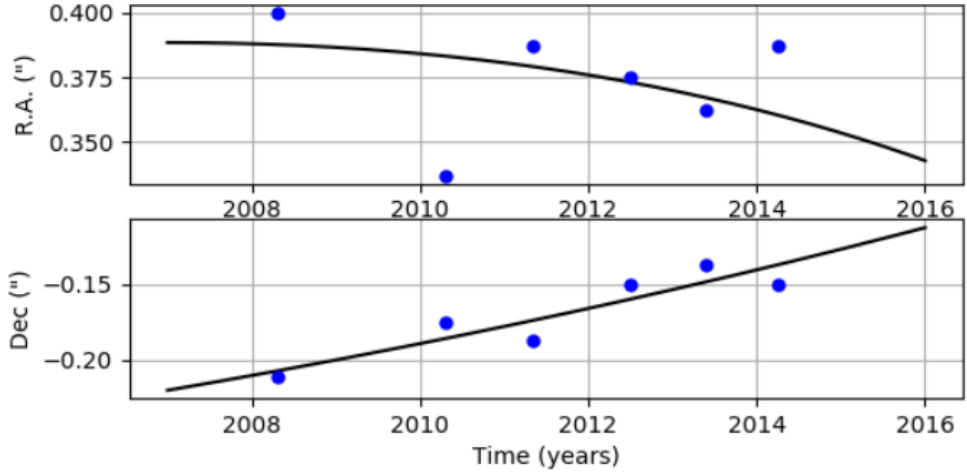
Figure 5.21: *The orbit parameters of the OS2 source show in the right ascension (RA) a higher uncertainty than the declination (DEC). The low S/N ratio can be accounted for this result. The pericenter passage is determined in the late 2020s. Because of the shifted field of view and the low data quality at the border of the cube, the position of OS2 cannot be determined before 2008 and in 2015.*

the back of the DSO is slower than the front that is closer to Sgr A*. It is implied that the gravitational force of the black hole stretches the object. With this, Gillessen *et al.* (2012), Pfuhl *et al.* (2015), and Plewa *et al.* (2017) conclude that the object must be a gas cloud. In contrast to these publications, the analysis presented in this work draws a clear picture. For every year between 2006 and 2015, the resulting velocity maps do not show a gradient that would reflect a gaseous nature of the DSO. Furthermore, a detailed analysis can be found in Table 5.4. The values of the first two rows are extracted from the orbit. The maximal velocity range indicates the possible velocities which the DSO reaches between the 1st of January and the 31st of December in every year. Given that the observations just cover a certain time span during a year, maximal observation velocity range specifies the possible values that could be detected. This range is important since it is based on a model of a star that is moving around a black hole on a Keplerian orbit. If a detected velocity gradient would be higher than this range, this would indicate a non stellar nature of the DSO. This value is followed by the velocity range per PSF. Because of the compact size of the DSO, the following row compares the velocity range per PSF and the velocity range per emission area. The difference is that the size of the DSO is smaller than a PSF. This again is an important comparison. If the velocity range per emission area is higher than the range per PSF, this would indicate a non stellar nature of the DSO. As it turns out, this value is indeed smaller than the PSF velocity range for every year. The next-to-last row presents the minimal and maximum pixel value. Hence, this is the difference between the smallest and the biggest velocity value of the DSO. Why this value is higher in some years than the maximal observation velocity range can be a puzzling question. To explain this,
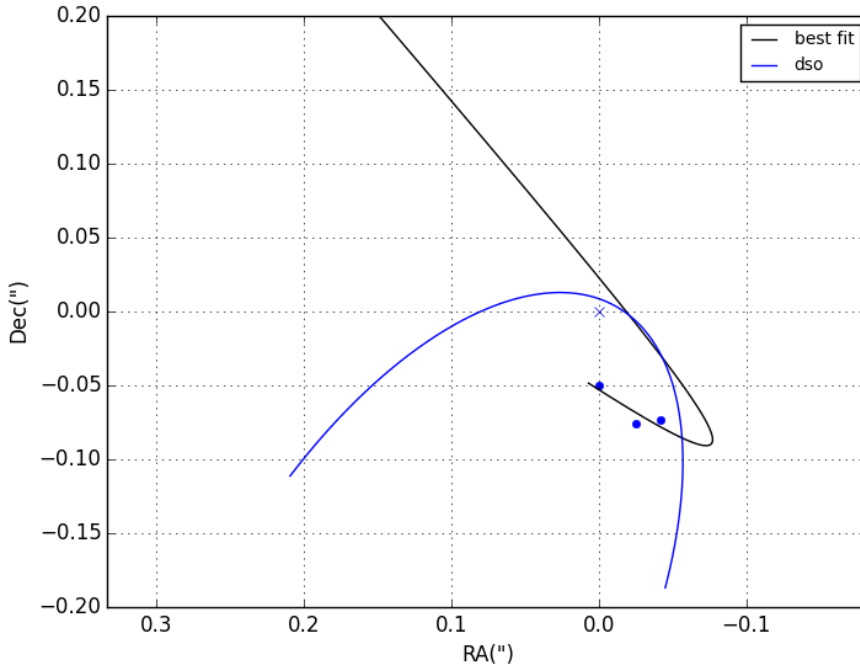
Figure 5.22: *Possible orbit of OS3 based on 3 data points since its detection in the crowded environment of Sgr A* is not possible in every year. The possibility of a blend star, i.e., two sources that move close to each other and combine their flux to create a false signal, can not be ruled out completely. OS3 crosses the orbit of the DSO in 2017. This should be taken into account if available data sets are investigated in the future. This plot is created by Marzieh Parsa (ph1, Cologne).*

a detailed analysis of single pixels is needed. Some pixels are located close to strong sky lines. Fitting a Gaussian to these pixels can result in a higher or lower velocity outside of the range. For that, the influence of the nearby sky lines has to be taken into account. Also, the background noise can lead to a centroid shift towards higher or lower values. Overall, it shows that the velocity gradient is a feature that is not as strong as indicated by Plewa *et al.* (2017). The last row gives the values of the mentioned publication. These results are much higher than the presented values of this work for every year. The key difference is, that the authors of Plewa *et al.* (2017) smooth their data, i.e. they apply a Gaussian to the data. Section 5.4 will investigate the influence of this approach.
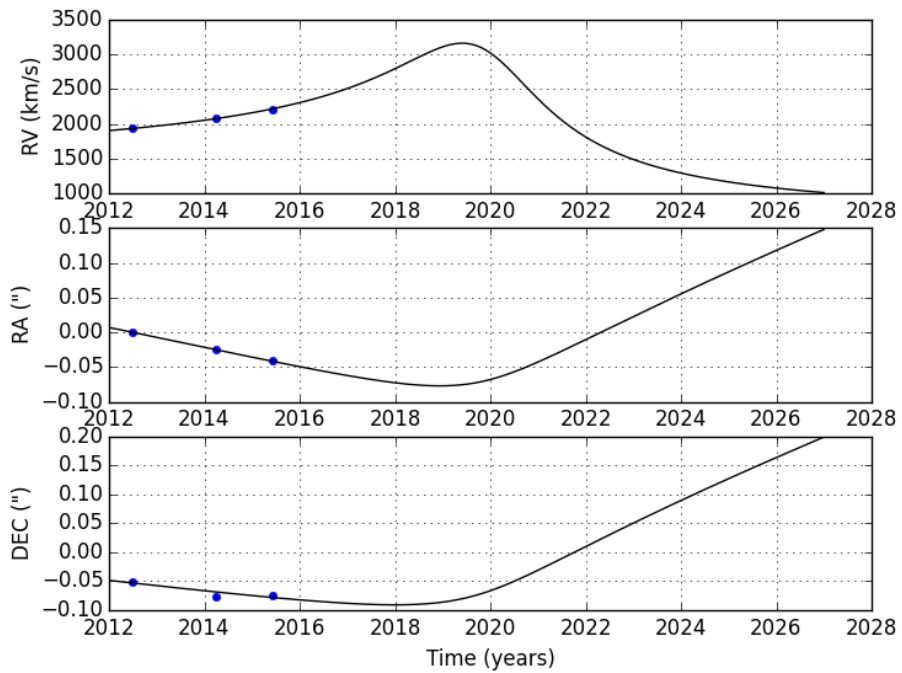
Figure 5.23: *Orbital parameters of OS3 showing a pericenter passage around 2021.5 when the velocity reaches over 3000 km/s. If OS3 is indeed not a blend star, it could increase the magnitude of the DSO in 2017 or in the following years since the spatial separation between the two objects is just a few pixels. The objects could overlap and trigger an increase of the flux. This plot is created by Marzieh Parsa (ph1, Cologne).*
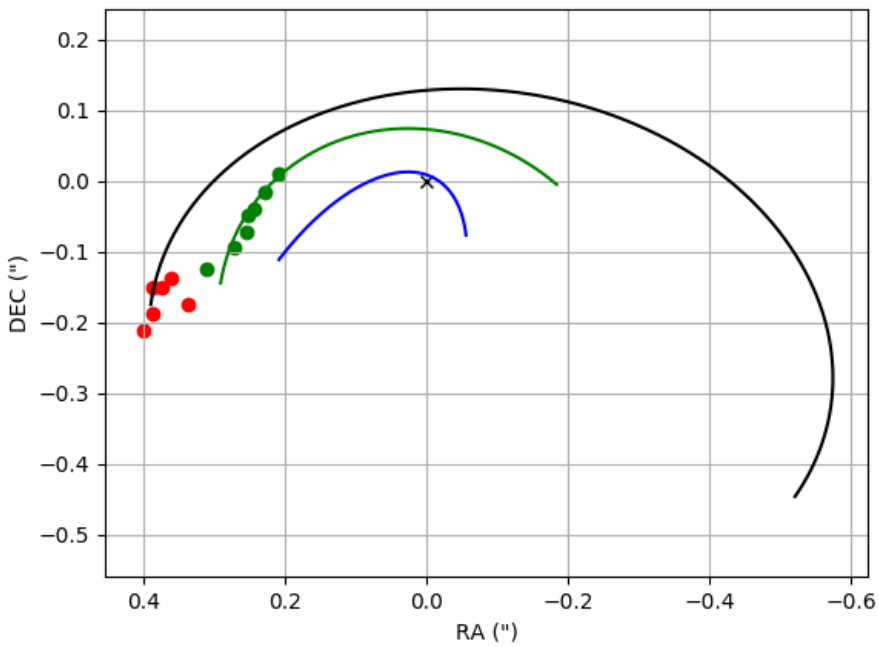
Figure 5.24: *Combined orbits of OS1 (green data points), OS2 (red data points), and the DSO (blue orbit). With this plot, the additional emission in Fig. 5.14 can be explained since the sources in the pv diagram are consistent with the sources OS1 and OS2.*
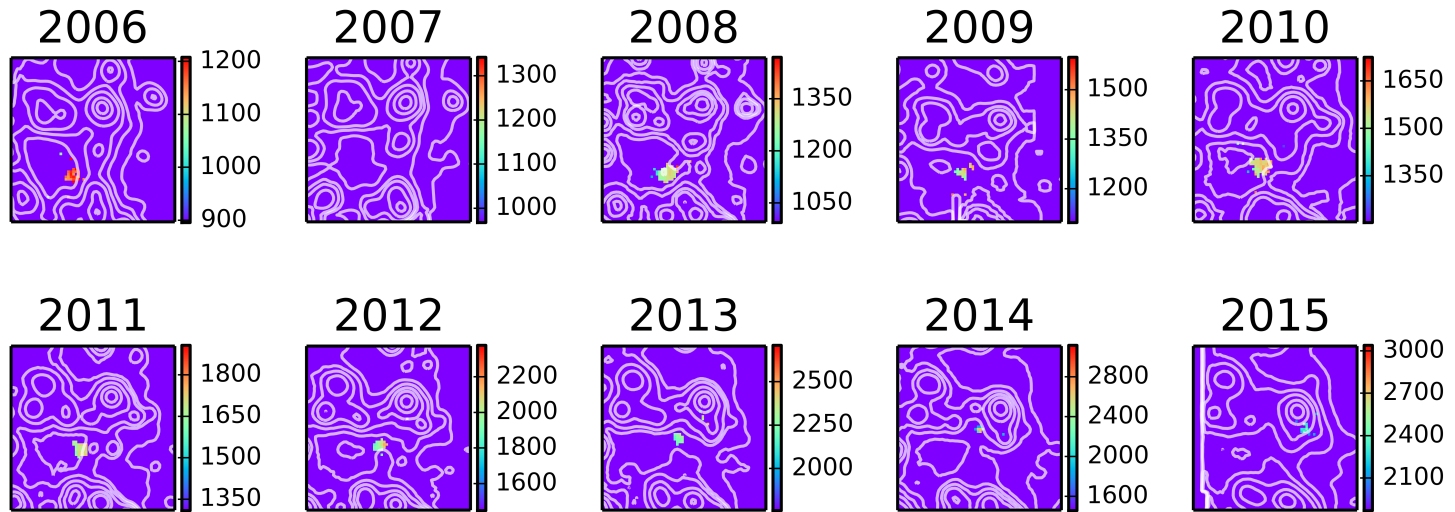
Figure 5.25: *Velocity gradients between 2006 and 2015. The plots are based on the final reduced and corrected data cubes. No error or smoothing kernel is applied. The color bar range is adopted from* Plewa et al. (2017) *and shows in almost every year the DSO emission. The emission of every displayed pixel needs to be above* 3σ*. With that, noise can be excluded in the final output. As a consequence, the size in every year is below the PSF size of SINFONI. This indicates a compact source. In 2007, the noise is too dominant which makes the fitting procedure fruitless.*

	2006	2007	2008	2009	2010	2011	2012	2013	2014 pre periapse	2015
Centroid velocity	1186.70	1302.47	1323.95	1454.89	1566.46	1728.18	2082.91	2318.26	2715.91	-2305.92
Maximal velocity range/year	62.83	74.62	91.16	115.79	157.54	230.45	404.83	1123.26	494.8	670.89
Maximal observation velocity range	26.17	31.09	-	-	26.25	67.21	202.41	561.63	103.08	279.53
Expected velocity range per PSF	7.63	8.74	-	-	10.60	30.94	120.18	748.84	51.96	200.91
Expected velocity range per emission area	6.31	8.74	-	-	4.55	12.69	52.25	315.30	24.94	80.36
This work, detected velocity range	73.49	(108.97)	39.94	73.73	64.02	117.75	127.54	231.87	126.86	227.34
Plewa *et al.* (2017), detected velocity range	98.73	-	101.26	-	171.73	246.15	217.39	294.73	432	280

Table 5.4: *Values, that are given in km/s, for the velocity gradients between 2006 and 2015. The centroid velocity is taken from the Keplerian fit (see Fig. 5.10) file. Additionally, the expected velocity is extracted in the same way and shows the velocity range from the beginning till the end of the year. Since the observational data does not cover the whole year, the velocity gradient is always slightly lower than the expected one. The data from Plewa et al. (2017) is based on the lookup table in their plots of the velocity gradient (see Fig. 4 in the mentioned publication).*

Epoch	Error in %	FWHM in $\left[\frac{km}{s}\right]$	Line peak in $\left[\frac{km}{s}\right]$	Luminosity $\left[10^{30}\frac{erg}{s}\right]$
2008.26	-	215.2	1302.4	5.047
	−10%	196.0	1300.2	4.973
	+10%	234.24	1304.9	5.148
	−20%	174.39	1298.5	4.851
	+20%	248.52	1307.2	5.163
2010.36	-	326.6	1565.4	8.424
	−10%	325.5	1566.2	8.448
	+10%	327.3	1564.5	8.390
	−20%	326.3	1566.2	8.543
	+20%	333.6	1564.2	8.538
2012.49	-	513.1	2029.8	6.079
	−10%	523.7	2032.2	6.106
	+10%	494.9	2025.6	5.987
	−20%	535.3	2035.9	6.139
	+20%	480.9	2023.0	5.985

Table 5.5: *Complete overview of the different sky errors and their influence to the luminosity, velocity, and the FWHM. Introducing an error shows a negligible influence (< 1%) to the luminosity, velocity, and the FWHM.*

5.3   Velocity gradient of OS1

Since the DSO can be analyzed for a velocity gradient, the same can be done for OS1. Even though the velocity is smaller than the DSO, it is interesting to know if OS1 also shows signs of a gradient. The challenge low S/N ratio compared to the DSO analysis. Therefore, some data-sets do not meet the required quality. Table 5.6 presents the results of the comparison between the gradient of the DSO and OS1. In this table, just the maximum gradient per year with the maximum gradient of the combined observations per year are compared. It

	2008	2010	2012
DSO - Centroid velocity	1323.95	1566.46	2082.91
OS1 - Centroid velocity	960.04	1063.21	1175.19
DSO - Expected gradient	±45.58	±78.77	±101.2
OS1 - Expected gradient	±24.19	±27.28	±27.98
DSO - This work	±19.97	±37.01	±63.77
OS1 - This work	±27.20	±11.59	±10.41

Table 5.6: *Comparison of the velocity gradient of OS1 and the DSO. The values are given in km/s.*

shows, that the detected gradient is always lower than the expected one. This indicates that the gradient is an observational and not a physical feature.

5.4   Smoothing the data

The influence of the manipulation of the data with the applied sky error and the smoothing is presented in Table 5.7. The impact on the luminosity is between $1\% - 10\%$. The centroid line peak variation is in the uncertainty range and negligible. This minor effect is also reflected in the velocity.

Epoch	Error in %	Smoothed	FWHM in $\left[\frac{km}{s}\right]$	Line peak in $\left[\frac{km}{s}\right]$	Luminosity $[10^{30}\frac{erg}{s}]$
2008.26	-	No	215.2	1302.4	5.047
	-10%	No	196.0	1300.2	4.973
	-	Yes (1px kernel)	214.9	1302.5	4.308
2010.36	-	No	326.6	1565.4	8.424
	-10%	No	325.5	1566.2	8.448
	-	Yes (1px kernel)	324.9	1563.6	8.048
2012.49	-	No	513.1	2029.8	6.079
	$+10\%$	No	494.9	2025.6	5.987
	-	Yes (1px kernel)	524.7	2035.5	5.992

Table 5.7: *This table shows a overview of the velocity gradient. The application of a smoothing kernel shows a negligible influence ($< 1\%$) on the luminosity, velocity, and the FWHM. As presented before, this is comparable to the influence of the sky error.*

The results presented in Table 5.7 show the robustness of the data under the influence of variations. Interestingly, the size of the DSO is enhanced due to the smoothing kernel. This is because the wings of the line are extended and blurred out. The Figures 5.26 - 5.28 show an increase of the DSO size between $10 - 20\%$ that also expands the range of the minimum and maximum velocity.

5.5 Creating the velocity gradient

The final comparison between the different manipulation setups in Table 5.8 draws a clear picture. Investigating the influence of an artificially created sky variability (see Table 5.5 and 5.7) results in a minor increase of the velocity range over the emission area of the DSO. However, the increase of the gradient by the sky variability is already between $75 - 120\%$. The values are shown in Table 5.8. Using a one-pixel kernel and smoothing the

	2008 in $\left[\frac{km}{s}\right]$	2010 in $\left[\frac{km}{s}\right]$	2012 in $\left[\frac{km}{s}\right]$
This work, no error	±19.97	±37.01	±63.77
This work, 10% error	±35.99	±88.27	±138.58
This work, smoothed, 1 px	±80.46	±143.94	±200.5
Plewa *et al.* (2017)	±238	±261	±464

Table 5.8: *Comparison between the velocity gradient after the introduction of an sky error with the one presented in* Plewa *et al. (2017).*

data with it, reveals a huge increase between $300\% - 400\%$ for the investigated data sets. As mentioned before, the red and blue wings of the emission lines are blurred out. Due to the strong background and noise emission, it is obvious that the spectral information is spread out because of the smoothing kernel. However, even with this dramatic increase of the values, the presented velocity gradient in Plewa *et al.* (2017) is far higher than the values presented in this work. This can be reached if the threshold of the emitting line is lowered. The authors of Plewa *et al.* (2017) mention in their analysis that the HeI is also taken into account. Since this line is weaker by a factor of $0.5 - 0.7$ compared to the Brγ line, it can be concluded that the confusion level is increased.
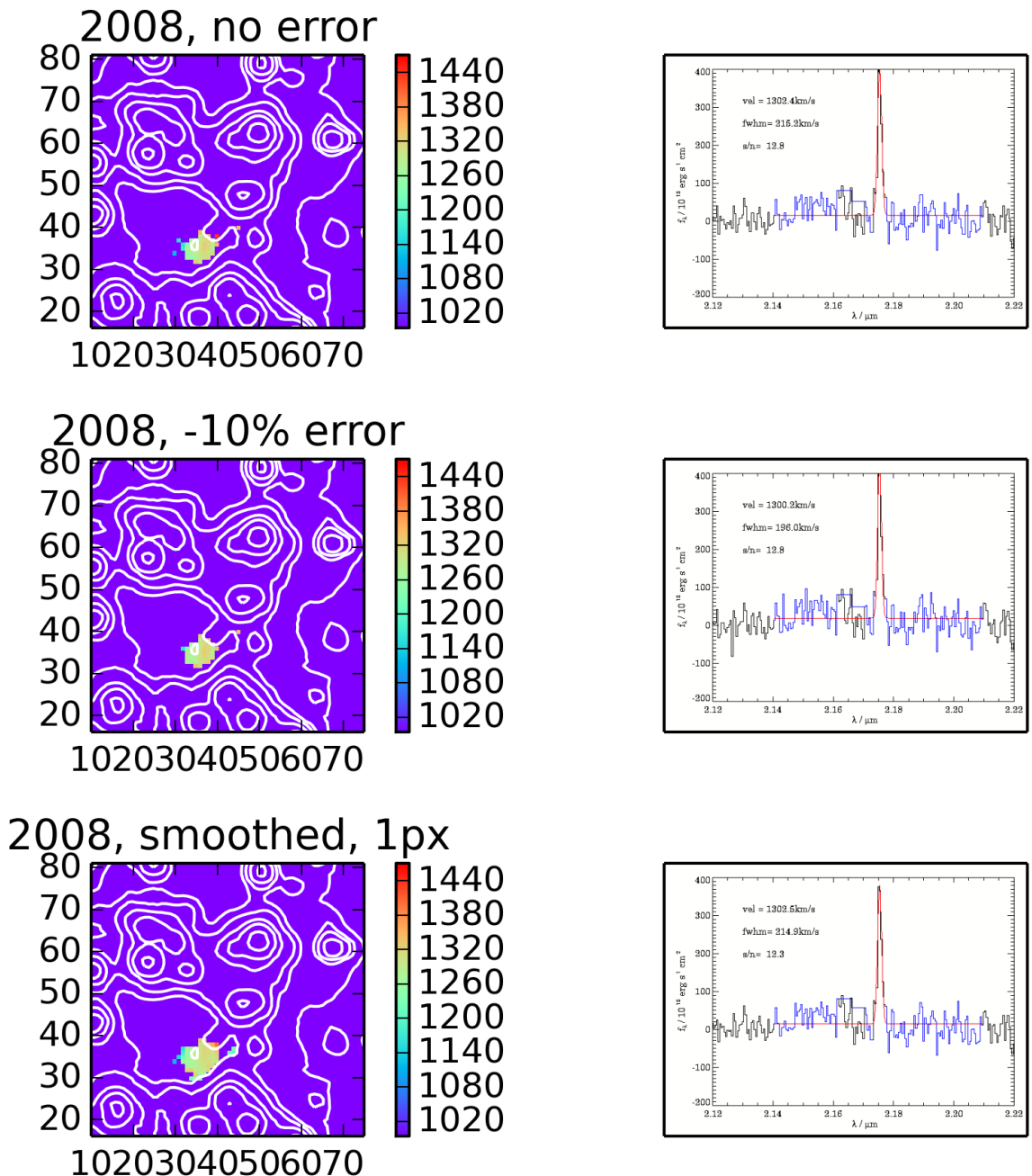
Figure 5.26: *These plots show the velocity gradient in 2008. The first plot is based on the final data cube. The velocity range is taken from the gradients in* Plewa *et al.* (2017). *As a result, no significant gradient can be observed. Next to it, the red-shifted Brγ emission line of the DSO is presented. It can be clearly detected above the noise. In the next row, a error is introduced to the data. The outcome does not show a significant influence of the enhanced sky variation. The emission area is approximately the same size as the data presented in the first row. The last column, on the other hand, show a significant increase in the emission area by over* 10%. *This is followed by an increase of* 400%.
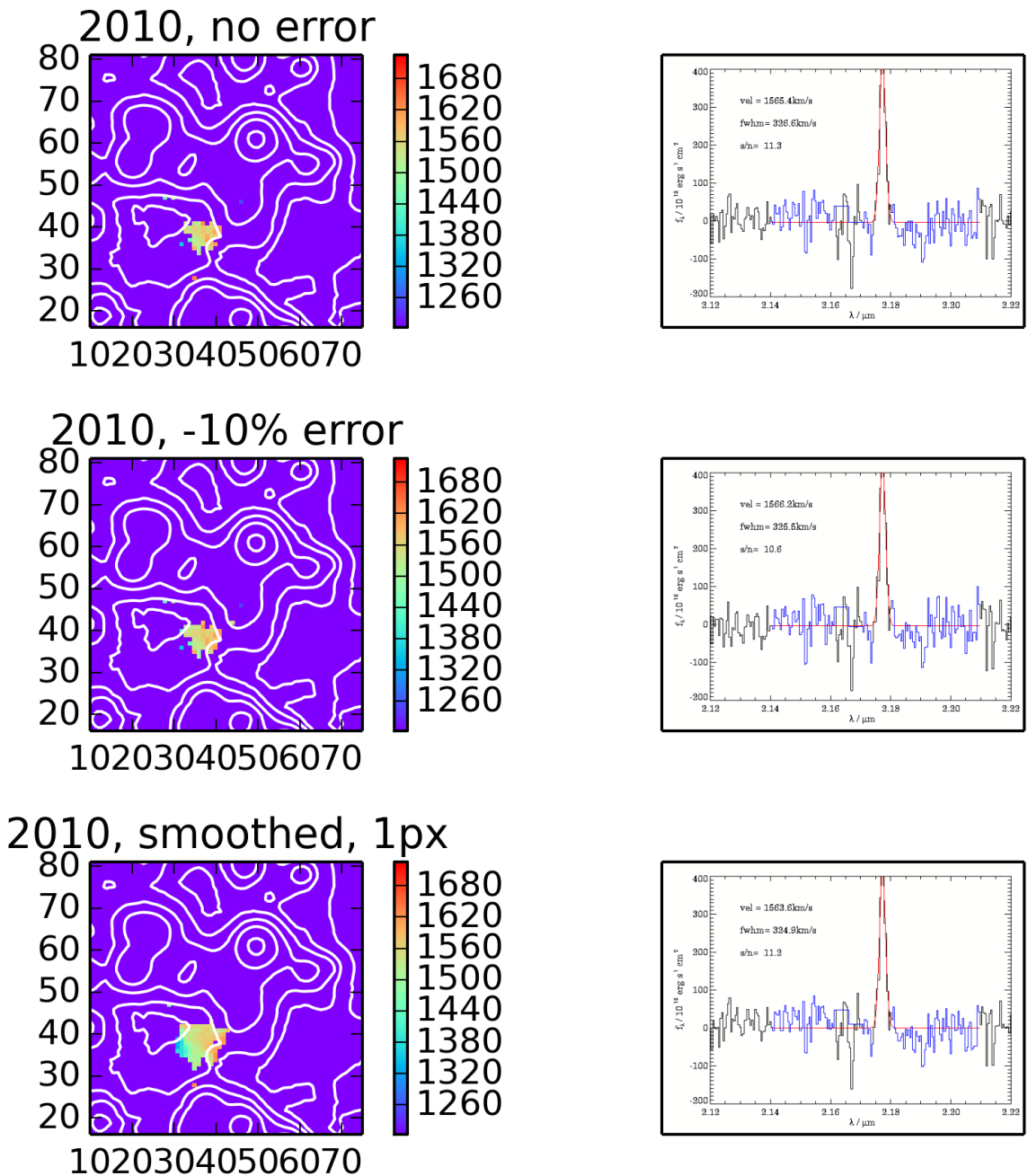
Figure 5.27: *The velocity gradient in 2010. Like in 2008, the size of the DSO is not affected by the sky variations that are simulated with the introduction of a artificial error. Smoothing the data with a 1-pixel kernel leads again to an increase of over 10%. The increase of the velocity gradient is over 300%.*
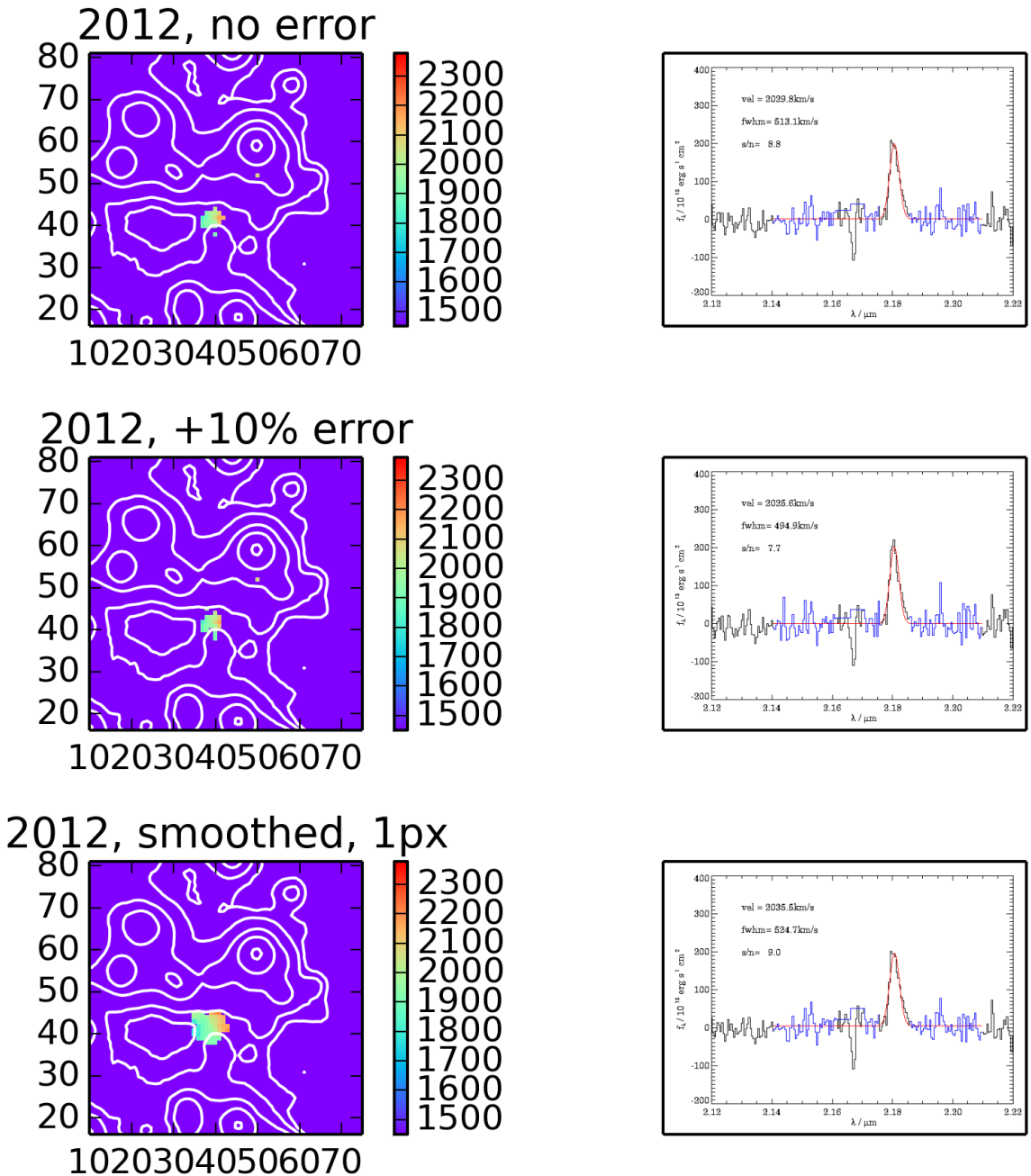
2012, no error

2012, +10% error

2012, smoothed, 1px

Figure 5.28: *In 2012, the increase of the 1-pixel smoothed data is again over 300% compared to the not smoothed data cubes. The size of the emission area of the DSO increases over 20% for the smoothed data.*

DISCUSSION

This chapter summarizes the results and findings of the DSO survey between 2006 and 2015.

6.1 Detection of the DSO

As a starting point of the analysis, Brγ line maps are used to identify the DSO in the SIN-FONI data cubes. The clear presence in the Doppler-shifted wavelength domain provides precise velocity and position information that is used to determine the distance to the derived Sgr A* position. The size of the DSO in the Brγ line maps is for every year comparable to the beam size of the SINFONI instrument. This indicates a compact nature of the object. Between 2006 till 2014.39, the data shows a red-shifted Brγ line in every year. Additionally, the HeI and Paα line can be detected with a matching velocity. However, the Paα line is highly contaminated with telluric emission lines. Therefore, it is too sensitive towards external influences, so it is excluded from the analysis. The HeI line is suffering from variations that result in a challenging detection. Therefore, the focus on the Brγ line is justified. Following this, the detection after 2014.39 in the red-shifted wavelength domain is unsatisfactory. This is because the DSO moved around Sgr A* (instead of being dissolved or destroyed). This is underlined by the presence and detection of the DSO in the blue-shifted Brγ domain. Staying on a Keplerian orbit, the non dissolving structure, and the fact that no increased activity of Sgr A* is observed points to a stellar nature of the DSO.

6.2   Properties of the DSO

As a follow-up analysis, the identification of the K-band Lucy Richardson reconvolved images on the derived orbit around the Sgr A* shows the DSO in every data set between 2006 and 2014. In 2015, the confusion of the DSO detection at the expected position cannot be ruled out entirely since a star, probably S62, is crossing its orbital path. Besides this limitation, the position of the DSO in the Lucy Richardson reconvolved images is consistent with the location that is derived from the Brγ line maps. It can be therefore concluded, that the identified source in the continuum images is indeed the source from the line maps. With that, aperture photometry can be applied since reference stars are in the field of view. By using S2 as a reference star, it can be shown that the DSO does not illuminate or gets dimmed. Both scenarios would speak against a stellar nature since a dimming would be explained by the dissolving structure of the DSO. The illumination could be connected to accretion events of Sgr A* or heating resulting from shocks of the ambient medium. Neither of this scenarios took place. In contrast to the proposed ideas about the faith of the DSO, the object shows a somewhat constant behavior when it comes to flux and magnitude. To put this into perspective, Eckart *et al.* (2013) as well as Shahzamanian *et al.* (2015) derive matching flux and magnitude values by using different sets of data from another instrument. Additionally, Witzel *et al.* (2014) present data from another telescope that underlines the constant flux and magnitude of the DSO.

6.3   Stretching of the K-band source

The analyzed and presented SINFONI data does not show signs of the proposed stretching that indicates a gaseous nature of the DSO. Judging by the line maps and the reconvolved K-band images of the Galactic center, the source stays compact and comparable in size as a function of the years. It is, of course, possible that some of the emitting material is suppressed or amplified because of the noise and background effects. The line map detection shows, on the other hand, a reasonable approximation of the orbiting object. This is followed by the presented position-velocity diagrams. They are also not showing signs of a stretched DSO. It seems, that the influence of the slit size, that adds up the flux along the orbit, is not neglectable. The presented example shows additional sources that are not on the orbit of the DSO. The similarity of the derived position-velocity diagram with the one presented in Gillessen *et al.* (2012) is remarkable and underlines false interpretation of the data.

6.4   Parallel detection of the red- and blue-shifted Brγ line

If there was a simultaneous Brγ emission in the red- and blue-shifted wavelength regime in 2014, it could result in a parallel detection in the position-velocity diagrams. This is because the slit is placed along the orbit and adds up all emitting wavelengths. Before 2014.39, no blue-shifted Brγ line can be found. However, as shown in the chapter 7, ran-

domly placed background apertures can create a blue-shifted Brγ signal in 2014.39. But it should be noted that the size of the aperture does not match the DSO aperture and therefore an over-subtraction takes place.

6.5 Additional sources

Investigating the claimed tail in 2008 reveals the surprising presence of additional sources (OS). OS1 and OS2 can be traced as single objects in several years following the DSO on a similar orbit with an increasing distance of 100 mas (2008) to 200 mas (2014). According to the data, the objects are following a Keplerian orbit around Sgr A* with a velocity of 1000 km/s in 2008 up to 1400 km/s in 2014 for OS1. OS2 is slightly slower with a determined velocity of around 660 km/s in 2008 and 750 km/s in 2014. The expected pericenter passage for both sources can be dated between 2020 and 2030. OS1 and OS2 will approach the black hole with a distance of less than 0.1 arcseconds. According to the redshifted Brγ line map emission, the size of OS1 is comparable with the beam size of SIN-FONI. That indicates, as well as for the DSO, a compact nature. Therefore, a dissolving structure, which would point to a gaseous nature can be ruled out. If the average magnitude of the DSO is around 18.5 mag, this can be used as an upper limit to determine the magnitude of OS1. According to the SINFONI manual, the limiting magnitude in the 0".8 × 0".8 plate scale in the H+K band is around 19.2 mag. Judging by the presented Lucy Richardson images, OS1 is fainter than the DSO. Therefore, the resulting magnitude of the object should be 18.9 ± 0.3 mag. OS2 is harder to identify because of the low quality data and the S/N ratio. Since it is even fainter than OS1, the upper limit for its magnitude can be determined to 19.2 mag. The detection of OS3 is limited to a few data points. A possible scenario for this source is the close approach of around 3 pixels (∼ 0".04) to the DSO that could result in a flux and magnitude increase. Because of the crowded environment, the detection of OS3 is more challenging compared to the other discussed objects.

6.6 Possible scenarios for the nature of the DSO

Since the DSO stays on a Keplerian orbit even after passing Sgr A*, a gaseous nature of the DSO can be ruled out. The gravitational forces would have dissolved the DSO and destroyed it so it would not be possible to detect a compact object on the orbit. In fact, the discussed properties of the DSO can all be easily explained by assuming a stellar nature of the object. Different scenarios can now be addressed.

Wolf Rayet star

Wolf-Rayet (WR) stars are objects (see Hamann *et al.* 1991, Hamann *et al.* 1995) with weak or the lack of hydrogen lines. This is because the outer shells are blown away, and the remaining core is responsible for the emission lines. The mass is considered between ten and several hundreds of solar masses. There are subclasses which are emitting prominent

helium lines like it is observed for the DSO. The main problem with this classification is the abundance of hydrogen lines, the mass (according to Zajaček *et al.* 2017 and Zajaček *et al.* 2016, the DSO mass is supposed to be less than three solar masses), and the strong and broad outflow of Wolf-Rayet stars.

T-Tauri star

In contrast to Wolf-Rayet stars, T-Tauri objects fulfill the discussed requirements. These objects are classified with masses less than three solar masses. T-Tauri stars also consist of a protoplanetary disk that might explain the observed emission. To emphasis this point even more, Shahzamanian *et al.* (2016) discuss the observed and polarized light from the DSO. The high variability of the polarized light is pointing to a more complex structure of the DSO. One possible scenario would be a Young Stellar Object (YSO) that consists of a protoplanetary disk, a bipolar wind, and a forming bow-shock. A T-Tauri star could describe this scenario although the Brγ emission line and the magnitude/flux of the DSO are rather constant. T-Tauri stars are well-known for high variability in line intensity and flux because of accretion processes.

Class I object

Young stellar objects can be classified into different classes. Class II objects can be excluded since the core is revealed and the DSO has to be explained by a more complex scenario. Class III objects are categorized with an almost vanishing near-infrared excess. Since the DSO is prominent in the NIR, this classification can also be excluded. Deeply embedded objects with a positive infrared spectral index are classified as Class I objects. Considering the derived K-band magnitude of 18.5 mag and an L'-band magnitude of 14.4 mag, it is

$$Spectral\ index_{IR} = 18.5\ mag - 14.4\ mag = 4.1\ mag \ . \tag{6.1}$$

From this point of view, the DSO fulfills the requirements of Class I objects. These protostars are known for strong line emissions that dominate the continuum.

6.7   Conclusion

Summarizing the results answers the initial question of the nature of the DSO. Considering the numerous outcomes that indicate a gaseous nature of the DSO raises the question, what justifies this assumption. However, the analysis of the data leaves no doubt that a pure gas model for describing the near-infrared emission does not satisfy the observations. The most persuasive argument is certainly the detection of the object itself on a Keplerian orbit. A gaseous object would be destroyed by the gravitational force or the close encounter with the supermassive black hole. The precise detection of the DSO in the line maps after the periapse and the non dissolved structure underline the interpretation. This is followed by the detection of a compact source in the Lucy-Richardson images. These results show again the compact DSO on a Keplerian orbit around Sgr A*. By shifting these images to a fixed DSO position and comparing them to shifted and stacked K-band images, the robustness of the method is proven. It can be concluded, that a K-band counterpart indeed exists and that the K-L' colors are positive. With that, a YSO like scenario is a possible explanation for the DSO. Considering the colors and the confirmed polarized flux from the DSO, a Class I object fits the observations. Besides the detection in the line maps and the Lucy-Richardson images, the position-velocity diagrams show no stretching of the source. Also, no parallel detection of a red- and blue-shifted Brγ is observed. If the DSO would be a gas-cloud, parts of it would be stripped away while other parts are still in place. One part of the cloud be on the one side of the black hole (red-shifted), while the other part is on the other side (blue-shifted). When it comes to the presented pv diagram in 2008, it shows two objects beside the DSO that can be identified as OS1 and OS2. By using the same slit size as in Gillessen *et al.* (2012), these dusty infrared excess sources are included in the plot. With that, the interpretation of a tail, which follows the DSO, can be explained. On the other hand, no dissolving events because of the nature of the DSO takes place.

At the beginning of this chapter, the justification for the assumed gaseous nature of the object is questioned. A possible explanation is the chosen background that influences the detected signal. By placing background apertures randomly in the field of view, false signals can be created. In chapter 5, this is shown for 2014.3 where a false signal is created. Another explanation for the assumption that the data analysis shows signs of a non-stellar object is the approach of applying a smoothing kernel to it. The broadening of the Brγ line leads to an increase of the emission area. Following this, the wings of the Doppler-shifted lines are getting broader. Therefore, the range of the velocity values is getting wider, which leads to an increase of the gradient. It is important to note that a gradient per se is not an issue. Since the DSO is moving fast, the spatial shift, as well as the increase of the velocity during a year, is reflected in a natural gradient. But it can be concluded that smoothing the data is the wrong approach for analyzing the SINFONI data. Another adverse outcome of the data-smoothing besides the creation of a velocity gradient is the broadening of the emission area. This is an explanation for the claimed tail in Gillessen *et al.* (2012),

Pfuhl *et al.* (2015), and Plewa *et al.* (2017). Since the additional sources suffer from the same effects as the DSO, the Doppler-shifted emission lines of, for example OS1, is getting broader. This effect should be even stronger for this source since the strength of the emission lines of OS1 are weaker compared to the DSO by a factor of ~ 2. With this, noise is also included in the smoothing approach that leads to a significant increase of the emission area. Besides the smoothing procedure, it is obvious that the slit size for creating the position-velocity diagrams is also an important factor that can include signals that are spatially separated to the DSO. After the analysis of every data set between 2006 and 2015, it can be ruled out without a doubt that the DSO shows signs of a gaseous nature. The DSO is indeed a star that is moving on a Keplerian orbit around Sgr A*. The number of observed flares during the observational campaign is rather low ($\leq$ 2/night) and is consistent with the flare statistics of Sgr A* presented in Witzel *et al.* (2012).

As pointed out by Jalali *et al.* (2014), gas clumps with a mass of around $100\,M_{\odot}$ could have formed young stellar objects. The mass is high in enough to produce several stars because of the tidal stretching. The clumps are elongated and compressed because of the gravitational forces. Because of the compression, young stellar objects are formed. In this picture, supermassive black holes enhance the chance of star formation. During this work, four new sources besides the DSO are found. This number of dusty and compact sources indicate that star formation in the Galactic center is an ongoing process. This observational conclusion is also consistent with Jalali *et al.* (2014) where the authors, based on their model, propose that the formation of young stellar objects happens in groups or clumps. With that, the chance of finding non discovered sources is comparably high and probably increases with the new generation of telescopes like the Extremely Large Telescope (ELT). Also the new generation of interferometric instruments like GRAVITY (see Gravity Collaboration *et al.* 2017) with an imaging mode that is capable of resolving features that are less than 4 mas small. With this observing power, it is just a matter of time until new exciting and challenging objects are found.

OUTLOOK

Besides the DSO, the SINFONI data delivers other interesting scientific objects. The extensive analysis not only reveals the OS sources but also a new elongated object that can be found in the blue-shifted Brγ domain at 2.164 μm. This translates to a Brγ velocity of around 200km/s. The source which is named X8 can be found in every year between 2006 and 2015. The name of this discovered object is picked to be close to X7 (see Mužić *et al.* 2007) since it shows similarities between it. As mentioned, it is elongated and additionally points towards Sgr A* in every data set. That could point to a possible outflow coming from Sgr A*. Figure 7.1 shows the X8 source in several years. In the first column, the single line continuum emission is displayed. This is achieved by selecting the blue-shifted Brγ emission line. For 2005 and 2006, the contrast in the image is set to highlight X8. The same field of view with another contrast is shown for a better comparison of the position of X8 in 2012 and 2015. These images are then used with the Lucy-Richardson deconvolution algorithm. The results are shown in the second column. In contrast to the DSO, a low number of iterations is chosen for the deconvolution process. This is important because of the close distance to the surrounding stars. The algorithm is too sensitive to close sources since it can combine the flux information of nearby objects. The position of X8 in the sharpened images is consistent with the position in the single line continuum emission images. The third column shows high pass filtered images. They are the result of smooth-subtracting the images. For that, the original image is smoothed with a 3-pixel Gaussian. This smoothed image is then subtracted from the original image. Afterward, this result is smoothed again. This procedure eliminates low frequencies that are associated with noise. In contrast, high frequencies and therefore stars as well as extended sources are passed. The last column shows the blue-shifted Brγ line maps. These im-
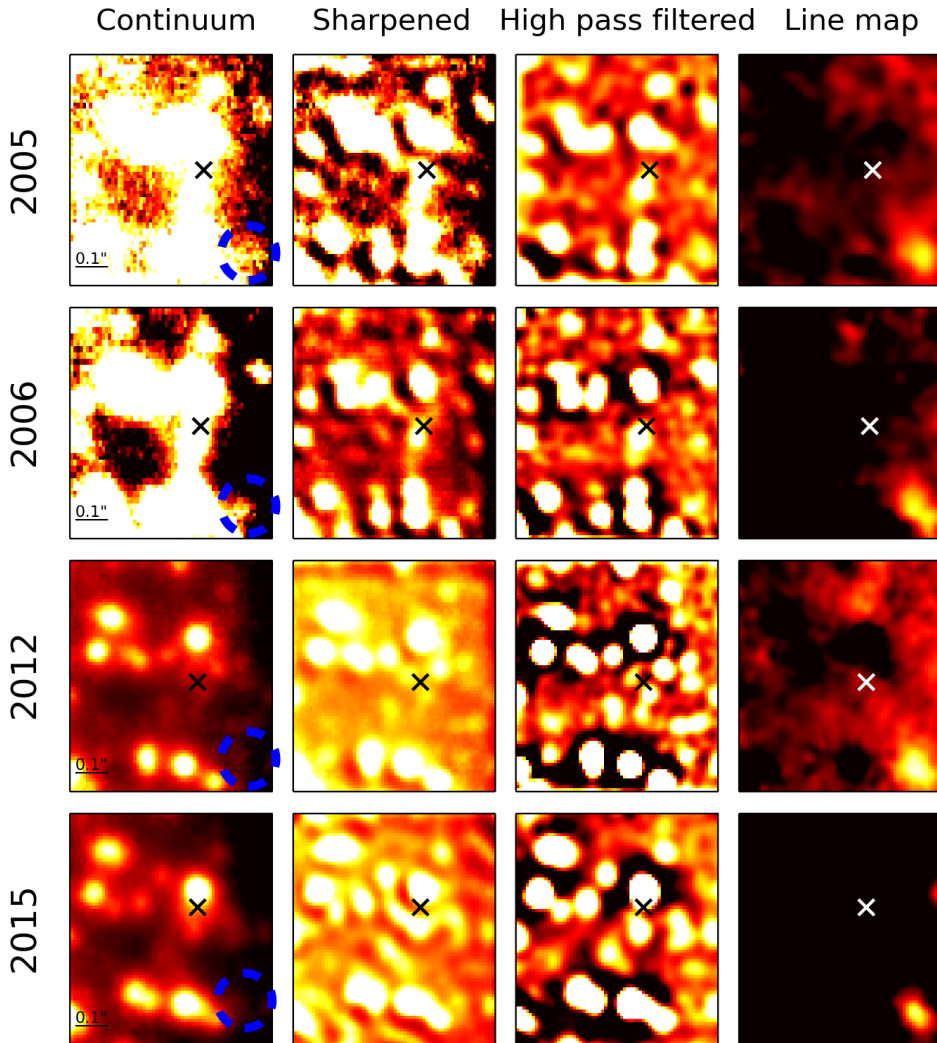
Figure 7.1: *The 16 single plots give an overview about the current status of the X8 analysis. The object is detected at the position of the blue dashed circle (left column). In every single plot, the emission source can be detected at the same position. The image is taken from Peißker et al. (in prep.).*

ages show an elongated source that is pointing towards Sgr A* (indicated by a white cross). The position is again consistent with the previous results and that raises the question if the single line continuum emission is connected to the Brγ line emission. Using the center of gravity of the 50% contour line in the line maps, the images are shifted to a fixed position. This shifting vector is then applied to the single line continuum images. The
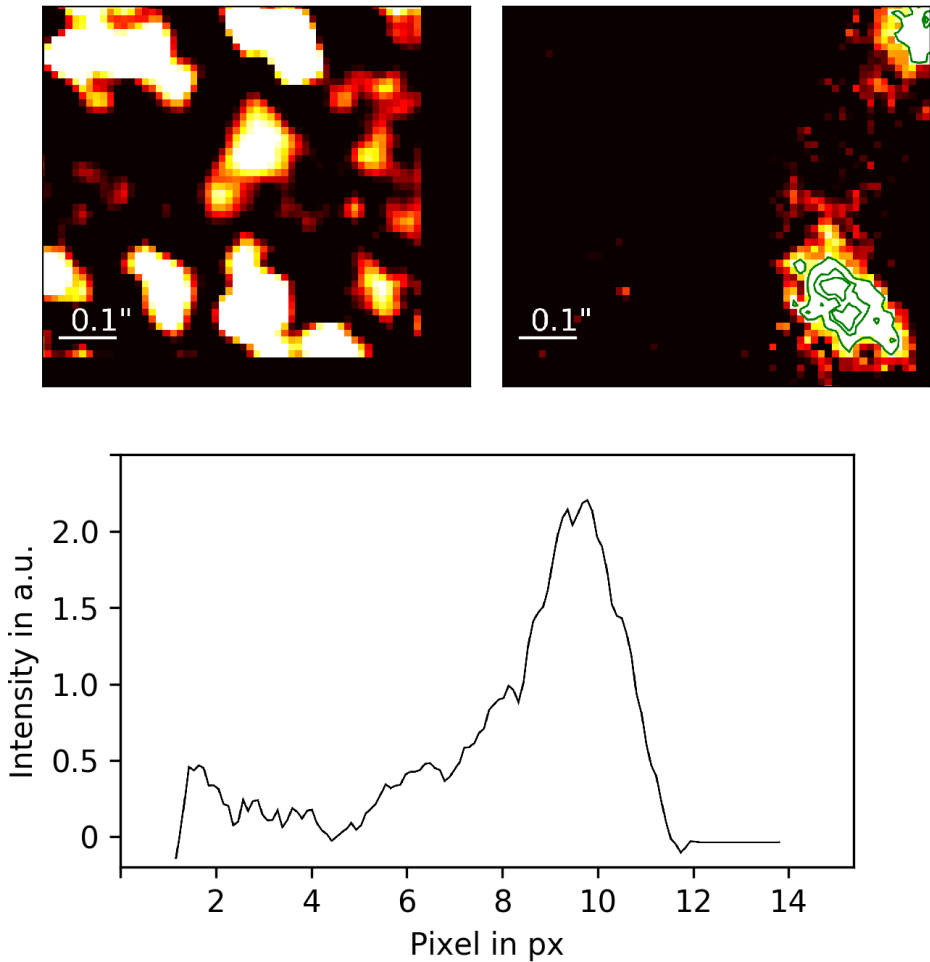
Figure 7.2: *These three plots show the new discovered source X8. The upper right image displays the stacked blue-shifted Brγ line map. Signs of bipolarity are clearly visible with two main emission peaks inside of the inner contour line. At the same position, a continuum source can be detected. The elongation of the continuum detection is comparable to the line map emission. Additionally, both sources are pointing towards Sgr A*. The lower plot is a cut through the aligned object that shows two distinct peaks at an intensity of over 2.0 (arbitrary units). The image is taken from Peißker et al. (in prep.).*

resulting images are shown in Figure 7.2. The right image shows the stacked line-maps of 2006, 2012, 2013, 2015, and 2016. It reveals signs of bipolarity since there are clearly two separate flux-peaks over the emission source. This could point to an outflow coming from a young stellar object. The left image shows a continuum emission at the position of the line map object. It is yet unclear if the objects of the continuum- and line-map images are connected to each other. If this would be a possibility, it could be warm dust that is heated up by a possible outflow from Sgr A*. This scenario is already discussed for X7 (Mužić *et al.* 2007) and could also be applied to X8. However, the bottom figure (Fig. 7.2) shows a 2D cut through the stacked line-map image along the alignment of X8. The graph shows indications of the double peak structure. Traces of this feature can also be seen in some of the line-maps in Figure 7.1 like in 2006. This is an indication that the detection is a function of data quality (weather conditions, noise, S/N ratio) and the number of observations that covers this particular area in the field of view.

The used SINFONI data

This section gives an overview about the used data sets. The majority of the data is down-

Date	Start time	End time	Amount of on source exposures			Exp. Time
			Total	Medium	High	
(YYYY:MM:DD)	(UT)	(UT)				(s)
2006.03.17	07:51:23	11:52:27	5	0	3	600
2006.03.20	07:33:06	07:42:27	1	1	0	600
2006.03.21	07:56:05	09:28:53	2	2	0	600
2006.04.22	08:47:59	08:57:24	1	0	0	600
2006.08.17	23:10:28	23:21:45	1	0	1	600
2006.08.18	23:19:54	03:46:01	5	0	5	600
2006.09.16	22:54:00	23:22:00	3	0	3	600
2007.03.26	06:46:26	06:57:32	1	1	0	600
2007.07.21	05:41:28	06:38:04	3	1	2	500
2007.09.03	23:42:50	01:11:12	4	1	3	600
2007.09.04	23:22:57	23:33:50	1	0	1	600
2008.04.06	05:25:26	08:50:00	16	0	15	600
2008.04.07	08:33:58	09:41:05	4	0	4	600
2009.05.21	06:10:02	08:50:36	7	0	7	600
2009.05.22	04:51:22	05:29:13	4	0	4	400
2009.05.23	09:41:41	09:57:17	2	0	2	400
2009.05.24	06:08:03	07:38:59	3	0	3	600

Table 7.1: *Note that medium exposures, who are slighty above the quality constrains (i.e. 0.1 − 0.2 px) are also included in order to increase the total on source integration time. The first column denotes the date of the night of the observation. The second and third column gives the exact Universal Time (UT). The on source exposure time is divided into a total-, medium-, and high-amount. The quality of some data-cubes is worse than medium. Hence, they are not listed separately. The last column denotes the exposure time in seconds.*

loaded from the ESO archive[1] except for some data sets in 2014 and 2015. These data-sets
are taken after the observations directly from the telescope-site. In total, over 520 single

Date	Start time	End time	Amount of on source exposures			Exp. Time
			Total	Medium	High	
(YYYY:MM:DD)	(UT)	(UT)				(s)
2010.05.10	06:03:00	09:35:20	3	0	3	600
2010.05.11	03:58:08	07:35:12	5	0	5	600
2010.05.12	09:41:41	09:57:17	13	0	13	600
2011.04.11	08:17:27	09:15:16	3	0	3	600
2011.04.27	05:10:41	09:23:09	10	1	9	600
2011.05.02	07:53:34	09:22:19	6	0	6	600
2011.05.14	08:47:28	09:25:07	2	0	2	600
2011.07.27	02:40:51	03:30:58	2	1	1	600
2012.03.18	08:55:49	09:17:01	2	0	2	600
2012.05.05	08:09:14	08:41:33	3	0	3	600
2012.05.20	08:13:44	08:23:44	1	0	1	600
2012.06.30	01:40:19	06:54:41	12	0	10	600
2012.07.01	03:11:53	05:13:45	4	0	4	600
2012.07.08	00:47:39	05:38:16	13	3	8	600
2012.09.08	00:01:36	00:23:33	2	1	1	600
2012.09.14	01:21:30	01:43:27	2	0	2	600
2013.04.05	08:55:49	09:43:38	2	0	2	600
2013.04.06	07:35:58	09:23:37	8	0	8	600
2013.04.07	07:27:49	09:40:35	3	0	3	600
2013.04.08	06:42:53	09:12:52	9	0	6	600
2013.04.09	07:08:17	10:01:46	8	1	7	600
2013.04.10	06:10:45	07:47:07	3	0	3	600
2013.08.28	00:40:17	03:11:43	10	1	6	600
2013.08.29	00:46:40	03:10:00	7	2	4	600
2013.08.30	02:31:22	03:24:46	4	2	0	600
2013.08.31	00:57:58	02:28:22	6	0	4	600
2013.09.23	23:40:31	01:49:33	6	0	0	600
2013.09.25	00:39:51	01:01:39	2	1	0	600
2013.09.26	23:55:53	00:39:13	3	1	1	600

Table 7.2: *The used SINFONI data between 2010 and 2013 (as shown in Table 7.1).*

exposures are reduced and analyzed. This translates into a total on source observation
time of over 5200 minutes/87 hours.

---

[1] www.archive.eso.org

Date	Start time	End time	Amount of on source exposures			Exp. Time
			Total	Medium	High	
(YYYY:MM:DD)	(UT)	(UT)				(s)
2014.02.27	08:40:42	09:41:36	4	1	3	600
2014.02.28	08:34:58	09:54:37	7	3	1	400
2014.03.01	08:00:14	10:17:59	11	2	4	400
2014.03.02	07:49:05	08:18:54	3	0	0	400
2014.03.11	08:03:55	10:03:28	11	2	9	400
2014.03.12	07:44:34	10:07:45	13	8	5	400
2014.03.26	06:43:04	09:58:12	9	3	5	400
2014.03.27	06:32:49	10:04:12	18	7	5	400
2014.04.02	06:31:38	09:53:52	18	6	1	400
2014.04.03	06:20:45	09:45:02	18	1	17	400
2014.04.04	05:58:18	09:47:58	21	1	20	400
2014.04.06	07:51:42	08:43:15	5	2	3	400
2014.04.08	07:04:37	09:39:47	5	1	0	600
2014.04.09	07:43:44	09:31:25	6	0	6	600
2014.04.10	05:46:47	09:45:03	14	4	10	600
2014.06.09	05:22:34	08:59:59	14	3	0	400
2014.06.10	05:20:38	06:35:24	5	4	0	400
2014.07.08	02:22:28	04:47:18	6	1	3	600
2014.07.13	00:33:27	01:41:15	4	0	2	600
2014.07.18	02:53:11	03:03:18	1	0	0	600
2014.08.18	02:26:09	02:47:10	2	0	1	600
2014.08.26	00:23:04	01:00:16	4	3	0	400
2014.08.31	23:30:25	01:20:25	6	3	1	600
2014.09.07	01:28:11	01:42:45	2	0	0	400
2015.04.12	05:52:37	10:14:30	18	2	0	400
2015.04.13	05:44:12	10:06:37	13	7	0	400
2015.04.14	07:07:28	08:29:18	5	1	0	400
2015.04.15	05:52:26	10:16:55	23	13	10	400
2015.08.01	23:22:12	04:41:09	23	7	8	400
2015.09.05	23:18:11	02:23:03	17	11	4	400

Table 7.3: *The used SINFONI data between 2014 and 2015 (as shown in Table 7.1).*

Lucy Richardson deconvolved images 2006-2015

For a better overview, the Lucy Richardson deconvolved low pass filtered images of the Galactic center are presented here separately. The central super massive black hole is at the position if the black cross. The images are centered on it and show the yearly movement of the surrounding stars. The DSO can be found in the white dashed circle. The brightness variations are not of physical nature. Different contrast settings for every year are the reason for the apparent magnitude variations. As shown in chapter 5, the magnitude and the flux is stable between 2006 and 2015.
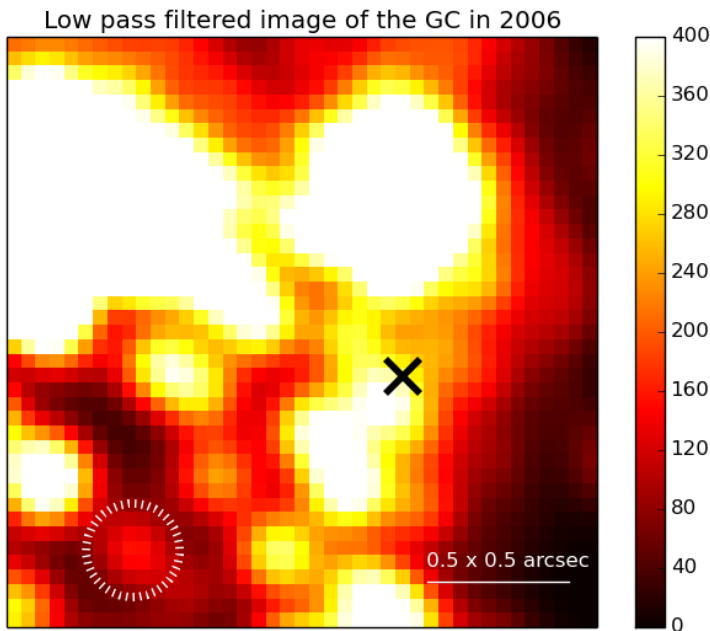
Figure 7.3: *The DSO (white dashed circle) on its way towards Sgr A* in 2006. The image is centered on Sgr A* (black cross). The contrast of the image is set to highlight the DSO.*
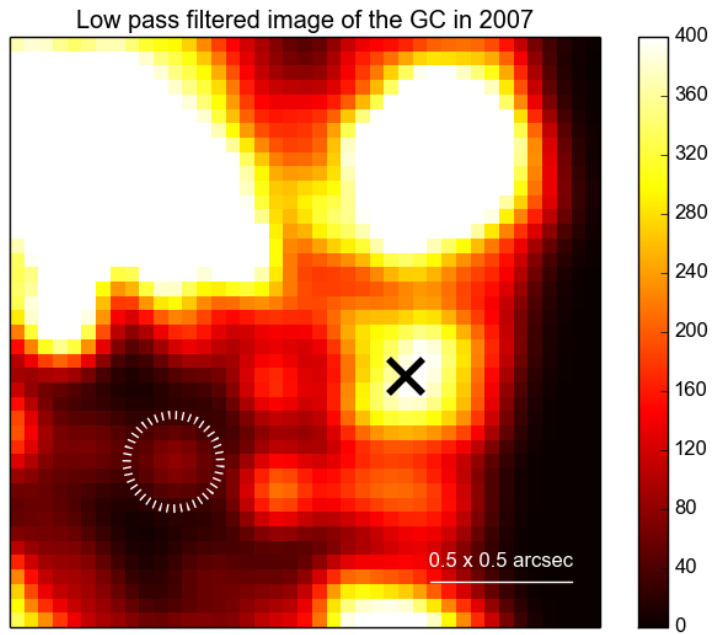
Figure 7.4: *Like in Figure 7.3 but for 2007.*
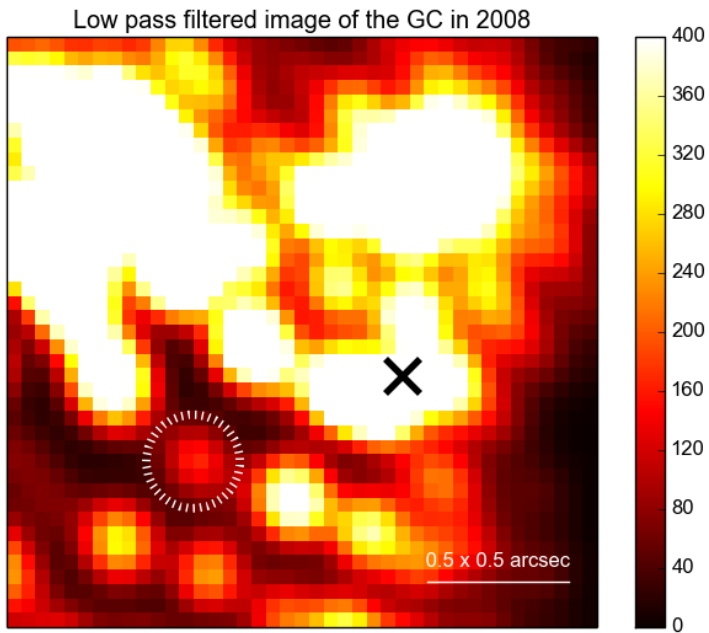
Figure 7.5: *Like in Figure 7.4 but for 2008.*
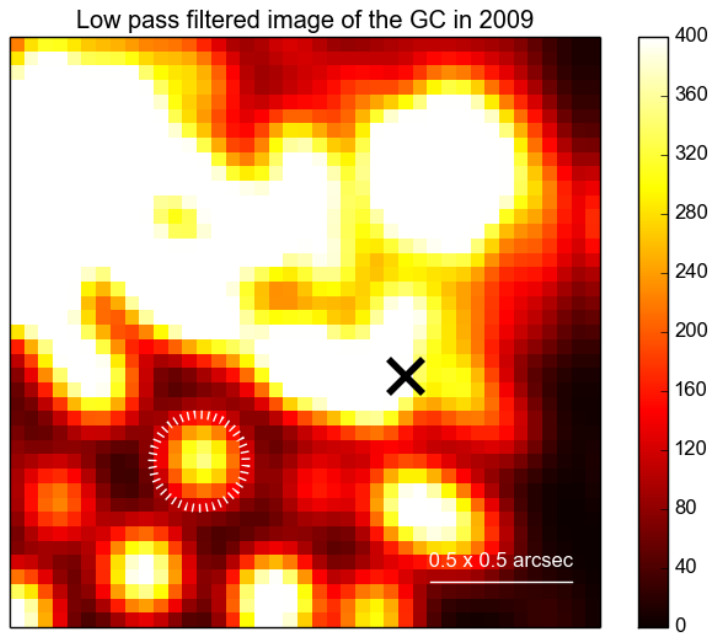
Figure 7.6: *Like in Figure 7.5 but for 2009.*
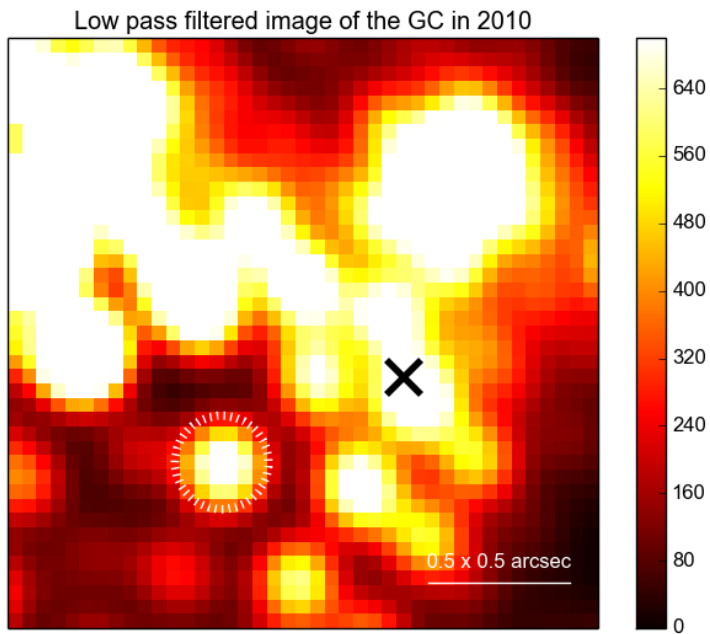
Figure 7.7: *Like in Figure 7.6 but for 2010.*
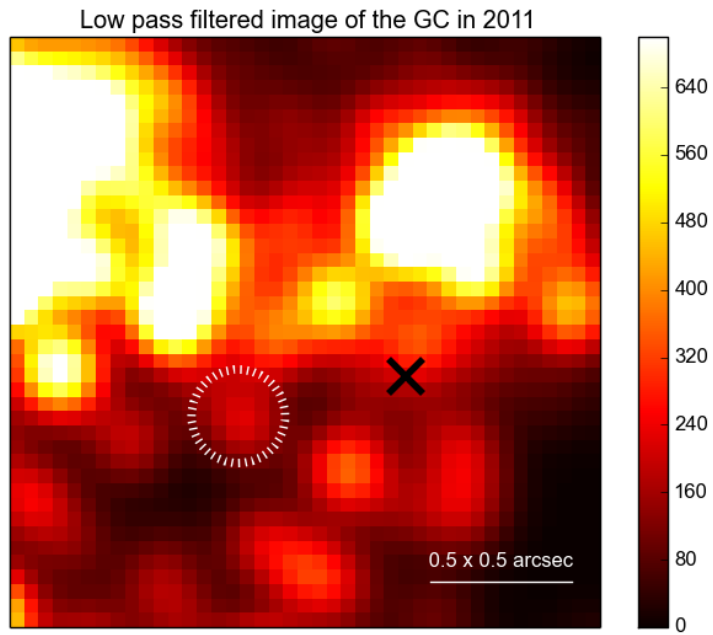
Figure 7.8: Like in Figure 7.7 but for 2011.
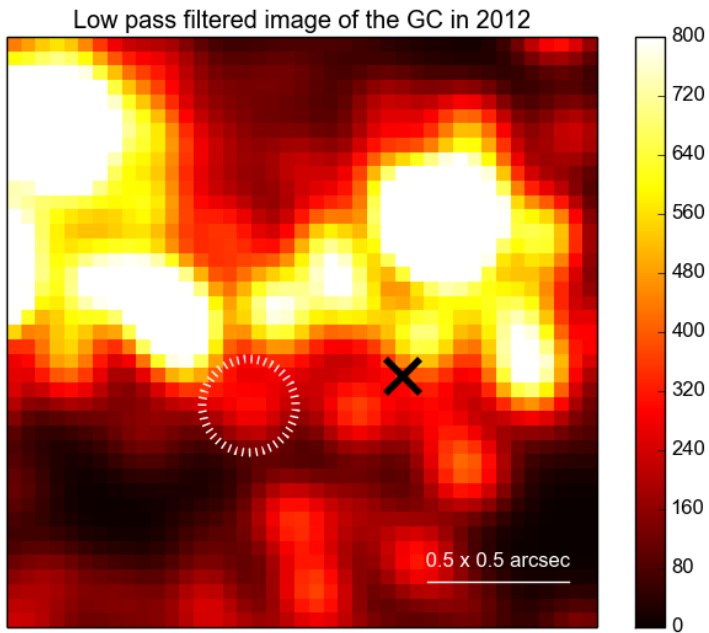
Figure 7.9: *Like in Figure 7.8 but for 2012.*
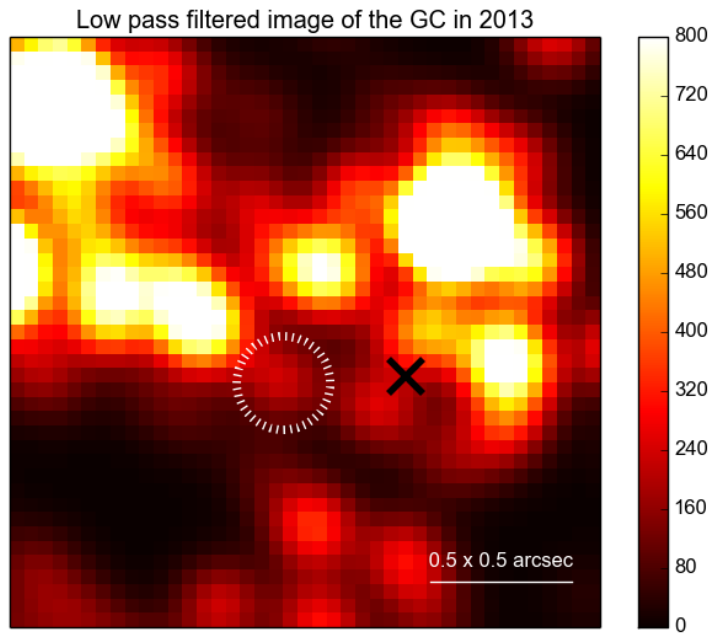
Figure 7.10: *Like in Figure 7.9 but for 2013.*
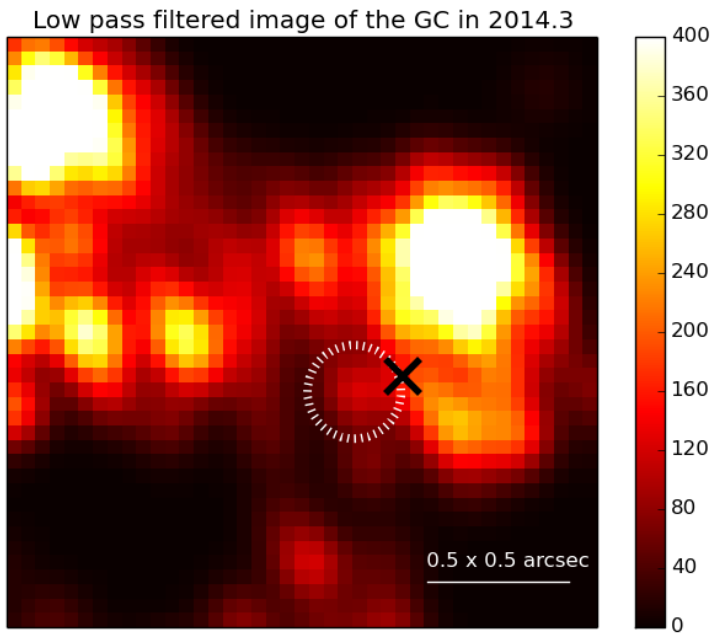
Figure 7.11: *Like in Figure 7.10 but for 2014 (before the peri-center passage).*
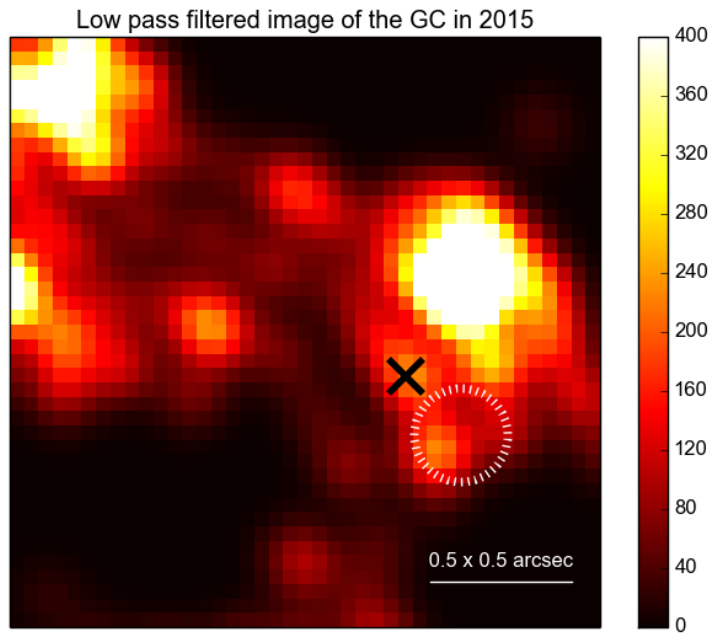
Figure 7.12: *Like in Figure 7.11 but for 2015 (after the peri-center passage).*

BIBLIOGRAPHY

Baker, J. G. and Menzel, D. H. (1938). Physical Processes in Gaseous Nebulae. III. The Balmer Decrement. *ApJ*, **88**, 52.

Balmer, J. J. (1897). A New Formula for the Wave-Lengths of Spectral Lines. *ApJ*, **5**, 199.

Barnard, E. (1927). *Catalogue of 349 dark objects in the sky*.

Boehle, A., Ghez, A. M., Schödel, R., Meyer, L., Yelda, S., Albers, S., Martinez, G. D., Becklin, E. E., Do, T., Lu, J. R., Matthews, K., Morris, M. R., Sitarski, B., and Witzel, G. (2016). An Improved Distance and Mass Estimate for Sgr A* from a Multistar Orbit Analysis. *ApJ*, **830**, 17.

Bohr, N. (1913). I. on the constitution of atoms and molecules. *The London, Edinburgh, and Dublin Philosophical Magazine and Journal of Science*, **26**(151), 1–25.

Bohr, N. and Rutherford, E. (1913). On the constitution of atoms and molecules: Part ii, systems containing only a single nucleus.

Burgess, A. (1958). The hydrogen recombination spectrum. *MNRAS*, **118**, 477.

Carter, C. S., Snodgrass, H. B., and Bryja, C. (1992). Telluric water vapor contamination of the Mount Wilson solar Doppler measurements. *Sol. Phys.*, **139**, 13–24.

Clénet, Y., Rouan, D., Gratadour, D., Marco, O., Léna, P., Ageorges, N., and Gendron, E. (2005). A dual emission mechanism in Sgr A*/L'. *A&A*, **439**, L9–L13.

Davies, R. I. (2007). A method to remove residual OH emission from near-infrared spectra. *MNRAS*, **375**, 1099–1105.

Demtröder, W. (2004). *Experimentalphysik 2*. SpringerLink : Bücher. Springer, Berlin, Heidelberg, 6., überarb. u. akt. aufl. 2013 edition.

Eckart, A. and Duhoux, P. R. M. (1991). Infrared speckle reduction software at the MPE. In R. Elston, editor, *Astronomical Society of the Pacific Conference Series*, volume 14 of *Astronomical Society of the Pacific Conference Series*, pages 336–338.

Eckart, A. and Genzel, R. (1996). Observations of the Galactic Center with SHARP: First Stellar Proper Motions. **102**, 196.

Eckart, A., Mužić, K., Yazici, S., Sabha, N., Shahzamanian, B., Witzel, G., Moser, L., Garcia-Marin, M., Valencia-S., M., Jalali, B., Bremer, M., Straubmeier, C., Rauch, C., Buchholz, R., Kunneriath, D., and Moultaka, J. (2013). Near-infrared proper motions and spectroscopy of infrared excess sources at the galactic center. *aap*, **551**, A18.

Einstein, A. (1905). Ist die traegheit eines koerpers von seinem energieinhalt abhaengig? *Annalen der Physik*, **323**(13), 639–641.

Eisenhauer (2003). SINFONI - Integral field spectroscopy at 50 milli-arcsecond resolution with the ESO VLT. volume 4841 of *Proc. SPIE*, pages 1548–1561.

Fritz, T. K., Gillessen, S., Dodds-Eden, K., Lutz, D., Genzel, R., Raab, W., Ott, T., Pfuhl, O., Eisenhauer, F., and Yusef-Zadeh, F. (2011). Line Derived Infrared Extinction toward the Galactic Center. *ApJ*, **737**, 73.

Ghez, A. M., Hornstein, S. D., Lu, J. R., Bouchez, A., Le Mignant, D., van Dam, M. A., Wizinowich, P., Matthews, K., Morris, M., Becklin, E. E., Campbell, R. D., Chin, J. C. Y., Hartman, S. K., Johansson, E. M., Lafon, R. E., Stomski, P. J., and Summers, D. M. (2005). The First Laser Guide Star Adaptive Optics Observations of the Galactic Center: Sgr A*'s Infrared Color and the Extended Red Emission in its Vicinity. *ApJ*, **635**, 1087–1094.

Gillessen, S. (2014). Observations of the gas cloud G2 in the Galactic Center. **40**.

Gillessen, S., Eisenhauer, F., Trippe, S., Alexander, T., Genzel, R., Martins, F., and Ott, T. (2009). Monitoring Stellar Orbits Around the Massive Black Hole in the Galactic Center. *ApJ*, **692**, 1075–1109.

Gillessen, S., Genzel, R., Fritz, T. K., Quataert, E., Alig, C., Burkert, A., Cuadra, J., Eisenhauer, F., Pfuhl, O., Dodds-Eden, K., Gammie, C. F., and Ott, T. (2012). A gas cloud on its way towards the supermassive black hole at the Galactic Centre. *Nature*, **481**, 51–54.

Gillessen, S., Genzel, R., Fritz, T. K., Eisenhauer, F., Pfuhl, O., Ott, T., Schartmann, M., Ballone, A., and Burkert, A. (2013). Pericenter Passage of the Gas Cloud G2 in the Galactic Center. *ApJ*, **774**, 44.

Gravity Collaboration, Abuter, R., Accardo, M., Amorim, A., Anugu, N., Ávila, G., Azouaoui, N., Benisty, M., Berger, J. P., Blind, N., Bonnet, H., Bourget, P., Brandner, W., Brast, R., Buron, A., Burtscher, L., Cassaing, F., Chapron, F., Choquet, É., Clénet, Y., Collin, C., Coudé Du Foresto, V., de Wit, W., de Zeeuw, P. T., Deen, C., Delplancke-Ströbele, F., Dembet, R., Derie, F., Dexter, J., Duvert, G., Ebert, M., Eckart, A., Eisenhauer, F., Esselborn, M., Fédou, P., Finger, G., Garcia, P., Garcia Dabo, C. E., Garcia Lopez, R., Gendron, E., Genzel, R., Gillessen, S., Gonte, F., Gordo, P., Grould, M., Grözinger, U., Guieu, S., Haguenauer, P., Hans, O., Haubois, X., Haug, M., Haussmann, F., Henning, T., Hippler,

S., Horrobin, M., Huber, A., Hubert, Z., Hubin, N., Hummel, C. A., Jakob, G., Janssen, A., Jochum, L., Jocou, L., Kaufer, A., Kellner, S., Kendrew, S., Kern, L., Kervella, P., Kiekebusch, M., Klein, R., Kok, Y., Kolb, J., Kulas, M., Lacour, S., Lapeyrère, V., Lazareff, B., Le Bouquin, J.-B., Lèna, P., Lenzen, R., Lévêque, S., Lippa, M., Magnard, Y., Mehrgan, L., Mellein, M., Mérand, A., Moreno-Ventas, J., Moulin, T., Müller, E., Müller, F., Neumann, U., Oberti, S., Ott, T., Pallanca, L., Panduro, J., Pasquini, L., Paumard, T., Percheron, I., Perraut, K., Perrin, G., Pflüger, A., Pfuhl, O., Phan Duc, T., Plewa, P. M., Popovic, D., Rabien, S., Ramírez, A., Ramos, J., Rau, C., Riquelme, M., Rohloff, R.-R., Rousset, G., Sanchez-Bermudez, J., Scheithauer, S., Schöller, M., Schuhler, N., Spyromilio, J., Straubmeier, C., Sturm, E., Suarez, M., Tristram, K. R. W., Ventura, N., Vincent, F., Waisberg, I., Wank, I., Weber, J., Wieprecht, E., Wiest, M., Wiezorrek, E., Wittkowski, M., Woillez, J., Wolff, B., Yazici, S., Ziegler, D., and Zins, G. (2017). First light for GRAVITY: Phase referencing optical interferometry for the Very Large Telescope Interferometer. *A&A*, **602**, A94.

Grotrian, W., Born, M., and Franck, J. (1928). *Graphische Darstellung der Spektren von Atomen und Ionen mit ein, zwei und drei Valenzelektronen: Zweiter Teil.* Struktur der Materie in Einzeldarstellungen. Springer Berlin Heidelberg.

Grould, M., Vincent, F. H., Paumard, T., and Perrin, G. (2017). General relativistic effects on the orbit of the S2 star with GRAVITY. *A&A*, **608**, A60.

Hairer, E., Nørsett, S., and Wanner, G. (2008). *Solving Ordinary Differential Equations I: Nonstiff Problems.* Springer Series in Computational Mathematics. Springer Berlin Heidelberg.

Haken, H. and Wolf, H. (2003). *Molekülphysik und Quantenchemie: Einführung in Die Experimentellen und Theoretischen Grundlagen.* Physics and astronomy online library. Springer.

Hamann, W.-R., Duennebeil, G., Koesterke, L., Wessolowski, U., and Schmutz, W. (1991). Spectral analyses of Wolf-Rayet stars - Hydrogen abundances in WN subtypes. *A&A*, **249**, 443–454.

Hamann, W.-R., Koesterke, L., and Wessolowski, U. (1995). Spectral atlas of the Galactic Wolf-Rayet stars (WN sequence). *A&AS*, **113**, 459.

Jalali, B., Pelupessy, F. I., Eckart, A., Portegies Zwart, S., Sabha, N., Borkar, A., Moultaka, J., Mužić, K., and Moser, L. (2014). Star formation in the vicinity of nuclear black holes: young stellar objects close to Sgr A*. *MNRAS*, **444**, 1205–1220.

Karssen, G. D., Bursa, M., Eckart, A., Valencia-S, M., Dovciak, M., Karas, V., and Horak, J. (2017). Bright X-ray flares from Sgr A. *MNRAS*, **472**, 4422–4433.

Kurosawa, R. and Romanova, M. M. (2013). Spectral variability of classical T Tauri stars accreting in an unstable regime. *MNRAS*, **431**, 2673–2689.

Kutta, W. (1901). Beitrag zur naeherungsweisen integration totaler differentialgleichungen. *Z. Math. Phys.*, **46**, 435–453.

Liu, L., Li, Z., Arcone, S., Fu, L., and Huang, Q. (2013). Radar wave scattering loss in a densely packed discrete random medium: Numerical modeling of a box-of-boulders experiment in the mie regime. *Journal of Applied Geophysics*, **99**, 68 – 75.

Lo Curto, G., Pasquini, L., Manescau, A., Holzwarth, R., Steinmetz, T., Wilken, T., Probst, R., Udem, T., Hänsch, T. W., González Hernández, J., Esposito, M., Rebolo, R., Canto Martins, B., and Renan de Medeiros, J. (2012). Astronomical Spectrograph Calibration at the Exo-Earth Detection Limit. *The Messenger*, **149**, 2–6.

Martinez, P., Kolb, J., Sarazin, M., and Tokovinin, A. (2010). On the Difference between Seeing and Image Quality: When the Turbulence Outer Scale Enters the Game. *The Messenger*, **141**, 5–8.

Meyer, F. and Meyer-Hofmeister, E. (2012). A nova origin of the gas cloud at the galactic center? *aap*, **546**, L2.

Meyer, L., Ghez, A. M., Witzel, G., Do, T., Phifer, K., Sitarski, B. N., Morris, M. R., Boehle, A., Yelda, S., Lu, J. R., and Becklin, E. (2014). The Keplerian orbit of G2. **303**, 264–268.

Mie, G. (1908). Beitraege zur optik trueber medien, speziell kolloidaler metalloesungen. *Annalen der Physik*, **330**(3), 377–445.

Modigliani, A., Hummel, W., Abuter, R., Amico, P., Ballester, P., Davies, R., Dumas, C., Horrobin, M., Neeser, M., Kissler-Patig, M., Peron, M., Rehunanen, J., Schreiber, J., and Szeifert, T. (2007). The sinfoni pipeline. *ArXiv Astrophysics e-prints*.

Mužić, K., Eckart, A., Schödel, R., Meyer, L., and Zensus, A. (2007). First proper motions of thin dust filaments at the Galactic center. *A&A*, **469**, 993–1002.

Mužić, K., Eckart, A., Schödel, R., Buchholz, R., Zamaninasab, M., and Witzel, G. (2010). Comet-shaped sources at the Galactic center. Evidence of a wind from the central 0.2 pc. *A&A*, **521**, A13.

Parsa, M., Eckart, A., Shahzamanian, B., Karas, V., Zajaček, M., Zensus, J. A., and Straubmeier, C. (2017). Investigating the Relativistic Motion of the Stars Near the Supermassive Black Hole in the Galactic Center. *ApJ*, **845**, 22.

Paumard, T., Genzel, R., Martins, F., Nayakshin, S., Beloborodov, A. M., Levin, Y., Trippe, S., Eisenhauer, F., Ott, T., Gillessen, S., Abuter, R., Cuadra, J., Alexander, T., and Sternberg, A. (2006). The two young star disks in the central parsec of the galaxy: Properties, dynamics, and formation. *The Astrophysical Journal*, **643**(2), 1011.

Peter L. Wizinowich, D. Scott Acton, O. L. J. G. W. L. P. J. S. (2000). Performance of the w.m. keck observatory natural guide star adaptive optic facility: the first year at the telescope.

Peterson, B. (1997). *An Introduction to Active Galactic Nuclei.* Cambridge University Press.

Pfuhl, O., Gillessen, S., Eisenhauer, F., Genzel, R., Plewa, P. M., Ott, T., Ballone, A., Schartmann, M., Burkert, A., Fritz, T. K., Sari, R., Steinberg, E., and Madigan, A.-M. (2015). The Galactic Center Cloud G2 and its Gas Streamer. *ApJ*, **798**, 111.

Phinney, E. S. (1989). Manifestations of a Massive Black Hole in the Galactic Center. In M. Morris, editor, *The Center of the Galaxy*, volume 136 of *IAU Symposium*, page 543.

Plewa, P. M., Gillessen, S., Pfuhl, O., Eisenhauer, F., Genzel, R., Burkert, A., Dexter, J., Habibi, M., George, E., Ott, T., Waisberg, I., and von Fellenberg, S. (2017). The Postpericenter Evolution of the Galactic Center Source G2. *ApJ*, **840**, 50.

Pych, W. (2004). A Fast Algorithm for Cosmic-Ray Removal from Single Images. *PASP*, **116**, 148–153.

Riekher, R. (1990). *Fernrohre und ihre Meister*. Verlag Technik.

Runge, C. (1895). Ueber die numerische aufloesung von differentialgleichungen. *Math. Ann.*, pages 167–178.

Sabha, N., Eckart, A., Merritt, D., Zamaninasab, M., Witzel, G., García-Marín, M., Jalali, B., Valencia-S., M., Yazici, S., Buchholz, R., Shahzamanian, B., Rauch, C., Horrobin, M., and Straubmeier, C. (2012). The S-star cluster at the center of the Milky Way. On the nature of diffuse NIR emission in the inner tenth of a parsec. *A&A*, **545**, A70.

Shahzamanian, B., Eckart, A., Valencia-S., M., Witzel, G., Zamaninasab, M., Sabha, N., García-Marín, M., Karas, V., Karssen, G. D., Borkar, A., Dovčiak, M., Kunnerieth, D., Bursa, M., Buchholz, R., Moultaka, J., and Straubmeier, C. (2015). Polarized light from Sagittarius A* in the near-infrared K_s-band. *A&A*, **576**, A20.

Shahzamanian, B., Eckart, A., Zajaček, M., Valencia-S., M., Sabha, N., Moser, L., Parsa, M., Peissker, F., and Straubmeier, C. (2016). Polarized near-infrared light of the Dusty S-cluster Object (DSO/G2) at the Galactic center. *A&A*, **593**, A131.

Smajić, S., Moser, L., Eckart, A., Valencia-S., M., Combes, F., Horrobin, M., García-Burillo, S., García-Marín, M., Fischer, S., and Zuther, J. (2014). ALMA-backed NIR high resolution integral field spectroscopy of the NUGA galaxy NGC 1433. *A&A*, **567**, A119.

Valencia-S., M., Eckart, A., Zajaček, M., Peissker, F., Parsa, M., Grosso, N., Mossoux, E., Porquet, D., Jalali, B., Karas, V., Yazici, S., Shahzamanian, B., Sabha, N., Saalfeld, R., Smajic, S., Grellmann, R., Moser, L., Horrobin, M., Borkar, A., García-Marín, M., Dovčiak, M., Kunnerieth, D., Karssen, G. D., Bursa, M., Straubmeier, C., and Bushouse, H. (2015). Monitoring the Dusty S-cluster Object (DSO/G2) on its Orbit toward the Galactic Center Black Hole. *ApJ*, **800**, 125.

Voshchinnikov, N. V., Henning, T., and Il'in, V. B. (2017). Mid-infrared Extinction and Fresh Silicate Dust towards the Galactic Center. *ApJ*, **Volume 837**, Doi 10.3847/1538–4357/aa5d53, 25 pages.

Wilson, R. (2013). *Reflecting Telescope Optics I: Basic Design Theory and its Historical Development*. Astronomy and Astrophysics Library. Springer Berlin Heidelberg.

Witzel, G., Eckart, A., Bremer, M., Zamaninasab, M., Shahzamanian, B., Valencia-S., M., Schödel, R., Karas, V., Lenzen, R., Marchili, N., Sabha, N., Garcia-Marin, M., Buchholz, R. M., Kunneriath, D., and Straubmeier, C. (2012). Source-intrinsic Near-infrared Properties of Sgr A*: Total Intensity Measurements. *ApJS*, **203**, 18.

Witzel, G., Ghez, A. M., Morris, M. R., Sitarski, B. N., Boehle, A., Naoz, S., Campbell, R., Becklin, E. E., Canalizo, G., Chappell, S., Do, T., Lu, J. R., Matthews, K., Meyer, L., Stockton, A., Wizinowich, P., and Yelda, S. (2014). Detection of Galactic Center Source G2 at 3.8 μm during Periapse Passage. *ApJ*, **796**, L8.

Witzel, G., Sitarski, B. N., Ghez, A. M., Morris, M. R., Hees, A., Do, T., Lu, J. R., Naoz, S., Boehle, A., Martinez, G., Chappell, S., Schödel, R., Meyer, L., Yelda, S., Becklin, E. E., and Matthews, K. (2017). The Post-periapsis Evolution of Galactic Center Source G1: The Second Case of a Resolved Tidal Interaction with a Supermassive Black Hole. *ApJ*, **847**, 80.

Zajaček, M., Eckart, A., Karas, V., Kunneriath, D., Shahzamanian, B., Sabha, N., Mužić, K., and Valencia-S., M. (2016). Effect of an isotropic outflow from the Galactic Centre on the bow-shock evolution along the orbit. *MNRAS*, **455**, 1257–1274.

Zajaček, M., Britzen, S., Eckart, A., Shahzamanian, B., Busch, G., Karas, V., Parsa, M., Peissker, F., Dovčiak, M., Subroweit, M., Dinnbier, F., and Zensus, J. A. (2017). Nature of the Galactic centre NIR-excess sources. I. What can we learn from the continuum observations of the DSO/G2 source? *A&A*, **602**, A121.

LIST OF FIGURES

LIST OF TABLES

DANKSAGUNG

Natürlich möchte ich an dieser Stelle allen voran meinen Eltern danken. Trotz meiner Startschwierigkeiten in der Bildungs- und Arbeitswelt hatte ich nie das Gefühl, eine Erwartungshaltung erfüllen zu müssen. Druck war sowieso nur von den Bildungsinstitutionen zu spüren. Ich möchte natürlich auch meiner gesamten Familie für den Rückhalt und die endlose Unterstützung über die ganzen Jahre danken. Diese Arbeit hätte ich niemals schreiben können ohne Spontandarlehen, zahlose CARE-Pakete, erholsamen Ablenkungen sowie Rückhalt auch in schwierigen Situationen.

Außerdem bin ich unendlich dankbar, so tolle Freunde in meinem Leben zu haben, die auch mal mit hilfreicher Kritik während der letzten Jahre mir zur Seite standen und weiterhin auch stehen.

Meinem Sohn Jakob danke ich einfach nur dafür, dass es ihn gibt.

Den Mittelteil der Danksagung widme ich den besten Korrekturlesern und Korrekturleserinnen, die ich mir wünschen konnte. Das wären (in alphabestischer Reihenfolge) Fabio, Lukas, Marzieh, Matthias, Nadeen und Saskia (die beste Schwester aller Zeiten). Ich bin unendlich dankbar für eure Mithilfe. Ihr habt aus dem hässlichen Entlein einen (meiner Meinung nach) schönen Schwan gemacht.

Auch danke ich Andreas Eckart für die Möglichkeit, in seiner Arbeitsgruppe zu promovieren. Besser hätte ich es nicht treffen können, besser hätte es Andreas Eckart nicht gestalten können. Auch danke ich meinem Zweitprüfer Anton Zensus für die Zusage und Korrektur. Bei Johannes Berg und Steffen Rost möchte ich mich für den Prüfungsvorsitz sowie das Protokollieren der Verteidigung bedanken.

Hier auch noch einmal ein großes Dankeschön an die ae-group für die atemberaubend schöne Arbeitsatmosphäre. Ebenfalls sei meinem Büro für die schöne Zeit gedankt. Ganz besonders Fabio.

ERKLÄRUNG

Ich versichere, daß ich die von mir vorgelegte Dissertation selbständig angefertigt, die benutzten Quellen und Hilfsmittel vollständig angegeben und die Stellen der Arbeit – einschließlich Tabellen, Karten und Abbildungen –, die anderen Werken im Wortlaut oder dem Sinn nach entnommen sind, in jedem Einzelfall als Entlehnung kenntlich gemacht habe; daß diese Dissertation noch keiner anderen Fakultät oder Universität zur Prüfung vorgelegen hat; daß sie – abgesehen von unten angegebenen Teilpublikationen – noch nicht veröffentlicht worden ist sowie, daß ich eine solche Veröffentlichung vor Abschluß des Promotionsverfahrens nicht vornehmen werde. Die Bestimmungen dieser Promotionsordnung sind mir bekannt. Die von mir vorgelegte Dissertation ist von Prof. Dr. Andreas Eckart betreut worden.

Köln, 29.03.2018

Lebenslauf

Persönliche Angaben

Name:	Florian Peißker
Anschrift:	I. Physikalisches Institut, Universität zu Köln
	Zülpicher Str. 77, 50937 Köln
Email:	peissker@ph1.uni-koeln.de
Geburtsdatum und -ort:	28.07.1982 in Pößneck, Deutschland
Staatsangehörigkeit:	Deutsch
Familienstand:	Ledig, ein Kind

Ausbildung und Berufserfahrung

Seit Okt. 2014	Promotionstudent an der Universität zu Köln,
	wiss. Betreuer: Prof. Dr. Andreas Eckart
2011 - 2014	Master of Science (Physik) an der Universität zu Köln
2005 - 2010	Bachelor of Science (Physik) an der Philipps-Universität Marburg
2004 - 2005	Berufsschule (Technik) Montabaur
2001 - 2004	Berufsausbildung zum Energieelektroniker für Anlagentechnik
	bei Dasbach Industriesteuerungen, Ransbach Baumbach
1999 - 2001	Berufsfachschule/Fachrichtung Elektrotechnik
	an der David-Roentgen-Schule, Neuwied
1997 - 1999	Hauptschule Nauort